Leibniz Universität Hannover
Physikalisch-Technische Bundesanstalt

Controlling mixed-species ion Coulomb crystals for optimal cooling and mitigating micromotion induced non-thermal heating

Von der Fakultät für Mathematik und Physik der
Gottfried Wilhelm Leibniz Universität Hannover
zur Erlangung des Grades

Master of Science Physik

vorgelegte Masterarbeit von

Leon Schomburg
geboren am 12.07.1995 in Hannover

Erstprüferin: **Prof. Dr. Tanja Mehlstäubler**
Zweitprüfer: **Prof. Dr. Piet O. Schmidt**

08. Oktober 2021

Abstract

Atomic clocks are humankind's most precise measuring instruments and are used in various applications as well as fundamental research. This thesis presents theoretical calculations and experimental measurements to enable multi-ion clock operation with mixed-species Coulomb crystals with low systematic uncertainties and an improved signal-to-noise ratio with respect to current single-ion clocks. The chosen platform for these experiments is a segmented linear Paul trap which stores ytterbium ions for sympathetic cooling and indium ions for clock interrogation.
This thesis provides a model that calculates motional mode cooling times for linear Coulomb crystals. The cooling times are strongly influenced by the crystal composition and configuration as well as by the confinement in the trap, and can differ by several orders of magnitude. This work identifies general trends and provides guidelines for choosing suitable conditions.
Furthermore, this work presents a deterministic loading scheme for mixed species crystals with In^+ and Yb^+ ions. This requires an algorithm that detects non-fluorescent indium ions, using a camera detecting ytterbium florescence. As background gas collisions can randomize the crystal configuration, re-ordering is investigated to reproducibly generate efficiently cooled configurations. Two methods are tested and prove to be reliable.
As a last topic, experiments are performed that investigate cooling of a single Yb^+ ion that undergoes excess micromotion (EMM). The results show that cooling of higher dimensional crystals where EMM is unavoidable could be applicable. This could lead to the development of new cooling strategies for operating multi-ion clocks.

Contents

1 Introduction

Atomic clocks are the most precise measuring instruments, reaching fractional frequency uncertainties below 10^{-18} [1]. Due to the relativistic red shift, such clocks can resolve height differences in the earths gravitational potential on a cm-level, which makes them interesting for geodesy [2]. Frequency measurements at this level can also serve as tests of fundamental physics [3].
Different experimental implementations of optical clocks are currently being pursued. One successful platform are trapped ions, which support low systematic uncertainties due to a trapping mechanism which does not interact with the electronic energy levels (to first order) and allows for strong localization. However, current state-of-the art ion clocks are operated with single clock ions and therefore have low signal-to-noise ratios. This requires long averaging times of up to 10 days to resolve transition frequencies at the 10^{-18} level, which makes them less practical in their applications. Another implementation is the neutral atom lattice clock. Due to particle numbers of 10^3 to 10^4 atoms, such clocks outperform current ion clocks in their statistical uncertainties.
The advantages of both approaches can be combined by loading multiple ions into an ion trap. Probing the ions simultaneously increases the signal and therefore decreases the clock's statistical uncertainty. In our approach the ions are stored in Coulomb crystals. Such crystals result from the balance between the trapping potential and the ions' Coulomb repulsion.
Coulomb crystals can contain ions of different species, which fulfil different purposes. This thesis contributes to an approach which uses $^{115}In^+$ ions as clock ions as they provide a suitably narrow transition with a low sensitivity to electric field gradients and other external influences [4]. $^{172}Yb^+$ ions, which are also loaded into the trap, are cooled with a cooling laser. The cooling effect is transferred to the whole ion crystal due to the Coulomb interaction, in a process known as sympathetic cooling that was first applied in [5]. Cooling is an essential part of all precision spectroscopy experiments as it reduces motion related frequency shifts. Optical clock measurements include cooling phases in each experimental cycle. For Coulomb crystals, the cooling process enables the ions to crystallize in the first place.
Our multi-ion clock approach is based on linear one-dimensional Coulomb crystals in a linear Paul trap [6], as they allow easy detection and control of the crystal. If laser cooling is only applied to a fraction of the ions, the composition and configuration of different ion species in the crystalline structure play an important role for the sympathetic cooling efficiency. This work deals with solutions for the requirements previously described. After chapter 2 and chapter 3 give a theoretical background of ion traps and an overview over the experimental setup, chapter 4 provides a model to calculate cooling times of linear ion Coulomb crystals and evaluates their dependence on the configuration and the composition of the crystal and other trap parameters. This allows to determine advantageous compositions with respect to sympathetic cooling. The chapter shows that the cooling times vary over several orders of magnitude depending on the chosen crystal configuration

and trap parameters. As the cooling time impacts the clock duty cycle, it is desired to be as short as possible. The chapter also shows that cooling might be more efficient with two- or three-dimensional crystals under certain conditions.
The operation of an ion trap with specific configurations and compositions of Coulomb crystals requires a deterministic loading routine. Chapter 5 presents a technique to experimentally load ion crystals with deterministic numbers of In^+ and Yb^+ ions with up to 30 ions in total. The chapter also investigates reproducible reordering sequences, which can be applied on the basis of the cooling time calculations and become necessary when background collisions melt and mix the crystal.
Recent proposals for ion clocks suggest to store larger, two- or three-dimensional crystals in ion traps to further reduce the statistical uncertainties [7, 8]. Higher dimensional crystals can experience difficulties in the cooling process caused by excess micromotion (EMM). This occurs in linear Paul traps when ions are trapped outside the one-dimensional rf nodal line and is therefore unavoidable for the proposed crystals. Chapter 6 investigates a cooling technique for a single Yb^+ ion that is exposed to EMM, which is theoretically proposed in [9]. Rabi flop temperature measurements are performed for different detunings of the cooling laser and EMM amplitudes. The experimental data is compared to the theoretical prediction.

2 Theoretical background

This first chapter provides important background information on the content of this thesis. Section 2.1 derives the motion of a single and multiple ions in a Paul trap. The theory of different laser cooling techniques in such a trap is presented in section 2.2 and section 2.3 describes a method to spectroscopically measure the temperature of a single ion that is used in this work.

2.1 Motion of ion crystals in a Paul trap

A radio frequency ion trap (also called a Paul trap) is used to spatially confine ions for the experiments performed in this thesis [6]. In general, due to Earnshaw's theorem, a charged particle cannot be confined in 3D using DC electric fields. In other words, the Laplace equation for source free DC electric fields $\Delta\Phi = 0$, with the Laplace operator Δ and the electric potential Φ, has no solutions that confine particles in all three spatial dimensions. To circumvent this, the Paul trap uses time-dependent electric fields. Four electrodes create an inhomogeneous quadrupole field in the x,y plane that alternates between confining and repulsive potential in the radio frequency (rf) regime. The resulting average net force in this plane pushes displaced ions towards the centre of the trap. Additional DC electrodes enclose ions along the z direction. Due to this electrode geometry, the electric field features a nodal line along the axial trap direction. If multiple ions are stored in the trap, they are commonly aligned along this axis, to reduce excess micromotion (see subsection 2.1.1). This alignment is achieved by choosing a weak DC confinement and a strong rf confinement. The trap axis along the nodal line is referred to as axial trap axis, while the other axes are referred to as radial trap axes. (depicted in figure 2.1).

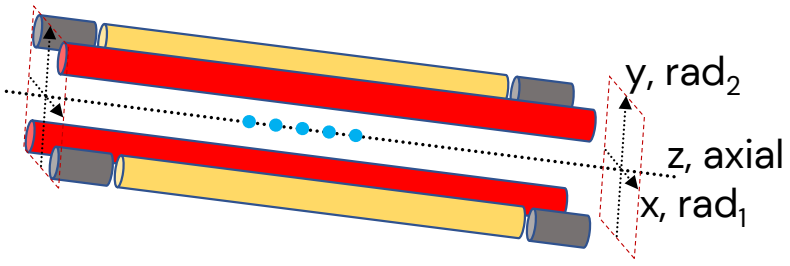

Figure 2.1: A schematic of a linear quadrupole Paul trap: The rf-field is applied to the red electrodes and the orange electrode segments are set to ground for radial confinement in x and y direction. Additional grey DC-electrode segments confine ions in the axial z direction. The blue dots represent a linear 5-ion crystal.

2.1.1 Single ion motion and equations of motion

The potential near the centre of a Paul trap with a static axial part Φ_{ax} and a radial part Φ_{rf} oscillating with a radio frequency $\Omega_{\mathrm{rf}}/(2\pi)$ can be described as

$$\Phi(\vec{r},t) = \underbrace{\frac{\kappa_{\mathrm{ax}}U_{\mathrm{ax}}}{2d_{\mathrm{ax}}^2}\left(2r_3^2-(r_1^2+r_2^2)\right)}_{\Phi_{\mathrm{ax}}} + \underbrace{\frac{\kappa_{\mathrm{rf}}U_{\mathrm{rf}}}{2d_{\mathrm{rf}}^2}\cos(\Omega_{\mathrm{rf}}t)\left(r_1^2-r_2^2\right)}_{\Phi_{\mathrm{rf}}}, \tag{2.1}$$

where U_{ax} and U_{rf} are the voltage amplitudes, that are applied to the respective electrodes. κ_{ax} and κ_{rf} are trap dependent geometric corrections of order unity, $2d_{ax}$ and $2d_{rf}$ are the distances between the respective electrodes. The indices 1,2,3 correspond to the spatial dimensions with 3 being the axial direction. Using

$$\frac{d^2r_i}{dt^2} = -\frac{e}{m}\frac{\partial\Phi}{\partial r_i} \qquad \text{and } i\in\{1,2,3\} \tag{2.2}$$

the equations of motion for a particle with mass m and charge e can be written as

$$\ddot{r}_i + (a_i + 2q_i\cos(\Omega_{\mathrm{rf}}t))\frac{\Omega_{\mathrm{rf}}^2}{4}r_i = 0. \tag{2.3}$$

Here a_i and q_i are dimensionless parameters commonly defined as:

$$\begin{aligned} q_1 = -q_2 &= \frac{2e\kappa_{\mathrm{rf}}U_{\mathrm{rf}}}{md_{\mathrm{rf}}^2\Omega_{\mathrm{rf}}^2}, \qquad q_3 = 0 \qquad \text{and} \\ a_{1,2} = -\frac{a_3}{2} &= -\frac{4e\kappa_{\mathrm{ax}}U_{\mathrm{ax}}}{md_{\mathrm{ax}}^2\Omega_{\mathrm{ax}}^2}. \end{aligned} \tag{2.4}$$

Equation (2.3) has the form of a *Mathieu* equation. Depending on the parameters a_i and q_i, this differential equation has stable solutions, where the charged particle remains in the trap. For $|a_i|$,$|q_i| \ll 1$, which is commonly chosen setting for Paul traps, the solution is

$$r_i(t) \cong r_{1,i}\cos(\omega_i t+\phi_i)\left(1+\frac{q_i}{2}\cos(\Omega_{\mathrm{rf}}t)\right). \tag{2.5}$$

This represents a so called *secular motion* in a harmonic, time-independent ponderomotive potential

$$\Phi_{\mathrm{pond}} \cong \frac{m}{2}(\omega_1^2r_1^2+\omega_2^2r_2^2+\omega_3^2r_3^2) \tag{2.6}$$

with the secular frequencies

$$\omega_i \cong \frac{\Omega_{\mathrm{rf}}}{2}\sqrt{a_i+\frac{q_i^2}{2}} \tag{2.7}$$

and phase ϕ_i modulated at the rf-frequency Ω_{rf} [10]. Motion of the particle with the rf frequency Ω_{rf} is referred to as *micromotion*. The secular frequencies ω_i summarize the confinement properties of the ponderomotive potential. Note that its radial part $\Phi_{\mathrm{pond,rad}} \sim m(\omega_1^2r_1^2+\omega_2^2r_2^2) \sim 1/m^2$ is mass dependent, while the axial direction $\Phi_{\mathrm{pond,ax}} \sim m\omega_3^2r_3^2 \sim 1$ is not, as $q_3 = 0$ (see (2.4)). The quantity q_3 being equal to 0 additionally means that ideal linear traps do not exhibit micromotion along the axial trap axis (see (2.5)). However, this is not the case for real traps, which usually have a micromotion component in the axial trap direction that needs to be taken into account and cannot be

compensated.
If a static external stray field $\vec{E}_{\mathrm{dc}}$ is present in the trap, the equation of motion is given by the inhomogeneous Mathieu equation:

$$\ddot{r}_i + (a_i + 2q_i \cos(\Omega_{\mathrm{rf}} t)) \frac{\Omega_{\mathrm{rf}}^2}{4} r_i = \frac{eE_{\mathrm{dc},i}}{m}. \tag{2.8}$$

This changes the solutions for the same parameters to

$$r_i(t) \cong (r_{0,i} + r_{1,i} \cos(\omega_i t + \phi_i)) \left(1 + \frac{q_i}{2} \cos(\Omega_{\mathrm{rf}} t)\right) \text{ [11]}. \tag{2.9}$$

The stray field displaces the charged particle from the trap centre about $\vec{r}_0$ causing additional micromotion. More specifically one defines the term proportional to $r_{0,i} \cos(\Omega_{\mathrm{rf}} t)$ as EMM (excess mircomotion) and the term proportional to $r_{1,i} \cos(\Omega_{\mathrm{rf}} t)$ as IMM (intrinsic mircomotion). The resulting EMM rf-field amplitude can be expressed in terms of the static stray field as follows

$$E_{\mathrm{rf},i} = \frac{q_i \Omega_{\mathrm{rf}}^2}{2\omega_i^2} E_{\mathrm{dc},i}. \tag{2.10}$$

Most trap experiments, which usually run on longer time scales than the fast oscillating micromotion, try to minimize the EMM and are less interested in the full ion trajectory. Therefore, micromotion is averaged out and omitted from the description of ion motion and only the secular motion as the solution of the time-independent potential Φ_{pond} is used instead.

2.1.2 Motional spectrum of a multi-ion crystal

If multiple ions are confined in a Paul trap and their kinetic energy is small compared to their Coulomb interaction energy, they form so-called *Coulomb crystals*. Their motion is governed by motional modes, which depend on the ions' masses and on their external confinement in the ponderomotive potential Φ_{pond}. A short derivation is presented this subsection. A more detailed derivation can be found in [12].
In the case of N ions in the trap at the positions $\vec{r}_i$ with masses m_i the total potential energy is given by

$$V_{tot} = \sum_{i=1}^{N} \Phi_{\mathrm{pond}}(\vec{r}_i, m_i) + \frac{1}{2} \sum_{\substack{i,j=1 \\ i \neq j}}^{N} \frac{e^2}{4\pi\epsilon_0 |\vec{r}_i - \vec{r}_j|}. \tag{2.11}$$

It consists of the single ion potential energies and the charged particles Coulomb interaction, which is the second term in (2.11) with the elementary charge e and the vacuum permittivity ϵ_0. To find the equilibrium positions $\vec{r}_{i,\mathrm{eq}}$ the potential is minimized by solving the set of equations

$$\frac{\partial V_{tot}}{\partial r_{ik}} = 0 \tag{2.12}$$

with the spatial dimension index k. Generally this needs to be done numerically.
Paul traps are commonly operated in the linear configuration, which requires a strong radial confinement and a comparably weak axial confinement. An estimate on the secular

trap frequency ratio $\alpha = \frac{\omega_{\text{rad}}}{\omega_{\text{ax}}}$, where the phase transition from a 1D to a 2D-crystal occurs for a given number of ions N is:

$$\alpha = \frac{\omega_{\text{rad}}}{\omega_{\text{ax}}} > 0.73N^{0.86} \text{ [13]}. \tag{2.13}$$

If the ratio is decreased further, the ions' equilibrium positions $\vec{r}_{i,0}$ can break out into the third dimension to form a 3D-crystal. Such higher dimensional crystals are also interesting for other research fields like solid-state physics as they make up a platform that can reproduce many properties of solid crystalline structures [14].
The next step in the derivation of the motional modes is the expansion of the potential in Eq. (2.11) to second order around the equilibrium positions. This results in

$$V_{tot} \approx \frac{1}{2}\sum_{k=1}^{3}\sum_{i,j=1}^{N} q_{ik}q_{jk}\left[\frac{\partial^2 V_{tot}}{\partial r_{ik}\partial r_{jk}}\right]_{r_{ik,\text{eq}}} = \frac{1}{2}\sum_{k=1}^{3}\sum_{i,j=1}^{N} q_{ik}q_{jk}H_{ijk}, \tag{2.14}$$

with the Hessian H and small deviations around the ions' equilibrium positions $\vec{q}$ defined as

$$\vec{q}_i(t) = \vec{r}_i(t) - \vec{r}_{i,\text{eq}}. \tag{2.15}$$

The $3N$ eigenmodes of the system can be found by solving the eigenvalue equation

$$\sum_{j=1}^{N} H_{ijk}\,\beta_{jk,\alpha} = \lambda_\alpha\, m_j\,\beta_{jk,\alpha}. \tag{2.16}$$

Here, the eigenvector component $\beta_{ik,\alpha}$ represents the normalized motional amplitude of ion i in eigenmode α. All possible motion of the trapped ions can be decomposed as a superposition of oscillations with the eigenfrequencies $\omega_\alpha = \sqrt{\lambda_\alpha}$ and amplitudes $\beta_{ik,\alpha}$. For a linear crystal, the motional modes separate into three sets of N modes on each trap axis. The motion in the axial direction and both radial directions does not couple and can therefore be treated and solved independently. This is not the case for higher dimensional crystals. An example of the motional modes for a mixed-species, a crystal with five ions is presented in figure 2.2.

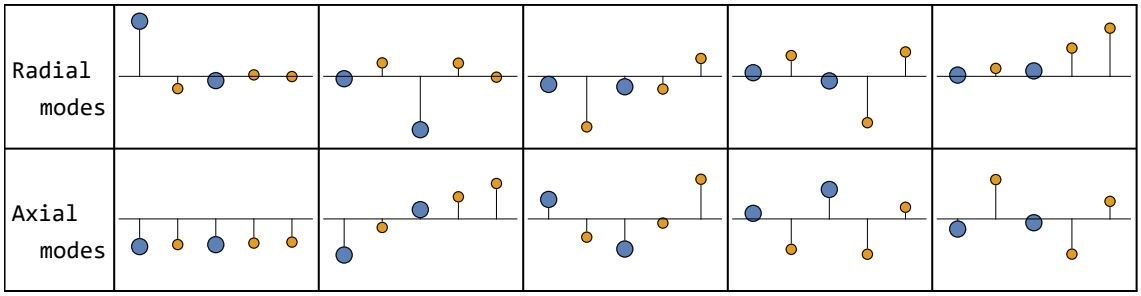

Figure 2.2: Radial and axial motional mode amplitudes of a 5-ion Coulomb crystals with two Yb^+ ions (blue) and three In^+ ions (yellow) in the (Yb^+, In^+, Yb^+, In^+, In^+) configuration.

For small energies, motional modes need to be treated quantum mechanically, which means that the motion appears in quantized states with distinct energies $E_{\alpha,n}$. In the trap, each

mode α forms a quantum mechanical harmonic oscillator system with states $|\alpha, n_\alpha\rangle$ and equidistant energy levels

$$E_{\alpha,n} = \hbar\omega_\alpha \left(n_\alpha + \frac{1}{2}\right) \quad \text{with } n_\alpha \in \mathbb{N}, \tag{2.17}$$

where ω_α ist the secular frequency. Here, n_α is the motional state quantum number denoting the excitation of mode α. The population of these states can be manipulated with lasers, which can be used for cooling, as explained in the next section.

2.2 Laser cooling

Once the ions are trapped, they are cooled using interactions with laser light. In order to reach temperatures close to absolute zero, the ions are laser cooled, because otherwise Doppler broadening [15] dominates in precision spectroscopy experiments. Heating processes can even result in a loss of the atom or ion if the temperature related kinetic energy exceeds the traps potential depth.
One of the simplest laser cooling schemes is Doppler cooling [16]. It relies on transferring decelerating momentum kicks from laser photons onto the atom or ion with absorption and emission processes. The scheme is limited by the randomly directed spontaneous photon recoil emission kicks, which leads to an ideal equilibrium Doppler temperature of

$$T_D = \frac{\hbar\Gamma}{2k_B}, \tag{2.18}$$

where Γ is the linewidth of the atoms cooling transition and k_B the *Boltzmann* constant [17]. To cool the ions to T_D, the cooling laser is detuned to $-\Gamma/2$ with respect to the cooling transitions resonance. Commonly chosen ions have cooling transitions with linewidths of approximately 20 MHz to scatter many photons on the cooling transition and cool efficiently. On the other hand, the large natural linewidth also results in an increased minimum temperature that can be achieved through Doppler cooling.
Cooling is also applicable to multi-ion crystals even if not all ions are directly addressed by the cooling laser. As the Coulomb interaction couples the individual ions motion, the cooling effect on the directly cooled ions is distributed throughout the crystal. This is known as sympathetic cooling, which can be used to cool co-trapped species that may not have accessible laser cooling transitions [5].
Another cooling technique that reaches even lower temperatures than Doppler temperature is continuous sideband (SB) cooling [18]. It uses the coupling of the motional states $|n\rangle$ and the internal states $|g\rangle$ and $|e\rangle$ of an ion exposed to laser radiation. Here, $|g\rangle$ refers to the ground state and $|e\rangle$ refers to an excited state. A laser with a sufficiently small linewidth can drive transitions from $|g, n\rangle$ to $|e, n'\rangle$ changing the motional state number, if the internal state linewidth $\Gamma_0 \ll \omega_{\text{sec}}$, where ω_{sec} is the secular frequency. For a carrier transition ($\Delta n = n' - n = 0$), the laser is detuned to $\omega_{\text{L}} = \omega_0$ with $\hbar\omega_0$ being the energy difference between the atomic internal states. For a first order blue (red) sideband transition with motional state difference $\Delta n = +1 (\Delta n = -1)$, the laser is detuned to $\omega_{\text{L}} = \omega_0 + \omega_{\text{sec}} (\omega_{\text{L}} = \omega_0 - \omega_{\text{sec}})$. A spectroscopic measurement of the three transitions on the $^2\text{S}_{1/2} \rightarrow ^2\text{D}_{5/2}$ transition of a trapped $^{172}\text{Yb}^+$ ion is shown in figure 2.3. The detailed spectroscopy sequence for this experiment is described in subsection 3.2.1.

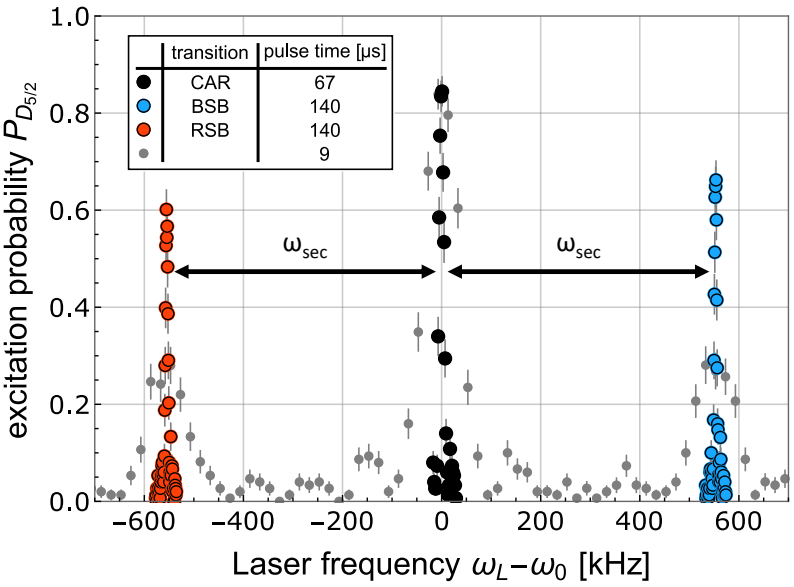

Figure 2.3: Spectroscopy measurement of the $^2S_{1/2} \rightarrow ^2D_{5/2}$ transition of an $^{172}Yb^+$ ion with the natural linewidth of $\Gamma_0 = 2\pi\, 22.7\,\text{Hz}$. Here the $^2S_{1/2}$ state represents the ground state $|e\rangle$ and the $^2D_{5/2}$ state the excited state $|g\rangle$. The scan with black data points corresponds to the carrier transition and the red and blue scans to the first red and blue sideband transitions. The grey data points represent a frequency scan with high laser power to localize the individual transitions. The sidebands can be resolved as $\Gamma_0 \ll \omega_{\text{sec}} \approx 2\pi\, 560\,\text{kHz}$.

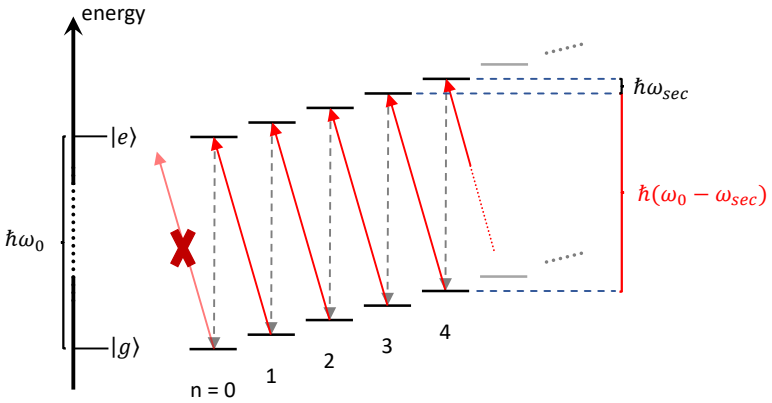

Figure 2.4: The schematic level structure of sideband cooling: The red arrows represent a RSB transition from the electronic ground state $|g, n\rangle$ in the harmonic oscillator state with quantum number n to the excited state $|e, n-1\rangle$. Additionally, ω_0 is the carrier transition frequency between the ground $|g\rangle$ and excited $|e\rangle$ state of the ion, and ω_{sec} is the secular frequency. The frequency of the RSB transition is $\omega_0 - \omega_{\text{sec}}$. The grey dashed arrows represent spontaneous decay events into $|g\rangle$. Consecutive cycles of both transition types transfer the population from all upper motional states with $n \geq 1$ to $|g, 0\rangle$. In this state, the cooling process ends as the RSB transition does not couple to an existing state anymore.

For continuos SB cooling, which is schematically shown in figure 2.4, a laser drives the resolved RSB transition of an ion repeatedly reducing the ions motional energy on average by $\hbar\omega_{\text{sec}}$ per absorbtion-emission cycle. Additionally the excited internal state is quenched

with a laser to increase the decay rate into the ground state to fasten the cooling rate. After several repetitions, the ion occupies the motional ground state with a high probability, which can be related to temperatures much lower than the Doppler limit (see more information about the temperature of ions within a trap in section 2.3).

2.3 Measuring temperatures with Rabi flops

Chapter 6 presents experiments that require a more detailed quantum mechanical explanation of the interaction between the spectroscopy laser and a trapped ion. These experiments are based on the evaluation of Rabi flops to determine the ion's temperature. The expression for a Rabi flop is derived here following [19].
Starting from the Schrödinger equation with the particles wavefunction Ψ and the Hamiltonian $\boldsymbol{H}$

$$i\hbar\frac{\partial\Psi}{\partial t} = \boldsymbol{H}\Psi, \tag{2.19}$$

a two level system with states $|g\rangle$, $|e\rangle$ and energies $E_g = \hbar\omega_g$, $E_e = \hbar\omega_e$ has the solution

$$\Psi(\vec{r},t) = c_g(t)\,|g\rangle\,e^{-i\omega_g t} + c_e(t)\,|e\rangle\,e^{-i\omega_e t}. \tag{2.20}$$

Here c_g and c_e are coefficients that describe the probability amplitude to find the particle in the respective states. They are normalized so that $|c_g|^2 + |c_e|^2 = 1$. If one adds a pertubative oscillating electric field $\vec{E}(t) = \vec{E}_0\cos(\omega_\mathrm{L}\,t)$ that represents laser radiation with amplitude $\vec{E}_0$ and frequency ω_L, an additional interaction Hamiltonian $\boldsymbol{H}_I(t) = e\,\vec{\boldsymbol{r}}\cdot\vec{E}(t)$ with the position operator $\vec{\boldsymbol{r}}$ transforms the differential equation for the coefficients to

$$i\frac{\partial}{\partial t}\begin{pmatrix} c_g \\ c_e \end{pmatrix} = \begin{pmatrix} 0 & \Omega\cos(\omega_\mathrm{L}\,t)\,e^{-i\omega_0 t} \\ \Omega^*\cos(\omega_\mathrm{L}\,t)\,e^{i\omega_0 t} & 0 \end{pmatrix}\begin{pmatrix} c_g \\ c_e \end{pmatrix}. \tag{2.21}$$

Here $\omega_0 = \omega_e - \omega_g$ is the internal state frequency difference and Ω the *rabi frequency*. This quantity is defined as

$$\Omega = \frac{e\,\langle g|\,\vec{\boldsymbol{r}}\cdot\vec{E}_0\,|e\rangle}{\hbar} \tag{2.22}$$

and describes the coupling between the laser and the two-level atom.
A rotating-wave approximation is applied, where one neglects fast oscillating terms with frequency $\omega_\mathrm{L} + \omega_0$ that average out over reasonable interaction times and keeps the slower oscillating terms with frequency $\Delta = \omega_\mathrm{L} - \omega_0$, which is the detuning between the laser frequency and the atomic transition frequency. The probability P to find the particle in the excited state $|e\rangle$ as a function of time is $P(|e\rangle)(t) = |c_e(t)|^2$. Starting with all of the population in the ground state $|g\rangle$, which means $c_g(0) = 1$ and $c_e(0) = 0$,

$$|c_e(t)|^2 = \frac{\Omega^2}{\Omega^2+\Delta^2}\,\sin^2\left(\frac{\sqrt{\Omega^2+\Delta^2}\,t}{2}\right) \overset{\Delta=0}{=} \sin^2\left(\frac{\Omega t}{2}\right) \tag{2.23}$$

solves the differential equation (2.21) with the applied rotating-wave approximation. This describes an oscillation of the population of $|e\rangle$ between 0 and $\Omega^2/(\Omega^2+\Delta^2)$ with the frequency $\sqrt{\Omega^2+\Delta^2}$ over time and is known as Rabi flopping. Only if the laser frequency ω_L matches the atomic transition frequency ω_0 ($\Delta = 0$) a total excitation of the upper state ($|c_e(t)|^2 = 1$) is possible. This only holds for ideal lasers with infinite coherence

times and monochromatic light. Otherwise, decoherence is present and the oscillations amplitude is damped out to zero and a stationary excitation of $|c_e(t)|^2 = |c_g(t)|^2 = 1/2$ is reached.
As discussed in the previous subsections, the motional states of an ion in the confining trap potential couple to the ion's internal states. Each motional state in the internal ground state $|g, n\rangle$ has a different coupling strength or Rabi frequency $\Omega_{n,n'}$ to its corresponding excited state, which is given by

$$\Omega_{n,n'} = \Omega\, \mu_{n,n+\Delta n} = \Omega\, e^{-\frac{1}{2}\eta^2} \sqrt{\frac{n_<!}{(n_< + \Delta n)!}} (i\eta)^{\Delta n} L_{n_<}^{\Delta n}(\eta^2) \tag{2.24}$$

with the free ion Rabi frequency Ω, $n_< = \{n, n'\}_{min}$, the Lamb Dicke parameter η and a generalized Laguerre polynomial $L_n^{\Delta n}(x)$. The Lamb Dicke parameter quantifies the potential influence of photon recoil onto motional states of an ion in a trap, but this is not discussed further as it is not relevant for the rest of this thesis [20]. Equation (2.23), which states the probability to find the ion in the excited state after time t starting from the ground state, can be extended to

$$P(|e\rangle)(t) = \sum_{n=0}^{\infty} P_n \sin^2\left(\frac{\Omega_{\text{int}}\, \mu_{n,n+\Delta n}}{2}\, t\right) \tag{2.25}$$

with the probability P_n of the ion to be in the motional state $|g, n\rangle$. In thermal equilibrium[1] the state distribution P_n for small mean phonon number $\bar{n}$ is approximated by

$$P_n(\bar{n}) = \frac{1}{\bar{n}+1}\left(\frac{\bar{n}}{\bar{n}+1}\right)^n \quad [21]. \tag{2.26}$$

Inserting this into (2.25) leads to

$$P(|e\rangle)(t) = \frac{1}{\bar{n}+1} \sum_{n=0}^{\infty} \left(\frac{\bar{n}}{\bar{n}+1}\right)^n \sin^2\left(\frac{\Omega_{\text{int}}\, \mu_{n,n+\Delta n}}{2}\, t\right), \tag{2.27}$$

which is a function of $\bar{n}$. If one neglects high motional states above a limit n_{lim}, where $P_n \to 0$ for $n > n_{\text{lim}}$, this function can be fitted to a Rabi flop to determine the mean motional state number of the ion. As this quantity can be related to the temperature T with

$$T = \frac{\hbar \omega_{\text{sec}} \bar{n}}{k_B}, \tag{2.28}$$

this method can be used to evaluate ion temperatures in cooling experiments spectroscopically, which is used in chapter 6.
Figure 2.5 presents the measurement of Rabi flops with Doppler cooling only and additional SB cooling (section 2.2) on the $^2S_{1/2} \to {}^2D_{5/2}$ transition of an $^{172}Yb^+$ ion. Both spectroscopy sequences are described in subsection 3.2.1. To compensate effects like the excited state decay due to finite detection times or experimental imperfections, an amplitude C_1 and an offset C_2 are added as free parameters to (2.27)

$$P(|e\rangle)_{\text{exp}}(t) = C_1 \cdot \left[\frac{1}{\bar{n}+1} \sum_{n=0}^{\infty} \left(\frac{\bar{n}}{\bar{n}+1}\right)^n \sin^2\left(\frac{\Omega_{\text{int}}\, \mu_{n,n+\Delta n}}{2}\, t\right)\right] + C_2. \tag{2.29}$$

[1] The ions motional states are in thermal equilibrium due to Doppler cooling.

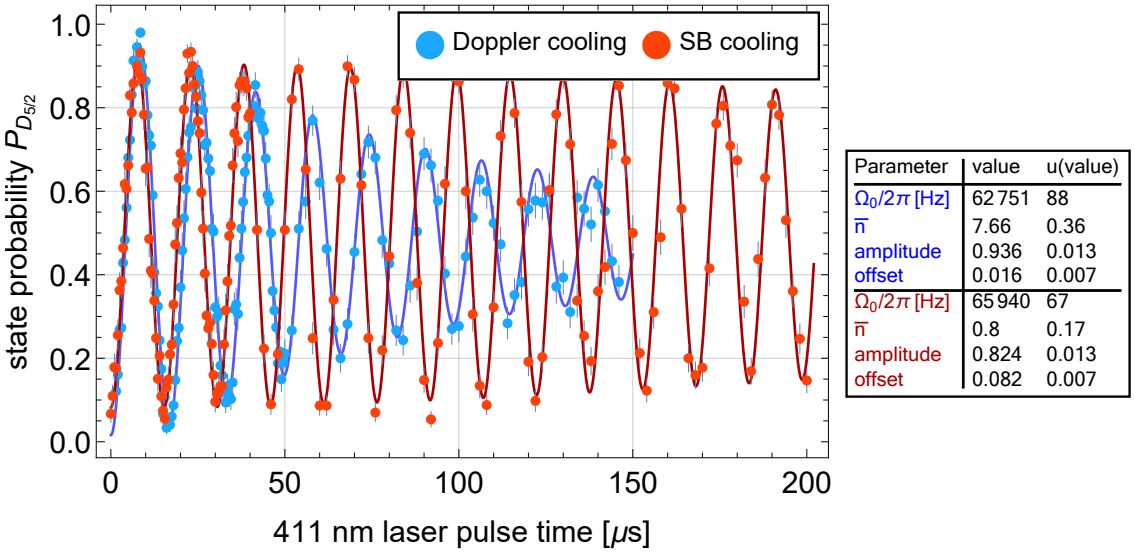

Parameter	value	u(value)
$\Omega_0/2\pi$ [Hz]	62 751	88
$\bar{n}$	7.66	0.36
amplitude	0.936	0.013
offset	0.016	0.007
$\Omega_0/2\pi$ [Hz]	65 940	67
$\bar{n}$	0.8	0.17
amplitude	0.824	0.013
offset	0.082	0.007

Figure 2.5: A Doppler cooled Rabi-Flop in blue and SB cooled Rabi Flop in red on the $^{172}Yb^{+}$ $^{2}S_{1/2} \rightarrow {}^{2}D_{5/2}$ carrier transition evaluated with (2.29) in the table.

This function is fitted to the Rabi flops in figure 2.5. The fit results in a mean motional state number $\bar{n} = 7.66 \pm 0.36$ for Doppler cooling and $\bar{n} = 0.8 \pm 0.17$ for SB cooling. The respective free ion Rabi frequencies are $\Omega_0/2\pi = (62.751 \pm 0.088)\,\mathrm{kHz}$ and $\Omega_0/2\pi = (65.940 \pm 0.067)\,\mathrm{kHz}$.

3 Experimental setup

This chapter gives an overview over the experimental setup that is used for the experiments in this thesis. Section 3.1 presents a schematic drawing of the setup and introduces important parts of the setup afterwards. Section 3.2 describes standard spectroscopy sequences and the results of a heating rate measurement.

3.1 Experimental setup

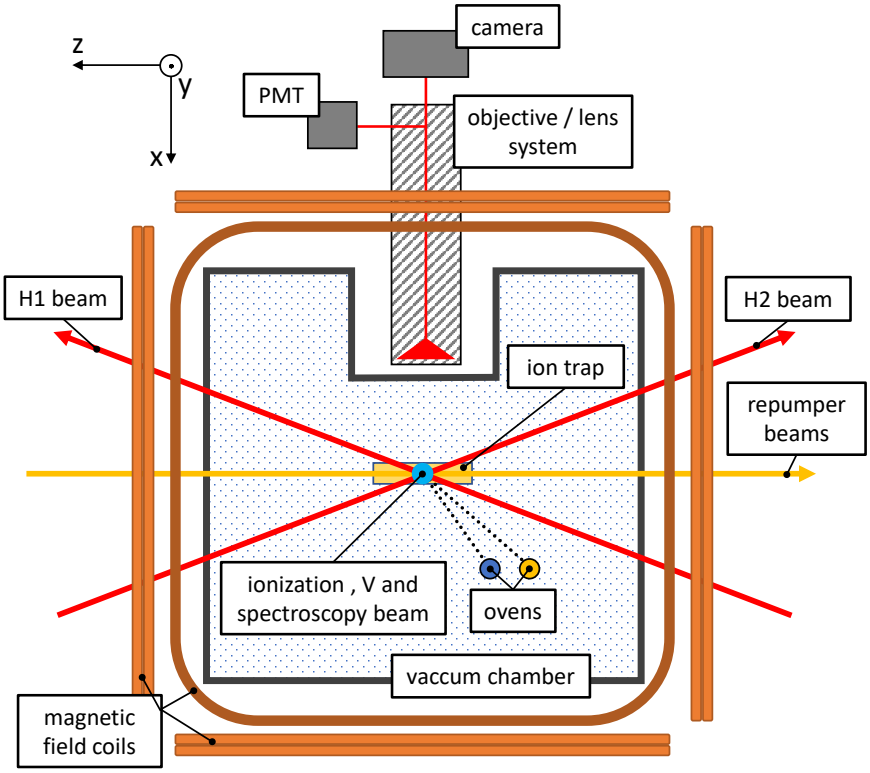

Figure 3.1: Schematic drawing of the experimental setup from above. The centre of the setup is the ion trap enclosed in a vacuum chamber. Trapped ions are manipulated and cooled with the H1, H2, V, repumper and spectroscopy lasers. The magnetic field in the trap is controlled by coils attached to the chamber. A lens system refracts scattered light onto a camera and a photomultiplier tube to detect ions. Metal ovens and the ionization laser are used to store ions in the trap.

Figure 3.1 presents important components of the experimental ion trap setup. The following subsections describe the referenced components more detailed. See subsection 3.1.1 for the ion trap, subsection 3.1.2 for the vacuum chamber, the optical setup and the ovens and subsection 3.1.3 for the detection system.

3.1.1 Ion trap

The ion trap implemented in this setup consists of four gold coated chips made of aluminium nitride and provides eight trap segments, each of which can trap ions [22]. Each segment has six electrodes, which provide and control the radial confinement in the respective segment. Figure 3.2 shows a schematic of a radial cut of the trap. An AC radio frequency field is applied to two of the inner four electrodes to confine trapped ions radially. The rf-field with a frequency of $\sim 16.4\,\mathrm{MHz}$ and an amplitude in the low kV regime, is generated by an rf signal generator and amplified by a helical resonator with a Q factor of 590.
Additionally, the four DC-voltage components $U_\mathrm{e}, U_\mathrm{t}, U_\mathrm{ec}$ and U_tc are applied on the other four non-rf electrodes. U_e and U_t rotate the principle radial axes, U_ec and U_tc shift the ion in the radial plane [22]. In this way, occurring stray charges and the resulting micromotion can be compensated by shifting the ions back to the trap centre. Axial confinement is provided by applying DC voltages to the neighbouring segments.

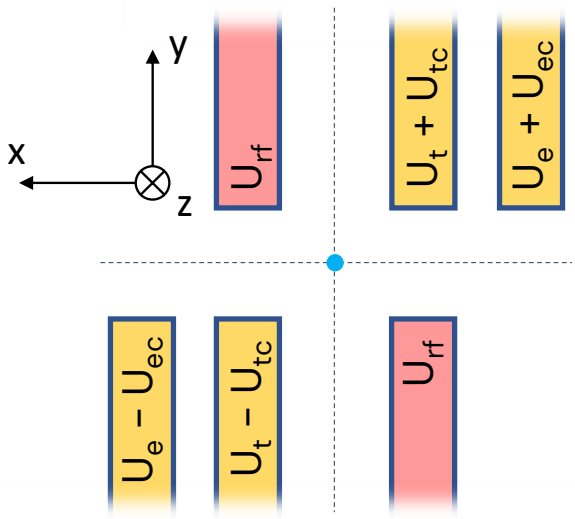

Figure 3.2: Schematic view of a radial cut through the trap. The radio frequency voltage U_rf is applied to two of the of six electrodes for radial confinement. The DC voltages (U_t, U_e, U_ec and U_tc) are applied on the other four electrodes (yellow) to determine the trap centre and the trap axis orientation.

3.1.2 Vacuum chamber and optical setup

Vaccum chamber

Vacuum or vacuum chambers are necessary for all experiments that isolate and control single and multiple atoms. By establishing a low pressure environment in the $10^{-11}\,\mathrm{mbar}$ regime [22], the probability of uncontrolled collisions and interactions of the ions with residual particles is reduced. A titanium octahedral chamber is used in this experiment as it allows for plenty of optical access to laser beams from different directions.
Around the chamber, two current carrying coils are assembled in a Helmholtz like configuration for each spatial dimension. They are optimized for a homogenous magnetic field

across a large trapping region while, at the same time, being as compact as possible. This allows one to control the magnetic field in the centre of the trap and apply the different magnetic field strengths in different directions as required for spectroscopy.

Yb^+ term scheme and laser setup

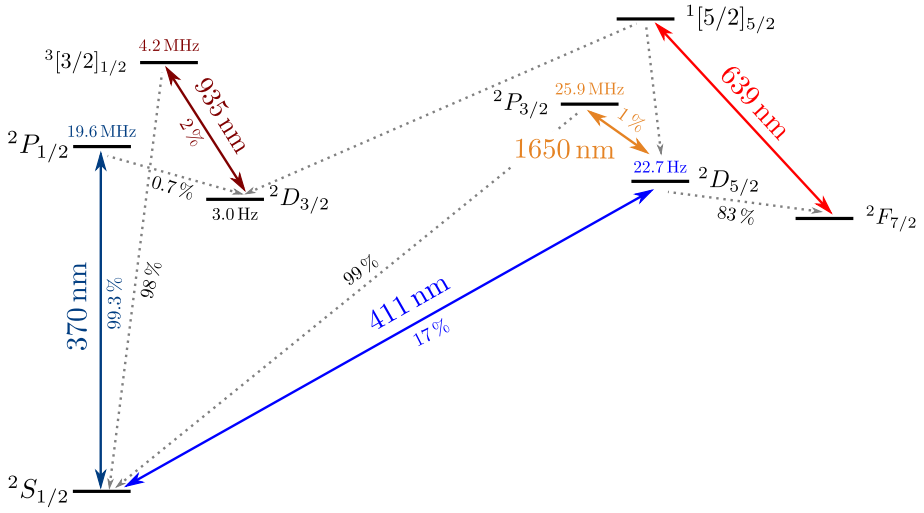

Figure 3.3: Ytterbium ion term scheme with relevant states and decay rates. The transitions, that are driven with lasers, are presented with their corresponding wavelengths. This includes the 370 nm cooling laser, the 411 nm spectroscopy laser and the repump lasers with the wavelengths 935, 638 and 1650 nm. Picture used with permission from [23].

All experiments in this setup are performed with ytterbium as the cooling ion and indium as the clock ion. This thesis only covers direct experiments on ytterbium, which is why only the ytterbium term scheme (figure 3.3) and the relevant lasers are shown and described here. Indium ions are sympathetically cooled using Ytterbium ions and are not directly addressed by any lasers for the experiments in this thesis.
Yb^+ ions feature a convenient cooling transition from $^2S_{1/2}$ to $^2P_{1/2}$ level with a linewidth of 19.6 MHz. The energy difference of the transition corresponds to photons with a wavelength of 370 nm, which is provided by laser light, that enters the trap via the H1, H2 and V beams (see figure 3.1) to cool Yb^+ in all spatial dimensions. The 411 nm spectroscopy laser drives the $^2S_{1/2}$ to $^2D_{5/2}$ quadrupole transition of ytterbium and enters the trap in the y-direction. The transition has a comparably small natural linewidth of 22.7 Hz and is used for sideband cooling. The 822 nm laser, which is frequency doubled to the 411 nm laser afterwards, is stabilized on a ULE cavity [23] to ensure a sufficient frequency stability of this laser. The two excited states $^2P_{1/2}$ and $^2D_{5/2}$ do not always decay back in to the ground state, which make the 935 nm and the 639 nm repump lasers necessary to keep the ytterbium ion in the cooling- and spectroscopy cycle. The 1650 nm laser is used to quench the spectroscopy transition, if SB cooling is applied (see section 2.2). The repump lasers enter the trap in the axial trap direction (z axis). Ytterbium is ionized during the loading process by the 399 nm laser, which enters the trap vertically from below the chamber. All lasers are focused to the centre of the trap. More detailed information on the lasers, their implementation in the experiment and other technical details can be found in [23].

Ion loading and ovens

Both ion species are loaded via thermal oven loading. The ovens are heated by currents running through the respective oven enclosure which vaporizes the solid purified metal pieces inside. As Yb has a higher vapour pressure than In, oven currents of 9 A and 11 A are used to heat the Yb and In samples to ensure a high enough flux of the atomic beams. A 400 µm diameter aperture in front of the ovens collimates the neutral atomic beams pointing towards the traps loading segment, where the atomic beams overlap with the respective ionization lasers. A second aperture is added to prevent coating of the ion trap. The 399 nm ionization laser for Yb^+ and the 410 nm ionization-laser for In^+ ionize the hot neutral atoms in combination with the 370 nm ytterbium cooling laser via a two photon absorption process. After ionization, the ions can be captured by the trapping potential of the ion trap.

3.1.3 Detection system

Photons scattered on the cooling transition of Yb^+ are collected by an objective consisting of 5 lenses [24], which is assembled in front of a reentrant viewport outside of the vacuum chamber. With a working distance of 31 mm [24], the system collects 2 % of the solid angle of the scattered light and has a numerical aperture of ≈ 0.27. About 50 % of the collected florescence is detected by a photon multiplier tube (PMT) and the other 50 % by an EMCCD camera (see figure 3.1). The lens system's magnification M is about 24, the camera chip holds 512 x 512 pixels and each pixel has a width of $d_{\mathrm{px}} = 16\,\mu\mathrm{m}$, which results in a resolution of $d_{\mathrm{px}}/M = 0.692\,\frac{\mu m}{\mathrm{px}}$ in the camera picture. The PMT has no spatial resolution but is more sensitive to smaller photon numbers. In this experimental setup, the PMT is also used to measure excess micromotion with the photon correlation method [23].

3.1.4 Experimental Control

The experimental control PC runs the C++-based program MCP[1], which provides a GUI and methods to communicate with different experimental hardware. Time critical experiments are controlled by ARTIQ [25], which uses an FPGA to ensure nanosecond resolution timing of the experimental sequences.

3.2 Spectroscopy sequences and heating rate of the ion trap

The previous section introduced relevant experimental parts. This section presents the spectroscopy sequences used in all spectroscopy experiments in this work. Furthermore the measurement of the heating rate of a single Yb^+ ion in the ion trap is shown, which is an important quantity for characterizing ion traps and relevant for the presented measurements in chapter 6.

3.2.1 Spectroscopy sequences

In this thesis different spectroscopy experiments are performed that evaluate the probability to excite the $^2S_{1/2} \rightarrow {}^2D_{5/2}$ transition of a single Yb^+ ion. Each cycle of the experiment

[1] MCP or *master control program* is developed by Prof. Kilian Singer and is unpublished.

consists of several operations that include state preparation, interrogation and detection. The individual operations require precise timing and are depicted schematically in figure 3.4. A cycle starts with a *reference image* to determine if the Yb^+ ion is in the ground

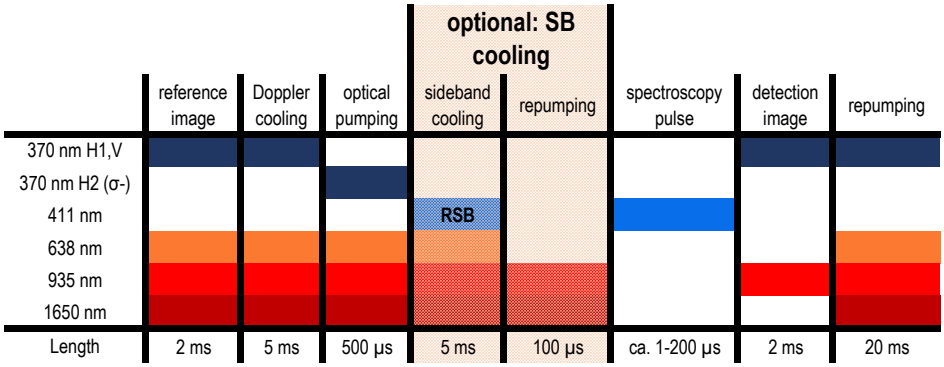

Figure 3.4: Standard spectroscopy scheme consisting of the following phases: reference image, Doppler cooling, optical pumping, optional SB cooling and repumping, a spectroscopy pulse, a detection image and a repumping phase. It is only shown whether the lasers, which are identified by their wavelengths and colors, contribute to the respective phases or not. See more information on the lasers in subsection 3.1.2 and information on the cooling techniques in section 2.2.

state with the electron shelving technique [26]. For this technique the ion is illuminated with the laser that addresses the $^2S_{1/2} \rightarrow ^2P_{1/2}$ Yb^+ cooling transition. If the ion is in its ground state, the photons are scattered on this transition and the ion can be detected by the detection system. If the ion is not in the ground state, no photons are scattered and the cycle is disregarded. Afterwards, the ion is cooled for 5 ms, where the laser parameters are optimized to reach Doppler temperature. Next, the ion is *optically pumped* into one of the $m_F = \pm 1/2$ Zeeman states of the ions ground state by applying $\sigma^{\pm}$-polarized light on the cooling transition with the H2 beam.
In case the experiment requires additional SB cooling, a 5 ms laser pulse of the spectroscopy laser is applied to the first red sideband of the $^2S_{1/2} \rightarrow {}^2D_{5/2}$ transition to cool the ion to it's motional ground state. Additionally the transition is quenched using the 1650 nm laser to accelerate the transfer back to the internal ground state, which SB cools the ions more efficiently. After the SB pulse, a 100 µs pulse of the 1650 nm and 935 nm lasers repumps remaining state population to the electronic ground state. Note that the SB pulse does not substitute Doppler cooling but is used as a second cooling phase, as Doppler cooling is much more efficient until the Doppler temperature is reached.
Afterwards the *spectroscopy pulse* with a chosen frequency, power and pulse length is applied to ensure a probability p to excite the ions to the $^2D_{5/2}$ state. Directly after, a *detection image* is taken to determine weather the ion was excited or not. The sequence ends with a *repumping* pulse of 20 ms, which ensures that the ion is back in the ground state before the sequence restarts. The cycle is repeated about 200 times. The excitation probability is given by the ratio between the number of cycles where the ion was excited to the $^2D_{5/2}$ state, and the total number of valid cycles.

3.2.2 Heating rate of the ion trap

Chapter 6 investigates a heating process of a single Yb^+ ion due to cooling under excess micromotion (see details in section 6.2). The evaluation of this experiment requires a measurement of the trap dependent heating rate of the ion due to electronic noise on the trap electrodes, to distinguish between the two. The heating rate generally decreases with an increasing secular frequency and distance of the ion to the trap electrodes. The measurement technique and the results of such a measurement in the experimental setup are presented in this subsection.
To measure the heating rate, a waiting time where no laser light is present, is introduced to the spectroscopy sequence between SB cooling and spectroscopy pulses (see figure 3.4). Afterwards the temperature of the ion is evaluated for different waiting times to measure the effect of the heating process on the ion. The result of the heating rate measurement at a secular frequency of $\omega_{\text{sec}} = 2\pi\,1028\,\text{kHz}$ for waiting times from 0 to 1 s is shown in figure 3.5. The mean phonon number $\bar{n}$ after the respective waiting times is evaluated by comparing the excitation probabilities of the blue motional sideband A_{BSB} and the red motional sideband A_{RSB} of the $^2S_{1/2} \rightarrow ^2 D_{5/2}$ transition, using the formula

$$\bar{n} = \frac{1}{\frac{A_{\text{RSB}}}{A_{\text{BSB}}} - 1} \text{ [27]}. \tag{3.1}$$

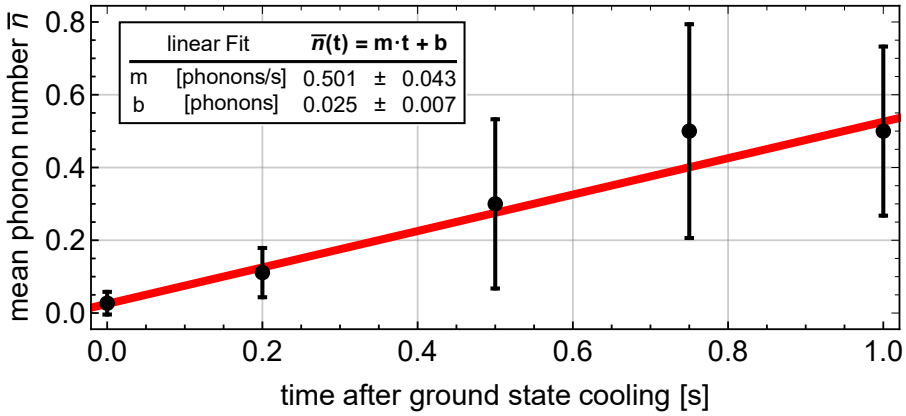

Figure 3.5: Result of a heating rate measurement at $\omega_{\text{sec}} = 2\pi\,1028\,\text{kHz}$: The five data points represent individual mean phonon number measurements with respective waiting times after SB cooling. The data are fitted with a linear function $\bar{n}(t) = m \cdot t + b$, which evaluates the heating rate and the starting temperature.

The linear fit gives a rate of $m = 0.5\,\text{phonons/s}$ and a starting temperature of $b = \bar{n}_{\text{start}} = 0.025\,\text{phonons}$. The value of the intercept depends on the efficiency of the SB cooling step. A higher efficiency of SB cooling ensures a lower intercept. This heating process happens on a much lower timescale than the temperature measurements in chapter 6 and can therefore be neglected.

4 Cooling rates for mixed-species ion Coulomb crystals

The results presented in this chapter are based on research published in [4]. While the previous investigations derived the properties of a fixed ion crystal configuration with a focus on relevant systematic shifts for an ion clock, this work compares different configurations with a particular focus on Doppler cooling times. Here the *composition* of a crystal defines the respective quantities of cooling ions (ytterbium ions) and clock ions (indium ions) and *configuration* means the specific order of the ions. The theoretical model and assumptions are presented and motivated in section 4.1. It also shows that the mentioned motional shifts change less between configurations and thus play a less decisive role in comparison to cooling times. A detailed and systematic analysis of the dependencies of cooling times on different parameters follows in section 4.2. Section 4.3 presents how different finite cooling times starting from a non-equilibrium mode-temperature affect motional shifts with a simple time-dependent model.
Finally, section 4.4 compares the results with an alternative code to give an additional outlook on cooling times for 2D and 3D configurations.

4.1 Configuration dependence of cooling times and systematic shifts

Before systematically analysing cooling rates of Coulomb crystals, this section covers the theoretical model and defines relevant quantities. It also motivates the use of cooling times - rather than motional frequency shifts - as the figure of merit for the optimization of trap parameters and configurations. Subsection 4.1.3 shows that these motional shifts, which are generally very important for atomic clock operation, do not vary significantly in the investigated parameter space. Subsection 4.1.4 reviews some geometric properties of motional modes of multi-ion Coulomb crystals to provide some intuitive insight into the results of the calculations in this chapter. Lastly subsection 4.1.5 gives a short overview of the calculations of the cooling times for an example composition $(n_{\mathrm{Yb}^+}, n_{\mathrm{In}^+}) = (3, 10)$. This example composition was also used for analysis in [4], which allows for a direct comparison of the results presented in this section. Other properties are explained on the bases of a $(n_{\mathrm{Yb}^+}, n_{\mathrm{In}^+}) = (5, 5)$ composition.

4.1.1 Theoretical model

A *Mathematica* code was written to simulate the cooling times for different configurations. First, the radial and axial equation of motion in a linear Paul Trap are solved for a given set of ions in a linear chain and trap parameters using precalculated equilibrium positions. The code is solves the EOM for one dimensional crystals and also handles the radial and

axial directions separately[1]. Motional mode equilibrium temperatures and cooling rates are derived by setting the sum of energy rates involved in the Doppler cooling process to zero:

$$\dot{E}^{\alpha}_{\text{cool,laser}} + \dot{E}^{\alpha}_{\text{heat,laser}} + \dot{E}^{\alpha}_{\text{heat,ext}} = 0 \qquad \text{for mode } \alpha. \tag{4.1}$$

$\dot{E}^{\alpha}_{\text{cool,laser}}$ and $\dot{E}^{\alpha}_{\text{heat,laser}}$ represent the laser induced cooling rate from photon absorption events and heating due to spontaneous emission momentum kicks. The sum of these rates can be expressed as product of the scattering rate Γ_{sc} and the effective kinetic energy difference ΔE. The external rate $\dot{E}^{\alpha}_{\text{heat,ext}}$ accounts for all non laser related heating processes, which are governed by electric field noise in this trap. It is measured experimentally with a single Yb^+ ion and extrapolated to higher order modes and multi-ion crystals by projecting the individual mode vectors onto the E-field vector [4]. In equilibrium, the ion's velocity distribution in each mode can be assumed to follow the Maxwell-Boltzmann distribution and can therefore be related to a mode temperature T_α. This allows to express the velocity dependent cooling rate in terms of T_α, which leads to

$$T_\alpha = -\frac{\dot{E}^{\alpha}_{\text{heat,ext}} + \Gamma_{\text{sc},0}\frac{1}{2}\left((\hbar k_\alpha)^2 + \frac{(\hbar k)^2}{3}\right)\sum_i \frac{\beta'^2_{\alpha,i}}{m_i}}{k_B \Gamma_{\text{sc},0}\rho_\alpha \hbar k_\alpha \sum_i \frac{\beta'^2_{\alpha,i}}{m_i}}. \tag{4.2}$$

Here $\Gamma_{\text{sc},0}$ and ρ_α are coefficients obtained by a linearization of the scattering rate $\Gamma_{\text{sc}} \approx \Gamma_{\text{sc},0}(1 + \vec{\rho}\cdot\dot{\vec{r}})$ [28] for small ion velocities with the radiation pressure $\vec{\rho}$, k_α is the projection of the wave vector $\vec{k}$ onto the $\alpha-$mode vector, k the projection of $\vec{k}$ onto the ion's momentum, $\beta'_{\alpha,i}$ (see (2.16)) corresponds to the normalized eigenvector component of the ion position number i for mode α in mass weighted space, m_i the mass of ion i and k_B the Boltzmann constant. It is important to point out that sum only runs over the cooling ions' indices. In a rather simple model, one can assume a rate of change of the mode temperature $\dot{T}_\alpha(t)$ proportional to the difference between the equilibriums temperature and the current temperature $T_\alpha - T_\alpha(t)$. An exponential decrease towards the mode's equilibrium temperature with temperature independent constant cooling rates $\dot{E}^{\alpha}_{\text{cool,const}}$ solves this:

$$T_\alpha(t) = (T_{start} - T_\alpha)\cdot e^{-\frac{\dot{E}^{\alpha}_{\text{cool,const}}}{k_B T_\alpha}t} + T_\alpha \tag{4.3}$$

The cooling rate is calculated as

$$\begin{aligned}
\dot{E}^{\alpha}_{\text{cool,const}} &\overset{\text{in equil.}}{=} \dot{E}^{\alpha}_{\text{cool,laser}} && \text{(4.4a)}\\
&= -(\dot{E}^{\alpha}_{\text{heat,laser}} + \dot{E}^{\alpha}_{\text{heat,ext}}) && \text{(4.4b)}\\
&= -\dot{E}^{\alpha}_{\text{heat,ext}} - \Gamma_{\text{sc},0}\frac{1}{2}\left((\hbar k_\alpha)^2 + \frac{(\hbar k)^2}{3}\right)\sum_i \frac{\beta'^2_{\alpha,i}}{m_i} && \text{(4.4c)}
\end{aligned}$$

Within this model one can define a 1/e cooling time

$$\tau_\alpha = \frac{k_B T_\alpha}{\dot{E}^{\alpha}_{\text{cool,const}}}. \tag{4.5}$$

[1]The code produces non-physical imaginary solutions for secular frequency ratios that correspond to 2D or 3D crystal conditions.

These mode dependent equilibrium temperatures and cooling rates depend on external trap parameters like the ions' confinement in radial and axial direction but also the composition and the configuration of the Coulomb crystal, as analysed in the next section. General calculation settings and parameters are discussed in the next subsection.

4.1.2 General calculation settings and parameters

To ensure comparable confinements and cooling times for variable crystal lengths, the relation (2.13) is used for parameter settings in calculations throughout this chapter, unless mentioned otherwise. The radial secular frequency is set to $\omega_{\mathrm{rad}} = 2\pi\,1\,\mathrm{MHz}$ (for Yb^+ ions) and the axial frequency is calculated to fulfil (2.13) and be exactly on the phase transition. In reality the phase transition happens at even weaker confinements and therefore this scheme can be used safely. E.g. for $N = 13$ ions the phase transition occurs at $\alpha = \frac{\omega_{\mathrm{rad}}}{\omega_{\mathrm{ax}}} = \frac{1000}{150.8} \approx 6.7$ according to (2.13), while in reality the crystal only starts forming a 2D configuration at a trap confinement of $\alpha = \frac{\omega_{\mathrm{rad}}}{\omega_{\mathrm{ax}}} \approx \frac{1000}{190} \approx 5.3$.
In general for a mixed-species ion crystal, the phase transition not only depends on the number of ions in the crystal but also on the ratio of the number of clock ions and cooling ions and their configuration. Therefore the method described in the previous paragraph does not perfectly ensure equal confinement over all the configurations and compositions. However, as the described dependence on the configuration and clock/cooling ion ratio is small compared to the dependence on the total number of ions in the crystal only the latter one is taken into account for simplicity throughout this thesis.
Two other parameters that also generally influence the absolute mode cooling times τ_α and the equilibriums temperatures T_α are the saturation parameter s [28, 29], that shows up in the scattering rate Γ_{sc} and the angle between the laser and all spatial dimensions. The latter one is chosen to be 54.7°, which is equivalent to equal cooling in all directions. The choice of the saturation parameter comes with a trade off between minimal cooling times and minimal equilibrium temperatures. This is depicted in figure 4.1 for a single Yb^+ ion. The trade off can be solved by weighting both quantities. However, the decision on the

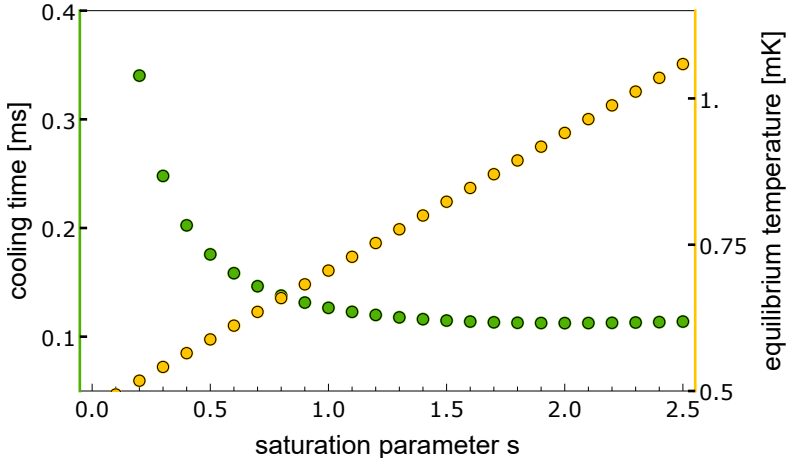

Figure 4.1: Dependence of the mode cooling time (green, left axis) and the equilibrium temperature (yellow, right axis) for a single Yb^+ ion on the saturation parameter s.

particular weights depends on the application of the Coulomb crystals. For simplicity the saturation parameter is chosen to be $s = 1$ for all calculations.
The ions' mean velocities, that was derived in the last subsection, can also be used to calculate motion related systematic energy shifts like the time dilation shift or the intrinsic micromotion AC-Stark shift. Their relevance for the main results of this chapter is investigated in the next subsection.

4.1.3 Relevance of motional shifts

With the goal of operating a two-species multi-ion clock with In^+ as a clock ion and Yb^+ as a cooling ion, one wants to minimize motional energy shifts in In^+. This subsection demonstrates that the choice of a configuration only slightly affects these motional shifts. Also the dependence on the trap confinement is analysed. This is accomplished by firstly comparing the individual time dilation shifts of In^+ ions in all possible crystal configurations of a certain composition, which are given by

$$\left\langle \frac{\Delta\nu_{\mathrm{td}}}{\nu_0} \right\rangle_i = -\frac{\langle v_i^2 \rangle}{2c^2} \,. \tag{4.6}$$

Here ν_0 is the clock transition frequency, $\langle v_i^2 \rangle$ the respective mean squared velocity of ion i and c is the speed of light. The addressed shifts are presented in figure 4.2 for a chosen

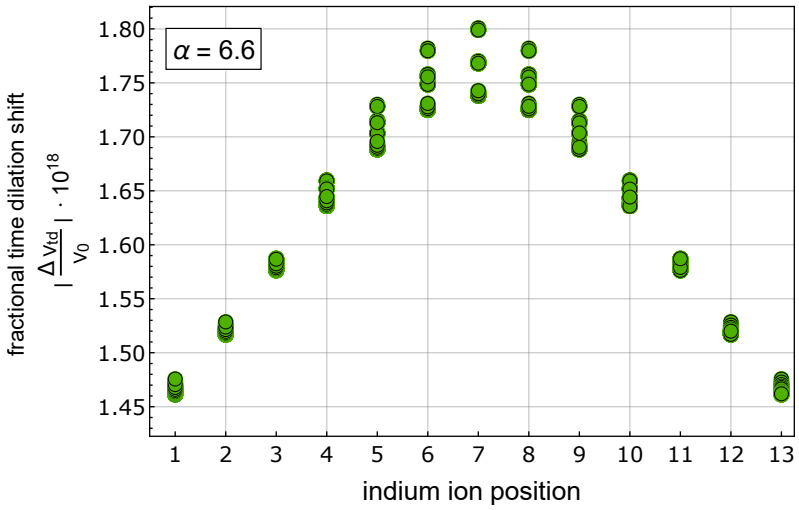

Figure 4.2: Absolute time dilation shifts $|\Delta\nu_{\mathrm{td}}/\nu_0|$ of In^+ ions in all 286 configurations of a $(n_{Yb^+}, n_{In^+}) = (3, 10)$-composition. The shifts of the 3 Yb^+ ions are not shown. secular frequencies: $\omega_{\mathrm{rad}} = 2\pi\, 1000\,\mathrm{kHz}$, $\omega_{\mathrm{ax}} = 2\pi\, 150\,\mathrm{kHz}$ $(\alpha \approx 6.7)$

composition $(n_{Yb^+}, n_{In^+}) = (3, 10)$, which makes a total of $\binom{n_{Yb^+}+n_{In^+}}{n_{Yb^+}} = \binom{13}{3} = 286$ configurations. Shifts for Yb^+ are not included, because they are not important for clock operation. According to figure 4.2, the configuration does not influence the time dilation shift significantly. From the outer indium ion position to the centre of the crystal the total spread of the fractional time dilation shift $|\Delta\nu_{\mathrm{td}}/\nu_0|$ increases from $\sim 0.02 \cdot 10^{-18}$ to $\sim 0.063 \cdot 10^{-18}$. The plot looks similar for the intrinsic micromotion AC-Stark shift as

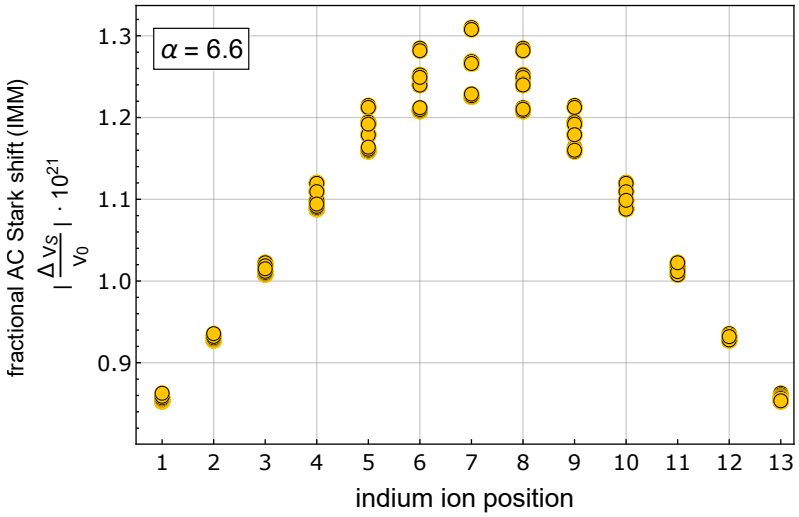

Figure 4.3: Absolute intrinsic micromotion AC-Stark shifts $|\Delta\nu_S/\nu_0|$ of In^+ ions in all 286 configurations of a $(n_{Yb^+}, n_{In^+}) = (3, 10)$-composition. The shifts of the 3 Yb^+ ions are not shown. secular frequencies: $\omega_{rad} = 2\pi\,1000\,\text{kHz}$, $\omega_{ax} = 2\pi\,150\,\text{kHz}$ ($\alpha \approx 6.7$)

seen in figure 4.3, which is given by

$$\left\langle \frac{\Delta\nu_S}{\nu_0} \right\rangle_i = -\frac{\Delta\alpha_{stat}}{h\nu_0} \frac{\langle E^2_{rf,i}\rangle}{2}\,. \tag{4.7}$$

Here, $\Delta\alpha_{stat}$ is the static differential polarizability of the clock states and $E_{rf,i}$ the radio frequency electric field acting on ion i. For this shift the total spread increases from the outer indium ion position to the centre of the crystal from $\sim 0.01 \cdot 10^{-21}$ to $\sim 0.04 \cdot 10^{-21}$.

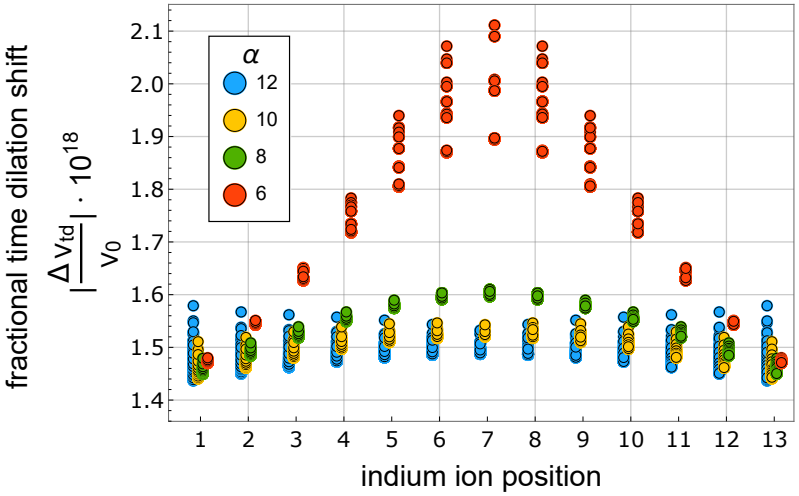

Figure 4.4: Absolute time dilation shifts $|\Delta\nu_{td}/\nu_0|$ of In^+ ions for all 286 possible configurations in a $(n_{Yb^+}, n_{In^+}) = (3, 10)$-composition for different values of the secular trap frequency ratio α. The respective shifts are horizontally shifted from their position number for for easier recognition. Yb^+ shifts ions are not included.

The shifts also depend on the trap frequency ratio α. Figure 4.4 displays the In^+ ions'

time dilation shifts for different values of the α in all possible configurations of the $(n_{\mathrm{Yb}^+}, n_{\mathrm{In}^+}) = (3, 10)$-composition. With the confinement approaching the phase transition to a 2D crystal at $\alpha \approx 5.3$ the time dilation shifts for all configurations rise in the centre of the crystal due to higher radial motional amplitudes from increased Coulomb repulsion in the more densely packed chain. While the mean shift for the central indium ion (position 7) for $\alpha = 12, 10, 8$ is relatively stable and is equal to $(1.492, 1.523, 1.601) \cdot 10^{-18}$ the mean value rises to $1.943 \cdot 10^{-18}$ for $\alpha = 6$. Intrinsic micromotion AC-Stark shifts behave similarly.
Although the choice of the configuration of a Coulomb crystal and its confinement in the ion trap affect the motional shifts, the respective changes are negligible in comparison to the effect of these parameters on the cooling times, which change by orders of magnitude as detailed below. Therefore it makes more sense to focus on cooling times when choosing a crystal configurations and confinement. The next subsection reviews the geometric properties of Coulomb crystal that determine cooling times and presents results of the cooling times calculations.

4.1.4 Geometric properties of Coulomb crystals

Before investigating how different properties in an ion trap effect cooling times of ion crystals, this subsection explains the behaviour of cooling times and relates them to geometric properties of motional modes. As described in section 2.2, multi-ion crystals are usually cooled sympathetically. Motional mode cooling times and rates depend on the participation of the cooling ions in the mode's oscillatory motion. This is evident in the case of a 2-ion crystal with a single Yb^+ ion and a single In^+ ion and comparing it with a 2 Yb^+ crystal in figure 4.5. To compare the mode frequencies with the ones for the example composition with 13 ions, the same confinement as for 13 ions is chosen. Additionally, the

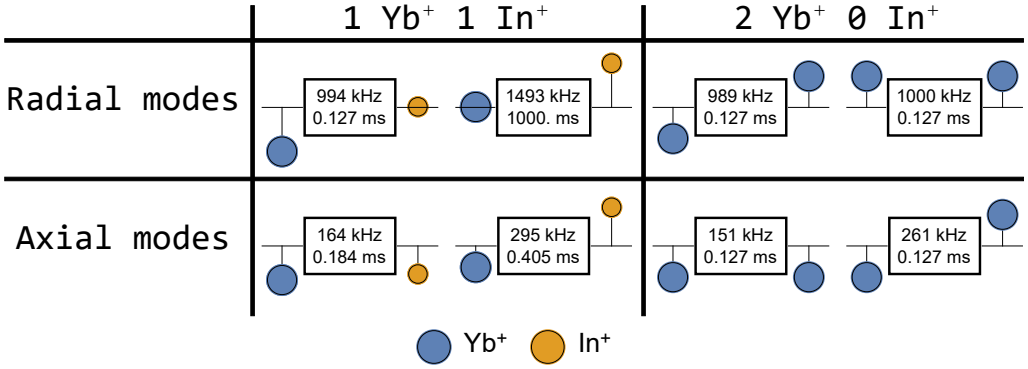

Figure 4.5: Radial and axial motional modes of 2-ion Coulomb crystals consisting of one Yb^+ and one In^+ ion with their eigenfreq. $\omega_\alpha/2\pi$ and 1/e cooling times τ_α for $\omega_{\mathrm{rad}} = 2\pi\,1000\,\mathrm{kHz}$, $\omega_{\mathrm{ax}} = 2\pi\,150\,\mathrm{kHz}$ $(\alpha \approx 6.7)$

mixed crystal has one less cooling ion, which roughly halves the cooling efficiency. The modes show asymmetric motional amplitudes due to the ions' mass difference. The motional modes divide into one mode where mostly Yb^+ oscillates (Yb^+-like mode) and one mode where mostly In^+ oscillates (In^+-like mode). This distinction is more pronounced in the radial direction. The modes with less amplitude of the cooling ion Yb^+ have increased cooling times, as Yb^+ laser cooling takes less kinetic energy out of the mode. In the

extreme case of no cooling ion oscillation, the laser would not be able to cool this mode at all. Quantitatively this is also described by equation (4.4c), where the sum $\sum_i \frac{\beta'^2_{\alpha,i}}{m_i}$ of the cooling ions' squared normalized mode amplitudes $\beta'_{\alpha,i}$ is proportional to the cooling rate $\dot{E}^{\alpha}_{\text{cool,const}}$.

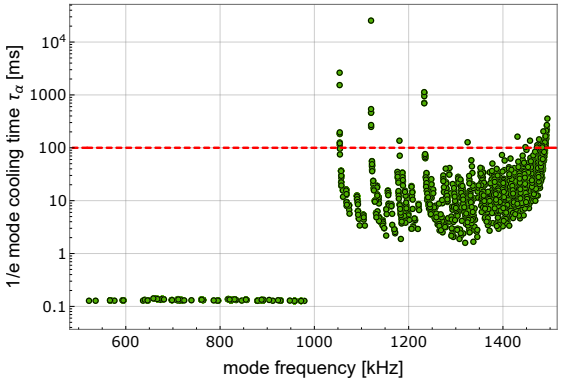

Figure 4.6: Radial mode cooling times τ_α on a logarithmic scale vs. their frequencies for $\omega_{\text{rad}} = 2\pi\,1000\,\text{kHz}$, $\omega_{\text{ax}} = 2\pi\,150\,\text{kHz}$ ($\alpha \approx 6.7$) for all 286 configurations of a $(n_{\text{Yb}^+}, n_{\text{In}^+}) = (3, 10)$ composition. A horizontal line at $\tau_\alpha = 100\,\text{ms}$ is shown for orientation.

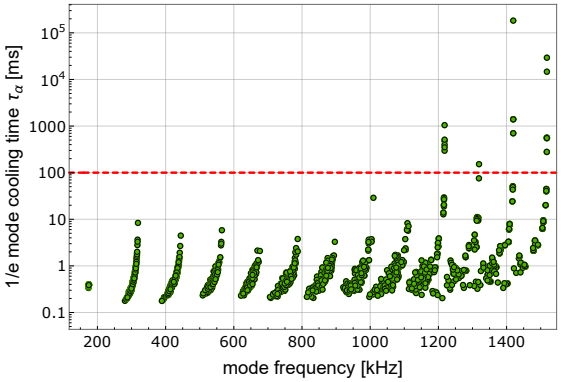

Figure 4.7: Axial mode cooling times τ_α on a logarithmic scale vs. their mode frequencies for $\omega_{\text{rad}} = 2\pi\,1000\,\text{kHz}$, $\omega_{\text{ax}} = 2\pi\,150\,\text{kHz}$ ($\alpha \approx 6.7$) for all 286 configurations of a $(n_{\text{Yb}^+}, n_{\text{In}^+}) = (3, 10)$ composition. A horizontal line at $\tau_\alpha = 100\,\text{ms}$ is shown for orientation.

Another interesting observation is in the frequencies of these individual modes. The radial Yb^+ and In^+-like modes oscillate with a similar frequency with respect to the single ion mode frequencies, which are 1000 kHz for Yb^+ and 1470 kHz for In^+. In figure 4.6, the radial modes of a more complicated example composition with 3 Yb^+ and 10 In^+ show the same structure and split up into two bulks. The low frequency bulk ($< 1\,\text{MHz}$) corresponds to Yb^+-like modes which are cooled efficiently and have frequencies similar to the Yb^+ eigenfrequency while the high frequency bulk ($> 1\,\text{MHz}$) is not cooled as efficiently because mostly the In^+ ions participate in the oscillation. Figure 4.7 shows similarities to the typical spectral behaviour for axial modes. The common mode (lowest frequency) has similar cooling times for all configurations. Cooling times for higher order modes depend on the configuration. The variance of cooling times increases for the highest order modes. This behaviour can be explained by the number of nodes, that increase with the frequency, in the motional modes. Similarly, the probability that cooling ions sit on one of the existing nodes increases, which scales the cooling times.
The next subsection presents the results of a calculation for an example configuration.

4.1.5 Example calculation, general observations and presentation methodology

As the number of ions in a Coulomb crystal increases, the number of possible configuration rises drastically. The results will be presented similarly to figure 4.8 and figure 4.9 throughout this chapter to maintain a clean presentation. For a specific composition, each plot contains data points for all possible configurations. Since the cooling times remain the same when a configuration is mirrored, only one of the corresponding configurations is included in the graph. This roughly halves the total number of configurations. For

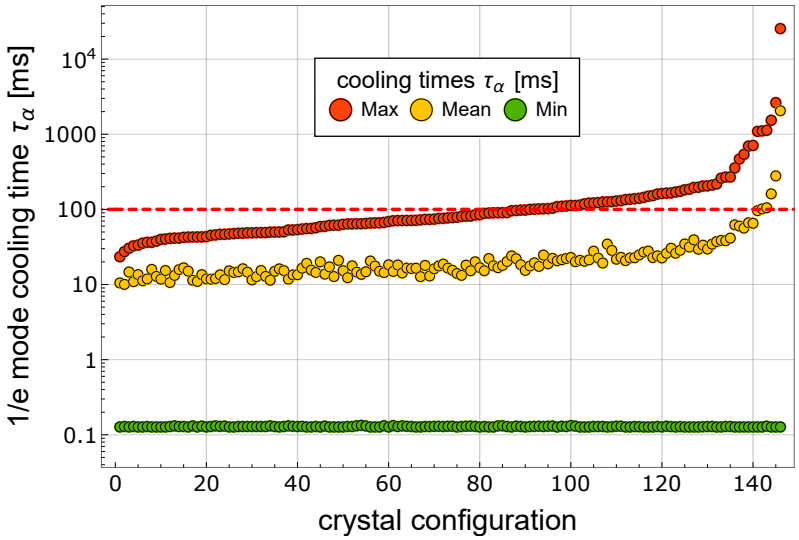

Figure 4.8: Sorted maximal, mean and minimal **radial** mode cooling times τ_α for $\omega_{\text{rad}} = 2\pi\,1000\,\text{kHz}$, $\omega_{\text{ax}} = 2\pi\,150\,\text{kHz}\,(\alpha \approx 6.7)$ for all 146 unique possible configurations with 3 Yb^+ an 10 In^+ ions. A horizontal line at $\tau_\alpha = 100\,\text{ms}$ is shown for orientation. The cooling time axis is scaled logarithmically.

the example composition with $(n_{Yb^+}, n_{In^+}) = (3, 10)$, the total number of 286 is reduced to 146 individual configurations. These are sorted by their worst cooled mode (maximal cooling time), as this sets a lower limit for the required total cooling time before each clock interrogation. The configurations are placed on the abscissa axis in this order. For each configuration the maximal, the mean and the minimal mode cooling times are presented. For this example the calculated maximal 1/e cooling times increase from 23 ms radially

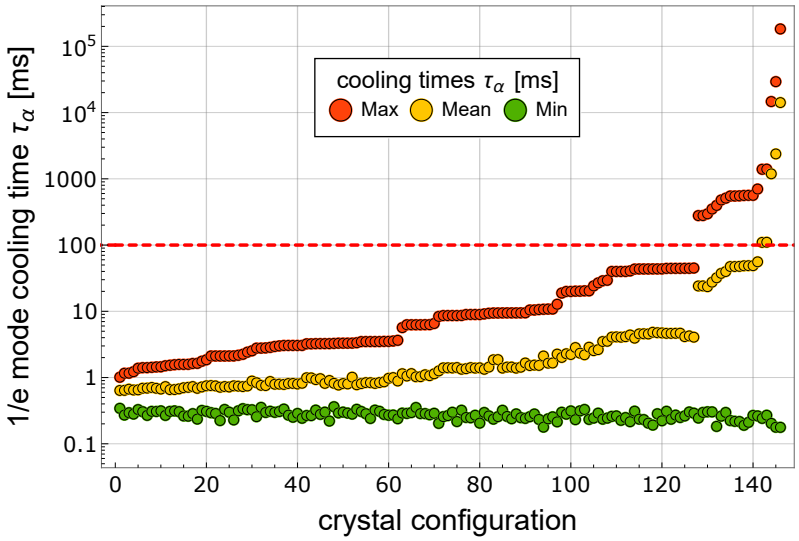

Figure 4.9: Sorted maximal, mean and minimal **axial** mode cooling times τ_α for $\omega_{\text{rad}} = 2\pi\,1000\,\text{kHz}$, $\omega_{\text{ax}} = 2\pi\,150\,\text{kHz}\,(\alpha \approx 6.7)$ for all 146 unique possible configurations with 3 Yb^+ an 10 In^+ ions. A horizontal line at $\tau_\alpha = 100\,\text{ms}$ is shown for orientation. The cooling time axis is scaled logarithmically.

(1 ms axially) in the best configuration to over 10 000 ms in the worst configuration in both dimensions. As this ranges over several orders of magnitude the cooling time axis is scaled logarithmically. A dashed red horizontal line at $\tau_\alpha = 100\,\text{ms}$ is included for orientation.

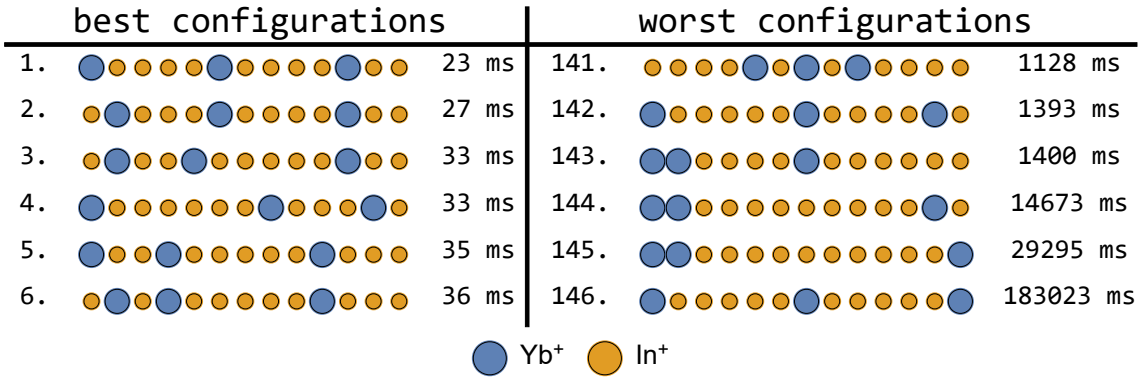

Figure 4.10: Best and worst configurations for 3 Yb^+ and 10 In^+ ions sorted after their maximal mode cooling time for radial and axial modes. $\omega_{\text{rad}} = 2\pi\,1000\,\text{kHz}$, $\omega_{\text{ax}} = 2\pi\,150\,\text{kHz}$ ($\alpha \approx 6.7$). For comparison: the 1/e cooling time for a 13 Yb^+ ion chain for all modes is 0.13 ms.

Figure 4.10 shows the best 6 and the worst 6 configuration considering axial and radial modes. Although some broad relations between the arrangement of the ions and the cooling efficiency can be drawn from these rankings, there seems to be no trivial recipe how to set up cooling and clock ions to have the most efficient cooling. In general, symmetry within the crystal should be avoided. In a single species coulomb crystal, all modes are either axially or point symmetrical. While this is not strictly true for mixed-species crystals, the mode structure is similar. For few symmetrically distributed cooling ions, the chance that all the ions are on or close to nodal points is increased. This especially applies for configurations with odd ion numbers.
From the observations from figure 4.5 one can derive, that the worst cooled mode of the last-placed configuration in figure 4.10 features relatively little motion of the cooling ions. Contrary to that, the worst cooled mode of the first-placed configuration should show relatively strong motion of the cooling ions. Figure 4.11 and figure 4.12 support this prediction. They show the worst cooled motional modes of the first placed configuration and the last placed configuration in the ranking of figure 4.10 (the configurations are sorted by their worst cooled modes). In figure 4.11, the cooling ions' motional amplitude is relatively low in comparison to the amplitude of the clock ions, but the cooling ion amplitude in figure 4.12 is not distinguishable from zero at the chosen resolution.

In figure 4.13 the best 6 and worst 6 configurations of the $(n_{\text{Yb}^+}, n_{\text{In}^+}) = (5, 5)$ composition are shown. By analysing this compilation where the number of cooling ions increases and its less likely that all cooling ions are on or close to nodal points, one can also conclude that the cooling ions should be equally distributed over the whole length of the crystal and not bulk up in one area.
The cooling times of Coulomb crystals depend strongly on the chosen confinement and composition of the crystal. The influence of these parameters on the cooling times, which were presented as an example based on the $(n_{\text{Yb}^+}, n_{\text{In}^+}) = (3, 10)$ and the $(5, 5)$ composition in this section, will be systematically analysed in the next section.

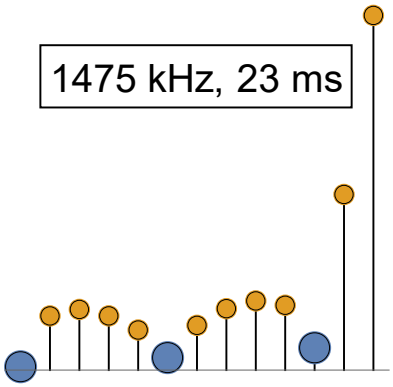

Figure 4.11: Worst cooled motional mode of the first placed configuration in the ranking presented in figure 4.10. Big orange circles correspond to the Yb^+ cooling ions and the small blue ones represent In^+ as clock ions. The presented mode is the radial common mode. The image is labelled with the modes frequency and its 1/e cooling time. $\omega_{\mathrm{rad}} = 2\pi\,1000\,\mathrm{kHz},\ \omega_{\mathrm{ax}} = 2\pi\,150\,\mathrm{kHz}\,(\alpha \approx 6.7)$

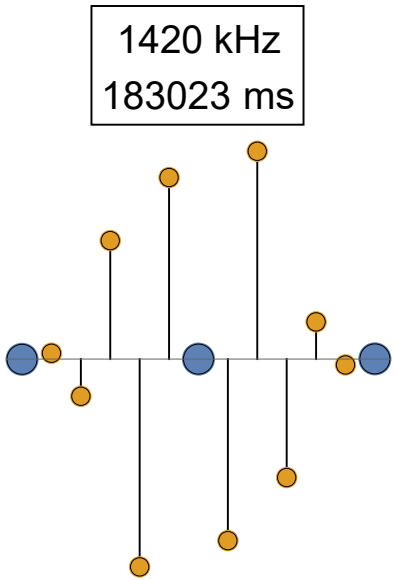

Figure 4.12: Worst cooled motional mode of the last placed configuration in the ranking presented in figure 4.10. Big orange circles correspond to the Yb^+ cooling ions and the small blue ones represent In^+ as clock ions. The presented mode is on of the axial modes. The image is labelled with the modes frequency and its 1/e cooling time. $\omega_{\mathrm{rad}} = 2\pi\,1000\,\mathrm{kHz},\ \omega_{\mathrm{ax}} = 2\pi\,150\,\mathrm{kHz}\,(\alpha \approx 6.7)$

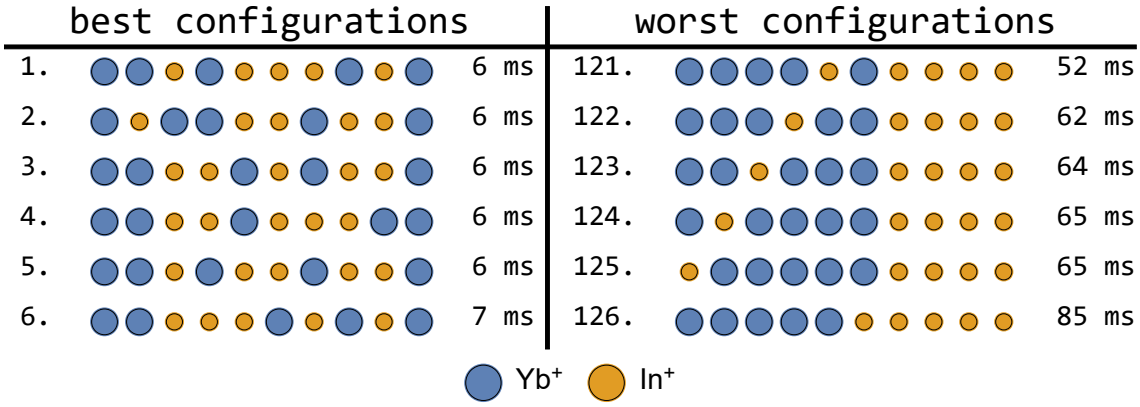

Figure 4.13: Best and worst configurations for 5 Yb^+ and 5 In^+ ion sorted after their maximal mode cooling time for radial and axial modes. $\omega_{\mathrm{rad}} = 2\pi\,1000\,\mathrm{kHz},\ \omega_{\mathrm{ax}} = 2\pi\,189\,\mathrm{kHz}\,(\alpha \approx 5.3)$.

4.2 Systematic analyses of parameters affecting cooling times

The last section explained how 1/e motional mode cooling times of mixed-species Coulomb crystals are calculated in this thesis and demonstrated first results on the basis of example compositions. The section also determined parameters that strongly influence the results of

these calculations, which are the chosen confinement and the composition of the Coulomb crystal. The latter parameter is split up into the ratio between the cooling ions and the clock ions $n_{\text{cool}}/n_{\text{clock}}$ and the total number of ions in the crystal $n_{\text{ions}} = n_{\text{cool}} + n_{\text{clock}}$. The following three subsections will analyse the dependence of cooling times on these parameters.
In some of the subsections the number of possible configurations within a composition changes with the chosen parameter. For this reason all sets of configuration for a given set of parameters are normalized to the window frame of the plot. Specifically, the first configuration within a ranking is always placed at the very left edge of the window frame and the last one at the very right edge regardless of the total number of configurations. For clarity, only the maximal cooling time of a configuration is shown in the plots below.

4.2.1 Ratio between cooling ions and clock ions

This subsection investigates the influence of the ratio between the number of cooling ions and the number of clock ions $n_{\text{cool}}/n_{\text{clock}}$ in the Coulomb crystal on their motional mode cooling times. The total number of ions $n_{\text{ions}} = 10$ in the crystal and the crystal confinement $\alpha \approx 5.3$ are held constant. The confinement is set to be close to the phase transition. Figure 4.14 presents the maximal motional mode cooling times (radial and

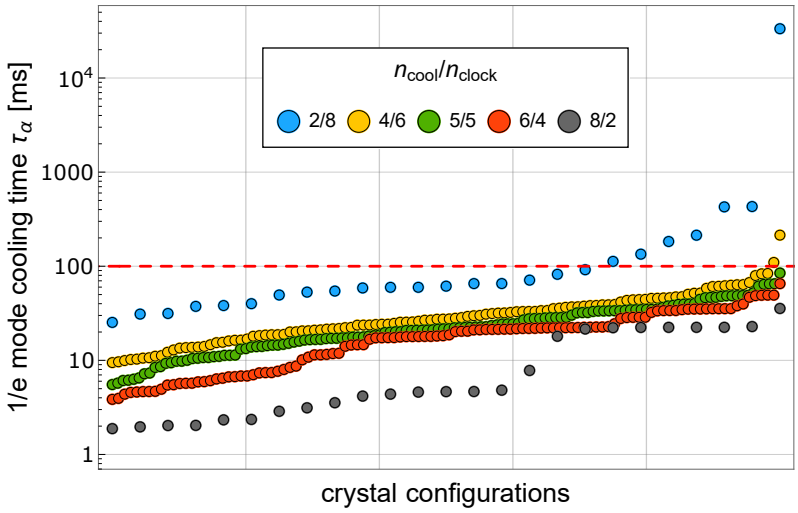

Figure 4.14: Maximal 1/e cooling times of radial and axial modes for all possible configurations for different compositions. The total number of ions $\boldsymbol{n_{\text{ions}} = 10}$ is kept constant while the ratios between the number of cooling ions and clock ions $\boldsymbol{n_{\text{cool}}/n_{\text{clock}}}$ is varied. The secular trap frequency ratio $\boldsymbol{\alpha \approx 5.3}$ also remains constant. A horizontal line at $\boldsymbol{\tau_\alpha = 100\,\text{ms}}$ is shown for orientation. The cooling time axis is scaled logarithmically.

axial modes) of all configuration out of compositions with four different ratios $n_{\text{cool}}/n_{\text{clock}}$. This is 1/4, 2/3, 3/2 and 4 meaning 2 Yb^+ and 8 In^+ ions, 4 Yb^+ and 6 In^+ ions, 6 Yb^+ and 4 In^+ ions and lastly 8 Yb^+ and 2 In^+ ions. As $\binom{10}{2} = 45 < \binom{10}{4} = 210$ the first and the last composition consist of fewer configurations than the second and the third composition. As expected, the maximal 1/e cooling times decrease monotonically with an increase of the amount of cooling ions in the crystal.

4.2.2 Total number of ions

This subsection presents data on the dependence of motional mode cooling times on the total number of ions $n_{\text{ions}} = n_{\text{cool}} + n_{\text{clock}}$ in the crystal. For this calculation, the ratio of $n_{\text{cool}}/n_{\text{clock}} = 1$ is kept constant. The parameter α is individually adapted to the respective value of n_{ions} to ensure comparable confinements (see subsection 4.1.2). Figure 4.15 shows

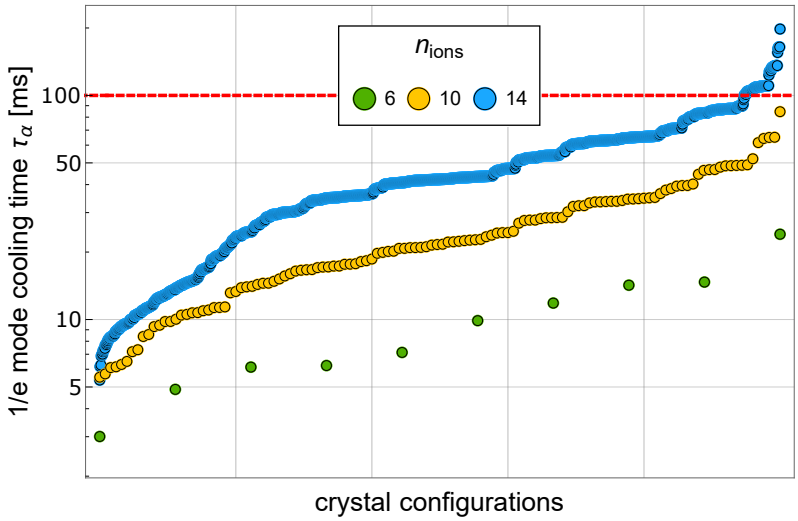

Figure 4.15: Maximal 1/e cooling times of radial and axial modes for all possible configurations for different compositions. The total number of ions n_{ions} is varied, while the ratio between the number of cooling ions and clock ions is held constant with $\boldsymbol{n_{\text{cool}} = n_{\text{clock}}}$. The respective secular trap frequency ratio α is adapted to n_{ions} to match (2.13) (see subsection 4.1.2). A horizontal line at $\tau_\alpha = 100\,\text{ms}$ is shown for orientation. The cooling time axis is scaled logarithmically.

the maximal motional mode cooling times (radial and axial modes) of all configuration out of compositions with three different values of $n_{\text{ions}} = 6, 10$ and 14. The amount of configurations within each composition varies a lot: $\binom{6}{3} = 20 < \binom{10}{5} = 252 < \binom{14}{7} = 3432$. As the ion number increases, the cooling times of the best-cooled modes remain similar of ~ 3 to 6 ms. However, the cooling times of the worst-cooled modes become longer as the ion number increases with 24.0 ms for $n_{\text{ions}} = 6$, 84.6 ms for $n_{\text{ions}} = 10$ and 197.8 ms for $n_{\text{ions}} = 14$, which also results in an increase in the average cooling times.

4.2.3 Crystal confinement

This subsection investigates the influence of the ratio of the radial and the axial secular frequency, $\alpha = \omega_{\text{rad}}/\omega_{\text{ax}}$, on motional mode cooling times. The previously varied parameters are constant in this calculations. The same example configuration of $(n_{\text{cool}}, n_{\text{clock}}) = (3, 10)$ as in subsection 4.1.5 is chosen. Figure 4.16 shows the maximal motional mode cooling times (radial and axial modes) of all configurations out of compositions with four different values of $\alpha = 12, 10, 8$ and 6. The confinement strongly decreases all maximal cooling times globally over about two orders of magnitude from $\alpha = 12$ to $\alpha = 6$, where the confinement is close to the phase transition at $\alpha \approx 5.3$. The changes are due to the mass dependence of the radial potential and thus to the radial modes. With weaker radial confinement, the fraction of heavier cooling ions in the amplitudes of the mode oscillations

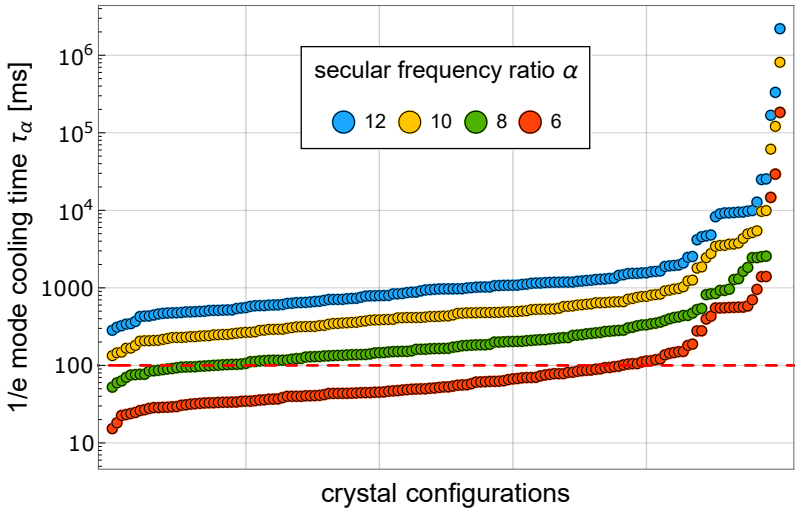

Figure 4.16: Maximal 1/e cooling times of radial and axial modes of all configurations of the $(n_{\mathrm{cool}}, n_{\mathrm{clock}}) = (3, 10)$-composition for different ratios of secular frequencies α. A horizontal line at $\tau_\alpha = 100\,\mathrm{ms}$ is shown for orientation. The cooling time axis is scaled logarithmically.

increases and the corresponding modes can be cooled more efficiently.
All three investigated parameters have a clear influence on the motional mode cooling times of mixed-species Coulomb crystals. Without considering other potentially relevant properties of these crystals, it is most optimal to set up the composition with as many cooling ions and as few total ions n_{ions} as possible. Also the trap should be operated with a confinement α close to the phase transition. A discussion of limitations of these recommendations can be found at the end of this chapter.

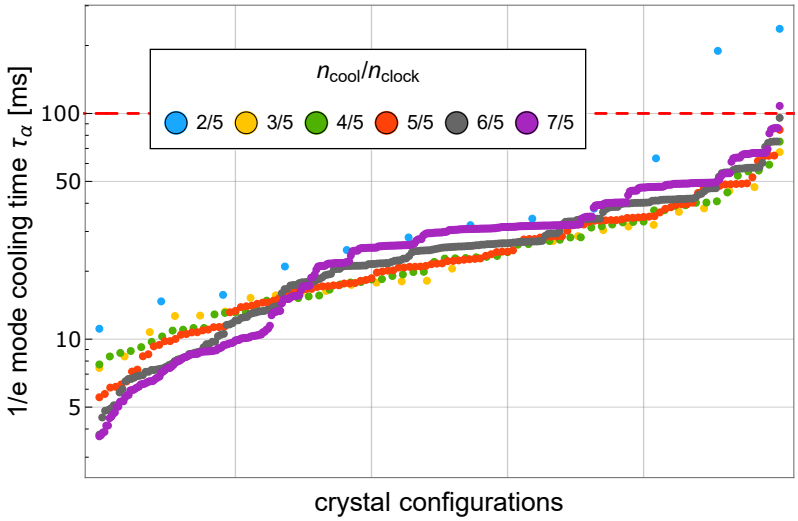

Figure 4.17: Maximal 1/e cooling times of radial and axial modes of all configurations of composition with a constant number of 5 clock ions ($n_{\mathrm{clock}} = const.$) and different numbers of cooling ions. A horizontal line at $\tau_\alpha = 100\,\mathrm{ms}$ is shown for orientation. The cooling time axis is scaled logarithmically.

Another interesting observation can be drawn from figure 4.17. Here the number of clock

ions is kept constant while the number of cooling ions is increased from 2 to 7. For this series of compositions, two out of three of the previously analysed parameters are tuned simultaneously (n_{ions} and $n_{\text{cool}}/n_{\text{clock}}$). The figure shows that the effect of the varied total number of ions in the crystal more or less cancels with the effect of the varied ratio of cooling ions in the crystal for the respective maximal cooling times. The maximal cooling times behave similarly for the configurations within all different compositions. Only the worst cooled modes of the $(n_{\text{cool}}, n_{\text{clock}}) = (2, 5)$ are an exception to this rule. However, this is not the case for the mean cooling times of the same compositions, which are presented in the appendix in figure 8.3. The mean cooling times decrease monotonically as the number of cooling ions increases.

4.3 Time dilation shifts for finite cooling times

In the previous subsections infinite cooling times were assumed in order to reach the modes equilibrium temperatures T_α and calculate the time dilation shifts $\Delta\nu_{\text{td}}/\nu_0$ of individual ions. For efficiently coolable configurations, this assumption seems valid, but for modes with 1/e cooling times exceeding typical cooling times, this may not hold. During a clock cycle, ions can heat up (e.g. due to background collisions) and need to be recooled afterwards. In figure 4.18, the effects of $0, 1, 10, 100$ and 1000 ms of finite Doppler cooling

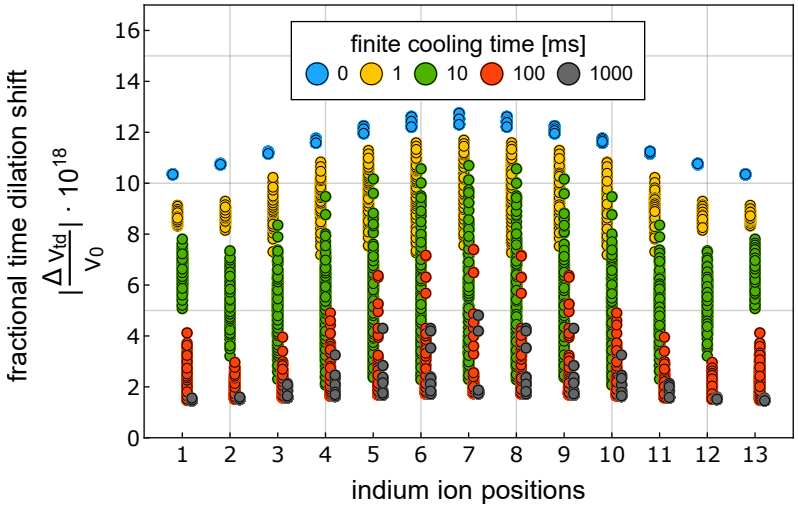

Figure 4.18: Absolute fractional time dilation shifts for all In^+ ions for all 286 configurations with 3 Yb^+ and 10 In^+ ions for different finite cooling times starting from 5 mK. Here the model from (4.3) is used. confinement: $\alpha \approx 6.7$

starting from an arbitrary common mode temperature of 5 mK time on the individual time dilation shifts are analysed. Here the time-dependent temperature model from (4.3) is used to evaluate the shifts for all In^+ ions for all 286 configurations with 3 Yb^+ and 10 In^+. As all modes start being cooled from the same temperature, the total spread in the time dilation shifts is minimal for 0 ms of cooling at a level of ~ 1.0 to $1.2 \cdot 10^{-17}$. Then with 1 ms and 10 ms of cooling the shifts start decreasing, while the total spread drastically increases ranging from ~ 5 to $8 \cdot 10^{-18}$ for the outermost ion to ~ 2 to $11 \cdot 10^{-18}$ in the chains center because of the various cooling efficiencies for different configurations. The shifts approach the minimal limit of $\sim 1.0 \cdot 10^{-18}$ for cooling times of 100 and 1000 ms.

While for 1000 ms of cooling, the total spread is already below $0.2 \cdot 10^{-18}$ at the outer parts of the ion crystal, it is still at $4 \cdot 10^{-18}$ in the center. As the shifts for these different cooling times vary strongly, they need to be carefully calculated and predicted for multi-ion clock operation.

4.4 Cooling times in 2D and 3D crystals

So far, only cooling of one dimensional configurations has been considered, as the *Mathematica*-code that has been used in the previous sections only solves the one dimensional equations of motion for mixed-species ion Coulomb crystals. Another reason for working in one dimension is the increased control over these crystals and the ability to easily detect their configuration. In order to pick and switch between specific configuration based on different cooling properties, these configurations need to be detected. This has practical limits like the camera's depth of focus or the presence of cooling lasers for both ion species, which varies for every experimental setup.
On the other hand, investigating in two- and three dimensional cooling opens up a bigger parameter space and could provide a solution for cooling issues with complicated Coulomb crystals with many clock ions. As it is shown in subsection 4.2.3 in 1D, less confinement results in increased contribution of the heavier cooling ions in the modes oscillation and leads to reduced cooling times. This behaviour could continue after crossing the phase transition to two- and three dimensional configurations.
The following calculations are executed with a *Matlab* code [30]. It starts by adding random 3D-offsets to a linear configuration of clock and cooling ions and then minimizing the total potential energy to find the equilibrium positions at given trap parameters. The secular frequencies $\omega_{\mathrm{rad},1}$, $\omega_{\mathrm{rad},2}$, and ω_{ax} in all three trap directions can be set individually. To compare Matlab to Mathematica the the radial plane is kept degenerate throughout this section by setting

$$\omega_{\mathrm{rad},1} = \omega_{\mathrm{rad},2} \qquad \text{and redefining the confinement} \quad \alpha = \frac{\omega_{\mathrm{rad},1}}{\omega_{\mathrm{ax}}} = \frac{\omega_{\mathrm{rad},2}}{\omega_{\mathrm{ax}}}. \tag{4.8}$$

Afterwards, the code solves for the 3D eigenmodes of the second derivative of the ions' potential, the Hessian matrix. Motional mode cooling rates are determined with an alternative approach. Laser cooling is simulated by adding a small negative friction term γ_a to the equations of motion for the cooling ions, which leads to a quadratic eigenvalue problem and results consisting of complex eigenvalues. The imaginary part corresponds to the modes' frequency ω_n and the real part κ_n can be understood as a response to the additional friction term or how well the laser cooling addresses motional mode, which is equivalent to a cooling rate. The cooling rates for each solution add up to

$$\sum_n \kappa_n = 3\gamma_a N_{\text{cooling ions}}. \tag{4.9}$$

In figure 4.19, the calculated complex eigenvalues $i\omega_n - \kappa_n$ are plotted and compared to the cooling rates over their mode frequencies computed with the *Mathematica* code. The codes produce the same results if one applies the same normalization to the *Mathematica* cooling rates as in *Matlab* (4.9).
As it is shown in figure 4.20 also the 1/e cooling times calculated as in (4.5) by both codes

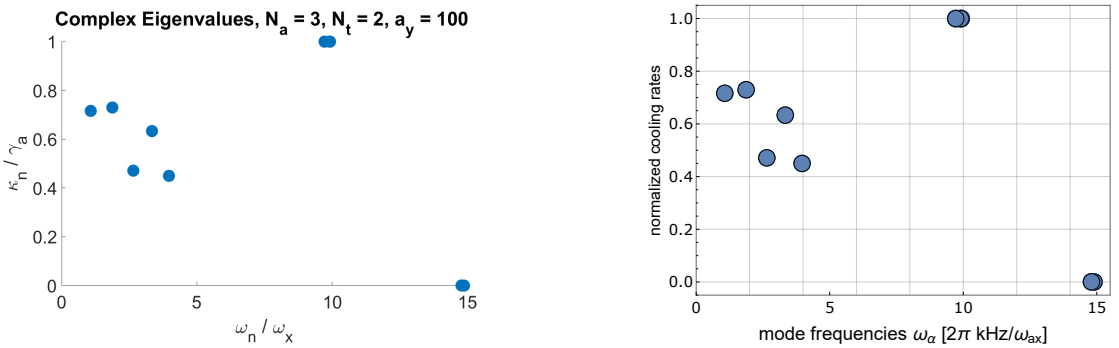

(a) *Matlab* (b) *Mathematica*

Figure 4.19: (*a*) complex mode eigenvalues calculated by Matlab κ_n vs. ω_n normalized by the friction coefficient γ_a and the axial secular frequency ω_x , (*b*) Mathematica cooling rates vs. mode frequencies normalized the same way as in (*a*).
Config: In^+-Yb^+-Yb^+-In^+-Yb^+ **confinement:** $\alpha = 10$

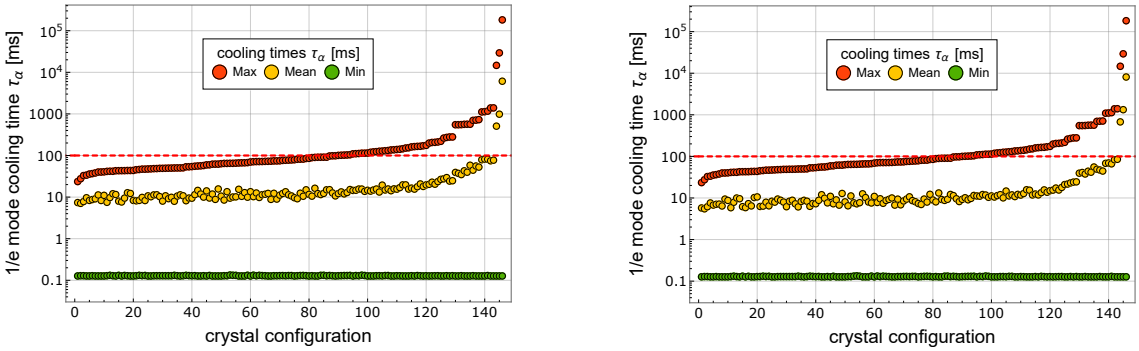

(a) ***Matlab*** (b) ***Mathematica***

Figure 4.20: Sorted maximal 1/e cooling times of motional modes for all configurations with 3 Yb^+ and 10 In^+ ions calculated with (*a*) *Matlab* and (*b*) *Mathematica*. A horizontal line at $\tau_\alpha = 100\,\text{ms}$ is shown for orientation. The cooling time axis is scaled logarithmically.
confinement: $\alpha \approx 6.7$

agree within 10^{-3}, with the discrepancy being due to numerical deviations. The following paragraphs will give an overview on cooling properties of 2D and 3D crystals using *Matlab*. A more detailed analysis would go beyond the scope of this master thesis. Figure 4.21 shows the effect of different confinement conditions on the maximal and the mean 1/e cooling times for example composition $(n_{\text{cool}}, n_{\text{clock}}) = (3, 10)$. Both radial secular frequencies $\omega_{\text{rad},1} = \omega_{\text{rad},2} =: \omega_{\text{rad}}$ are consecutively decreased from $\frac{\omega_{\text{rad}}}{2\pi} = 600\,\text{kHz}$ to 100 kHz, which corresponds to the used axial secular frequencies. This means $\alpha = \omega_{\text{rad}}/\omega_{\text{ax}}$ decreases from 6 to 1 in integer steps. The equilibrium positions for the chosen composition are one dimensional for $\alpha = 6$, two dimensional for $\alpha = 5$ and 4 and three dimensional $\alpha = 3, 2$ and 1. Figure 4.22 visualizes these conditions for an example configuration 5 In^+ - 3 Yb^+ - 5 In^+.

The consecutive decrease of the secular frequency ω_{rad} in both radial trap dimensions leads to structural changes of the variation of mean and especially the maximal cooling rates over the various possible configurations in the 2D and 3D regime. This behaviour is

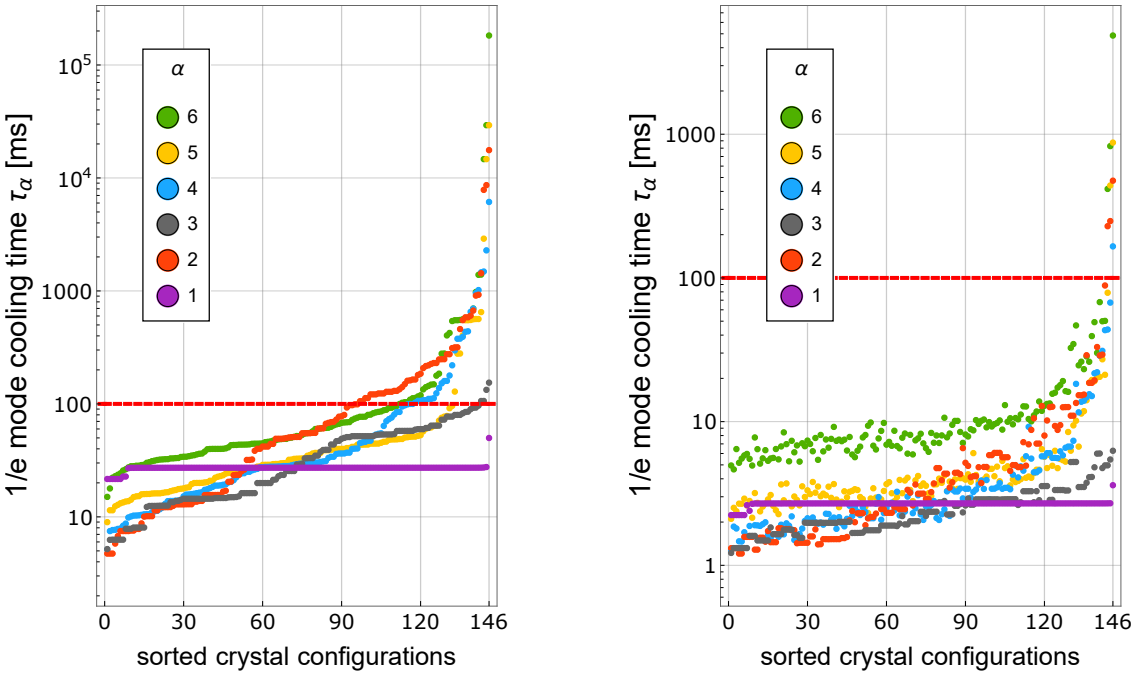

(*a*) maximal cooling times (*b*) mean cooling times

Figure 4.21: Sorted maximal and mean 1/e cooling times of motional modes for all configurations with 3 Yb^+ and 10 In^+ ions for different radial secular frequencies ratios $\alpha = 6, 5, ..., 1$. A horizontal line at $\tau_\alpha = 100\,\text{ms}$ is shown for orientation. The cooling time axis is scaled logarithmically.

contrary to the results of figure 4.16 in subsection 4.2.3, where the crystals' confinement was varied to investigate dependencies on trap parameters within the 1D crystal phase. In the one dimensional regime the cooling times change globally over all configurations with the confinement. The crossing of the phase transition to the two dimensional and afterwards also to the three dimensional phase results in motional modes with oscillations in more than one dimension and therefore also different projections of the motional modes onto the cooling laser direction. In general, this also introduces stronger non-linear mode couplings, which could cause additional heating and cooling but is not implemented in the calculations as only the first order expansion of the ions' potential is considered.
For the 3 Yb^+/10 In^+ ions composition in figure 4.21, the phase transition from 1D to 2D leads to improved 1/e maximal (mean) cooling times by a mean factor of 2.0 ± 0.8 (2.4 ± 0.7) for the transition to $\alpha = 5$ and 2.2 ± 2.6 (3.3 ± 2.5) to $\alpha = 4$, with respect to the $\alpha = 6$ condition. This continues with the transition into the 3D phase with a factor of 1.7 ± 1.2 (2.9 ± 1.4) for $\alpha = 3$, 13.3 ± 99.6 (11.1 ± 65.2) for $\alpha = 2$ and 40.4 ± 316.5 (16.5 ± 114.4) for $\alpha = 1$, again relative to the 1D, $\alpha = 6$, condition. The behaviour of the cooling times at $\alpha = 1$ is discussed in a later paragraph.
The comparably high standard deviations, which are used as errors here, demonstrate that the cooling times change differently over to configurations' ranking. This is especially true for the maximal cooling times. They only consecutively decrease with α for the best ranked third of the configurations, although the maximal cooling times for $\alpha = 2$ are almost equal to the ones for $\alpha = 3$ in this section. The other two worse ranked thirds

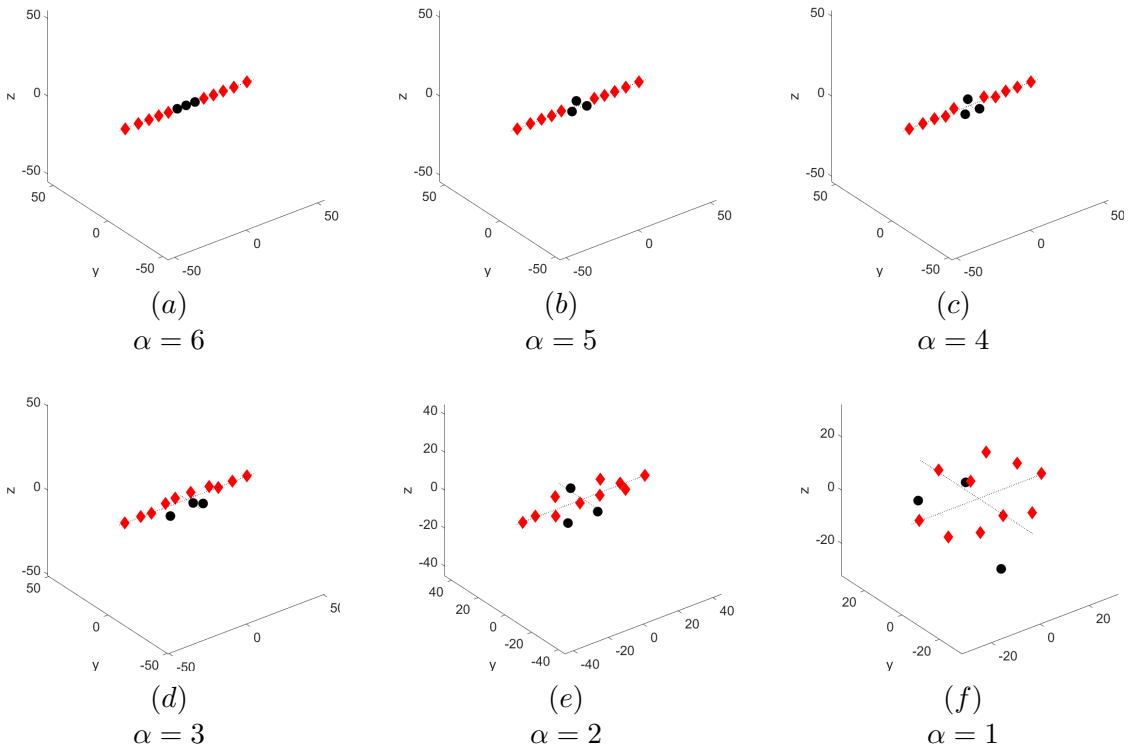

Figure 4.22: Visualization of the equilibrium positions calculated by *Matlab* for the initial 1D configuration 5 In^+ - 3 Yb^+ - 5 In^+ for the different secular frequency ratios $\alpha = 6, 5, .., 1$ used in figure 4.21. Yb^+ ions are shown in black and In^+ ions in red.

of the configurations shows no clear structure. The configuration with the secular trap frequency ratio of $\alpha = 2$ have even higher maximal cooling times than for $\alpha = 6$ in 58 out of 146 configurations.
The mean mode cooling times for the $(n_{\text{cool}}, n_{\text{clock}}) = (3, 10)$ composition however decrease monotonically with α. Only the cooling times of configurations for $\alpha = 3$ exceed cooling times of configuration with higher α-values. This may hint on the existence of local extreme points in the cooling times and could be explored further.
The most striking behaviour for the mean and maximal cooling times happens at $\alpha = 1$. The mean and maximal cooling times plateau on a single level with only some small deviations. This behaviour is probably explained by the symmetrical confinement in all directions for these conditions. In this case the minimization process in the *Matlab* code produces multiple similar equilibrium positions not necessarily dependent on the starting position of the ions, which results in similar cooling properties. This is briefly discussed in the appendix section 8.3. The plateauing behaviour should be verified experimentally or by other calculations, as it is not unlikely that the *Matlab* codes runs into minimization limits such as stopping in a local minima.

4.5 Summary

Both codes used for the previous calculations solve the first order expansion of the ions' potential for its eigenmodes and frequencies. The *Mathematica*-code does this only in one dimension and generates a solution for the axial and for one radial direction, while the *Matlab*-code calculates a full three dimensional solution, which is why only the *Matlab*-code is capable of making predictions for 2D and 3D crystals.
Figure 4.8 and figure 4.9 show that Doppler cooling times of multi species ion Coulomb crystals, which scale an eventual clock cycle, differ over several orders of magnitude and depend strongly on the choice of the configuration. This makes cooling times important when searching for a configuration to operate an ion clock with. The cooling efficiency depends on the contribution of the cooling ions in its modes' oscillatory motion. This contribution can be tuned by different parameters that have been analysed in section 4.2. Increasing the number of cooling ions in an ion crystal, decreasing the total amount of ions or decrasing the ratio between the secular frequencies $\alpha = \omega_{\mathrm{rad}}/\omega_{\mathrm{ax}}$ towards the phase transition generally reduces the cooling times of a one dimensional mixed-species Coulomb crystal. Also crossing the phase transition by reducing α even further to get a 2D and 3D crystals has an improving influence on the cooling times.
Another approach to handle long cooling times within a composition is to chose a composition with only sufficiently well cooled configurations. The $(n_{\mathrm{Yb}^+}, n_{\mathrm{In}^+}) = (5, 5)$ composition is a suitable example for this idea. As it can be seen in the appendix in figure 8.1 and figure 8.2, all maximal cooling times are below 100 ms while the mean cooling times are even lower. Of course the optimization on cooling efficiency has its limits, as other parameters are equally important. The most important example is the trade off between the number of cooling ions and clock ions. This is why this optimization process should be executed after an agreement on certain boundaries like a minimum of clock ions, a maximal number of ions or other experimental limits that may restrict the range of optimization parameters. These restrictions vary on each experimental setup and could be given, e.g., by voltage limits on trap electrodes, which determine the adjustable confinement of ions, or different detection and loading techniques.
The next chapter investigates how certain compositions and configurations can be loaded deterministically and generated experimentally.

5 Deterministic loading of Yb^+ and In^+ ions and re-ordering of mixed crystal configurations

This section describes the experimental implementation of loading and re-ordering mixed-species Coulomb crystals and puts the results in context with the previous theoretical analysis of cooling times for different configurations and compositions. First, section 5.1 and section 5.2 explain how to detect ytterbium and dark indium ions, which is the basis for a deterministic loading scheme for mixed-species Coulomb crystal described in section 5.3. Section 5.4 demonstrates which configurations can be re-ordered reliably with 2 different methods.

5.1 Ytterbium ion detection

Trapped and directly laser cooled ytterbium ions can be detected with the camera in the experimental setup (more details in subsection 3.1.3). The development and implementation of the detection algorithm was not part of this thesis but is briefly revisited here.
For each picture taken with the camera, a *C++* based routine scans for pixels with a brightness level above a certain threshold. Neighbouring pixels above the threshold are combined to an ion object consisting of a list of contributing pixels, which allows to calculate single ion positions in the camera picture via a weighted sum below the pixel resolution. The threshold is adjusted such that neighbouring ions are not combined to a single object but also a single ion is not split into multiple objects due to brightness fluctuations. This algorithm allows the experimental control unit to count and update the number of bright, cooled Yb^+ ions with the cameras update rate and feed it to the loading algorithm, which is described in section 5.3.

5.2 Indium ion detection

Contrary to ytterbium ions, the indium ions are cooled exclusively sympathetically (see section 2.2) throughout this work. Therefore no light is scattered from this ion species and the camera cannot detect them. To nevertheless detect In^+ ions, a routine, which uses only the positions of the directly detectable Yb^+ ions to calculate the total number of ions in the trap, has been developed. The routine is described in the following. In future experiments In^+ detection will be possible by implementing a 2-colour detection system.
When indium ions are loaded to the ion trap, they occur as dark spots between the directly detectable ytterbium ions. The presence of an additional indium ion changes the equilibrium positions of the ytterbium ions. If the trap parameters are chosen such that the ions form a one dimensional crystal, the equilibrium positions of the ions are not

influenced by mass and just depend on the axial secular frequency ω_{ax} and are unique for each number of trapped ions n_{total}. With a commonly used normalization factor

$$L^3 = \frac{e^2}{4\pi\epsilon_0 m\omega_{\mathrm{ax}}^2} \text{ [31]} \tag{5.1}$$

these equilibrium positions are presented in figure 5.1 relative to the trap centre.

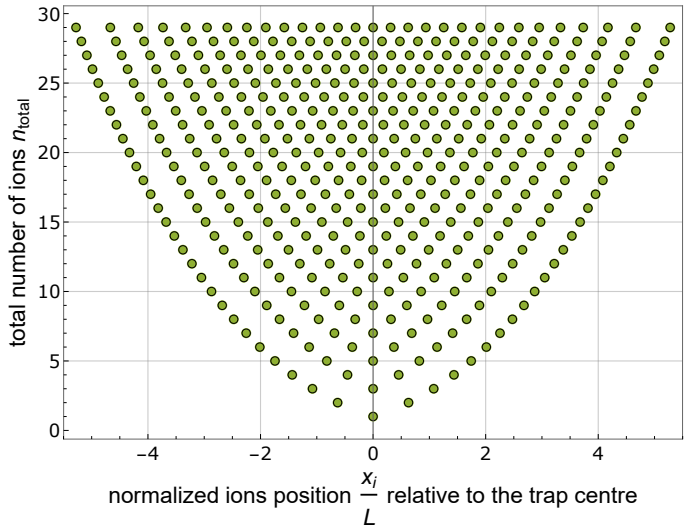

Figure 5.1: Normalized equilibrium positions x_i/L relative to the trap centre for total ion numbers n_{total} of 1 to 29. These positions are independent of the ion mass m and the axial secular frequency ω_{ax} if the normalization factor defined in (5.1) is used.

In addition to the axial secular frequency, the routine requires the position of the trap centre in the camera picture. Both parameters can be calibrated during the ytterbium loading phase to be independent of temporal drifts. The position of the first ytterbium ion determines the trap centre and the distance between the subsequently loaded ytterbium ion positions detected by the camera $campos_i$ and the theoretically calculated positions $theopos_i$ determine the axial secular frequency using the formula

$$\frac{\omega_{\mathrm{ax}}}{2\pi} = \frac{1}{n_{\mathrm{total}}} \sum_i \sqrt{\frac{e^2}{4\pi\epsilon_0 m L_i^3}} \qquad \text{with } L_i = \frac{campos_i}{theopos_i} \cdot \frac{d_{\mathrm{px}}}{M}. \tag{5.2}$$

Here i runs over all detected ytterbium ions. d_{px}/M is the resolution of the camera resulting from the magnification of the lens system M and the pixel width d_{px} (see subsection 3.1.3). Similar to the detection routine for the bright ytterbium ions, the dark ion detection algorithm, whose pseudo code is presented in figure 5.2, is executed with each exposure. It uses the positions of the ytterbium ions in the camera picture, which are saved and sorted in the *brightIonPositions* list (see positions in figure 5.1). The index n runs over the possible values for the total number of ions n_{total} starting from n_{bright} to an arbitrary number *maxLength*. For each value of n, the routine searches for a possible solution *solution* by comparing the positions of the Yb^+ ions with the theoretical ion positions. The positions need to agree within a margin of $\pm\epsilon$. A solution consists of the

```
detectDarkIons(...) {
        ...
        For (n = brightIonsPositions.size() , n <= maxLength , n++) {
                solution = searchSolution(brightIonsPositions,n);
                If (solution.size() == brightIonsPositions.size()) {
                        createIonList(n);
                        break;
                }
        }
        ...
}

searchSolution(brightIonPosition,n) {
        solution = [];
        foundIon = True;
        posToContinueWith = 0;
        For (ion = 0 , ion < brightIonPosition.size() && foundIon , ion++) {
                foundIon = False;
                For (pos = posToContinueWith , pos < n, pos++) {
                        If (|brightIonPosition(ion)*(dpx/M)/L − theopos(n,pos)| < ε) {
                                solution.pushBack(pos);
                                foundIon = True;
                                posToContinueWith = pos+1;
                                break;
                        }
                }
        }
        return solution;
}
```

Figure 5.2: Pseudo code of dark ion detection algorithm. The positions of ytterbium ions, which are directly detected by the camera, are compared to calculated equilibrium positions of a linear crystal. If both sets of positions match, the number of indium ions is given by the difference between the number of ions in the matched solution and the number of bright ions in the camera picture.

matched position indices and is only valid, if the solution list has as many entries as present ytterbium ions. In this case, the function *createIonList(n)* creates a list of dummy ion objects with the theoretical ion positions, which can be used to create regions of interests (ROI) around all ions to automatically track the crystal configuration. The number of indium ions can be obtained by subtracting the number of bright ions from the result for n_{total} of the valid solution, which can be fed to the loading algorithm and is described in the next subsection. Note that also Yb^+ molecules are counted as In^+ ions, as there is no way to distinguish between both species without making indium ions visible, switching to the 2D- or 3D-phase or doing mass spectroscopy.
A range between 0.05 and 0.08 is optimal for ϵ. Depending on the secular frequency, this is equivalent to ~ 1.2 pixels or ~ 890 nm. This range produces stable and correct results for the indium detection. The routine is successfully tested with up to 28 ions in total of which three were bright. For higher values of ϵ, the algorithm occasionally finds other valid but incorrect solutions with smaller total ion numbers. Decreasing the parameter from its optimal range towards the resolution limit of the bright ion detection eventually leads to a drop of the result for the total ion number to 0, which is the standard output if no solution is found.

5.3 Loading scheme for mixed-species Coulomb crystals

The last two sections described routines that can detect directly cooled ytterbium ions and sympathetically cooled indium ions for linear crystals with up to 28 ions in total and at least three Yb^+ ions. This subsection describes a scheme, which can be used to load an arbitrary linear Coulomb crystal with both ion species via oven loading, which is detailed in subsection 3.1.2.

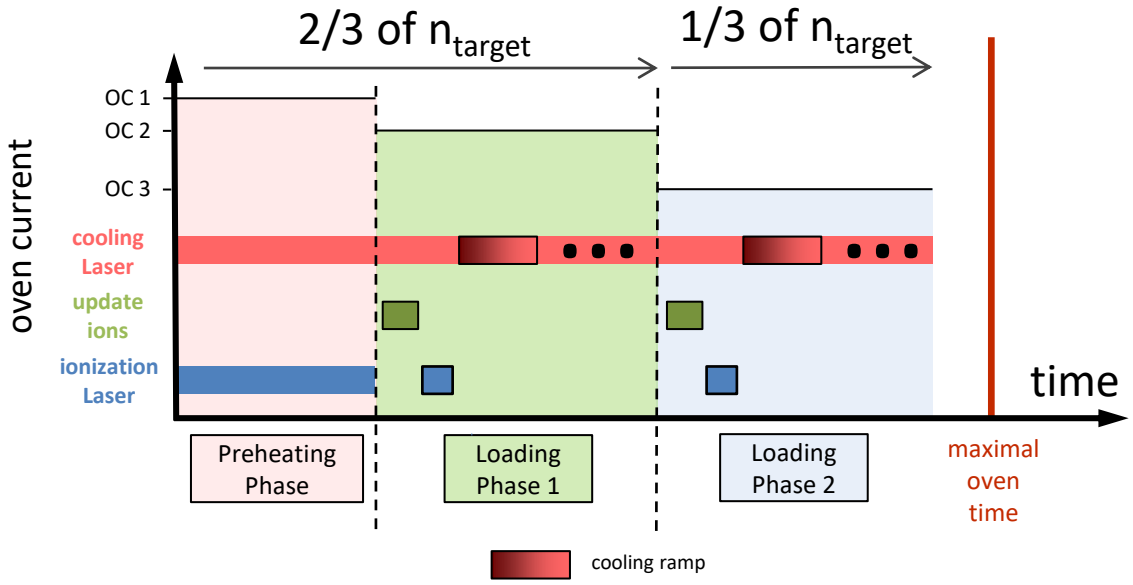

Figure 5.3: Oven loading scheme that is used to load a linear Coulomb crystal with an arbitrary number of indium or ytterbium ions n_{target} into the ion trap. The scheme is split into three phases: 1. preheating phase with a high oven current (OC 1) to reach the temperature for evaporation quickly, 2. loading phase 1 with a medium oven current (OC 2) to load two thirds of n_{target} quickly and 3. loading phase 2 with a low oven current (OC 3) to load the last third of n_{target} controlled to not overshot n_{target}. In the loading phases the routine alternates between an ionization laser pulse, cooling laser ramps and an period where the detection mechanism updates the number of loaded ions.

In the routine, the species are loaded one after the other into the trap. First, the targeted number of ytterbium ions is loaded to be able to detect indium ions (see section 5.2) and then the routine loads the targeted number of indium ions. Both loading processes are based on the same sequence, which is split into three phases as schematically presented in figure 5.3. It starts with a 45 to 90 s long preheating phase, in which the oven is operated with an increased current (9.3 A for Yb^+, 11.2 A for In^+) to reach the temperature where the solid metal piece inside the oven starts evaporating quickly. The ionization laser is shined in continuously in this phase to ionize early evaporating atoms.
The atomic beam flux exiting the oven increases exponentially over time. To prevent overshooting of the respective number of targeted ions n_{target}, the loading phase is split up into two phases. The first one (green) tries to load the first two thirds of ions quickly with a medium oven current (9.1 A for Yb^+, 11.0 A for In^+). The user can choose if the ionization laser is pulsed or runs continuously. In the second loading phase (blue), the oven current is further decreased to counteract the exponential growth of evaporation

(8.7 A for Yb^+, 10.7 A for In^+) and the last third of ions is loaded slower and therefore more controlled. In both loading phases, the routine alternates between an ionization laser pulse, ytterbium cooling laser ramps and a period where the detection mechanisms of section 5.1 and section 5.2 are used to update the number of loaded ions. For cooling ramps, the ytterbium cooling laser is tuned from $-135\,\mathrm{MHz}$ to $-\Gamma/2$ with respect to the cooling transition to cool hot ytterbium ions. If the routine fails to load the targeted number of ions within the maximal loading time of 420 s the oven and the ionization laser are switched off to prevent damage of experimental parts and excessive deposit of atoms on the trap.
During the indium loading process, the formation of ytterbium molecules is sometimes observed, which probably occurs because of impurities in the indium oven or deposits on the surrounding of the oven that evaporate if the indium oven is heated. To avoid this problem, deep UV-Light of a 230 nm laser is switched on in the indium loading process to dissociate the molecules. At the time of this work the 230 nm laser has already been prepared to enable direct indium detection and cooling but a detection system for that wavelength was still under development. For this reason the 230 nm laser could not be aligned precisely to the ions at that time. Photoelectrons from stray light of the 230 nm laser and the operation of the Indium oven move the ions axially by a few µm over the loading time. To nevertheless be able to detect the ion number correctly, tracking of this has been implemented by moving the trap centre position by 0.2 pixels whenever there is no solution of the algorithm for 5 consecutive pictures. This solution works straightforward because the ions only move in one direction.
The ytterbium and the indium loading phase are enclosed in a loop that controls the respective experimental parts to load arbitrary mixed-species Coulomb crystals.

5.4 Re-ordering of multi-ion crystals

Chapter 4 shows that cooling times for sympathetic cooling are highly relevant for multi-ion clock operation and strongly depend on the chosen configuration. This subsection presents first tests on the re-ordering of mixed crystals with total ion numbers of 8 to 20 to be able to produce well cooled configurations. Reliable re-ordering methods for longer and shorter crystals are proposed in subsection 5.4.1 and the produced configurations are ranked with respect to their calculated cooling times.
In the process of testing re-ordering methods three parameters to influence the ion configuration have been used: a change of the axial confinement, a change of the radial confinement and the application of a DC field. All of these make use of the different ion masses or more specifically the different binding strengths in the radial trap potential of In^+ and Yb^+. Other approaches would require to split up the ion crystal in different segments, re-order simpler and smaller samples and merge the crystal afterwards. The principal operations that are required for this method have been demonstrated in [32] but the implementation and merging of this operations into a working re-ordering algorithm would exceed the scope of this thesis.

5.4.1 Re-ordering methods

As shown in subsection 4.1.5, asymmetrical configurations with equally distributed cooling ions across the chain are desirable for fast cooling. Also even ion numbers are favoured over odd ion numbers. Due to their symmetric nature, the presented tools cannot produce asymmetric configurations. To produce even more favourable configurations, they could be extended with the addition of axially asymmetric forces.
All of the following re-ordering methods start from a trap confinement resulting in a linear chain of ions. They exploit the radial mass dependence by changing the trap parameters to 2D and 3D conditions so that the radially less confined heavier ytterbium ions separate from the indium ions and form a stable intermediate configuration independent from the initial configuration. After reversing the steps back to the initial condition, it is likely that the ions form a specific configuration. The tests are split into two different parameter regimes for the intermediate phase, called method A and method B. While method A works reliable for up to 14 ions, method B works for longer crystals with more than 11 ions and includes a more complicated scheme. Both methods are described on the basis of a specific Yb^+-In^+-composition and compared afterwards.

Method A

Method A is schematically presented in figure 5.4 on the basis of a 4 Yb^+- 7 In^+ crystal.

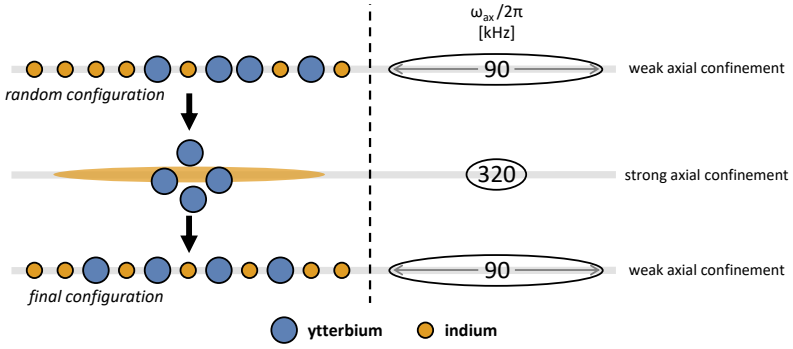

Figure 5.4: Scheme of re-ordering ***method A*** presented on the basis of a 4 Yb^+- 7 In^+ composition: maximally increase axial confinement with U_t DC voltages from 90 to 320 kHz and reverse back to initial 1D conditions. The blue circles represent ytterbium ions and the yellow circles represent indium ions. The yellow clouds represent the area where the indium ions are likely to reside during the intermediate phase. The radial secular frequencies are set to approximately 600 kHz for this method.

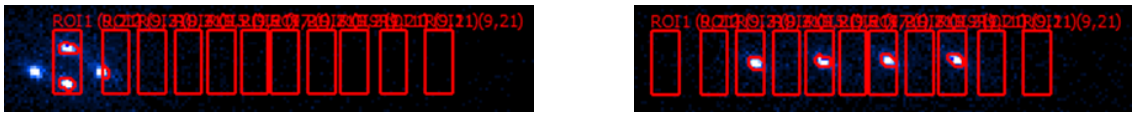

(a) intermediate configuration (b) final configuration

Figure 5.5: Camera pictures of intermediate (a) and final configuration (b) of the 4 Yb^+- 7 In^+ composition re-ordered with *method A*. 11 ROIs positioned for ions in initial 1D conditions.

The scheme starts from an arbitrary linear configuration in 1D at an axial secular fre-

quency of about 90 kHz for a single Yb^+ ion. Then the axial confinement is increased to the maximum which corresponds to a secular frequency of 320 kHz. This makes the Yb^+ ions break out into a 2D or 3D and bunch up in the centre of the trap due to their weaker radial confinement, while the In^+ ions remain radially tighter bound. Afterwards all ions are released back into the linear configuration by switching the axial secular frequency back to its initial condition. Within the tests carried out, this method produces a stable intermediate configuration for short crystals with up to 14 ions in total and 6 ytterbium ions that is independent of the initial configuration. Therefore it is likely that also the final configuration is independent of the initial configuration. In figure 5.5, camera pictures of the intermediate and final configuration using *method A* for a configuration with 4 Yb^+ and 7 In^+ ions are presented. 11 regions of interest (ROIs) are placed on the respective equilibrium positions of the linear chain to track which final configuration was produced. The trap centre shifts with different axial confinements, which is why the visible ytterbium ions centre does not match with the centre of the drawn ROIs for the intermediate configuration.
For compositions with more ions, it is likely that not all heavy ytterbium ions slide towards the centre of the 2D or 3D crystal in the intermediate configuration, as they can be blocked by local potentials of indium ions. This makes the intermediate configuration vary and results in different final configurations. A blue detuned Yb^+ cooling laser pulse can be applied to briefly heat the crystal as this gives the Yb^+ ions the energy to reach the centre of the crystal after recrystallization.

Method B

Method B, schematically presented in figure 5.6 on the basis of a 8 Yb^+-10 In^+ composition, is tested on longer crystals from 10 to 20 ions. It starts with increasing the axial

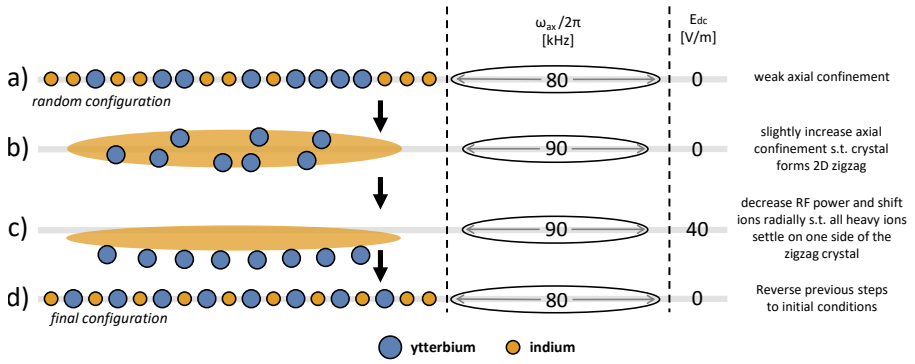

Figure 5.6: Scheme of re-ordering ***method B*** presented on the basis of a 8 Yb^+- 10 In^+ composition: a) linear crystal in random starting configuration. b) increase axial secular frequency slightly such that the crystal forms a 2D zigzag configuration from 80 to 90 kHz. c) decrease radial confinement from $\omega_{rad}/2\pi$ =600 kHz to about 400 kHz and shift ions radially with DC field E_{dc} so that the heavier Yb^+ ions settle on one side of the zigzag crystal. d) reverse previous steps to initial conditions. The blue circles represent ytterbium ions and the yellow circles represent indium ions. The yellow clouds represent the area where the indium ions are likely to reside during the intermediate phase.

confinement from about 80 to 90 kHz such that the crystal forms a 2D zigzag. Afterwards, the radial confinement is decreased from $\omega_{rad}/2\pi$ =600 kHz to about 400 kHz by tuning

the rf power and the ions are radially shifted away from the rf node with a DC field E_{dc} of approximately 40 V/m. This makes the radially weaker bound ytterbium ions settle on one side of zigzag crystal and separates both species to form a stable intermediate configuration independent from the initial configuration. In the next step the trap parameter changes are reversed to the initial conditions.
Figure 5.7 presents camera pictures of the intermediate and final configuration using *method B* for a configuration with 8 Yb^+ and 10 In^+ ions. *Method B* reliably produces interleaved configurations.

(*a*) intermediate configuration (*b*) final configuration

Figure 5.7: camera pictures of intermediate (*a*) and final configuration (*b*) of the 8 Yb^+- 10 In^+ composition re-ordered with *method B*. 18 ROIs positioned for ions in initial 1D conditions.

5.4.2 Experimental results

10 compositions with different numbers of indium and ytterbium ions are tested. The total amount of ions ranges from 8 to 20. The compositions with fewer ions are mostly re-ordered with *method A* and the longer ones with *method B*. The (5,5)-composition and the (6,10)-composition are tested with *method A* and *B* to directly compare the methods. The results of the experiments are shown in figure 5.1. For each tested composition the table gives the produced final configuration(s) with their empirical probability, if the re-ordering method works sufficiently well. In this case, the experiment is repeated about 20 times. After each repetition, the experiment is paused until the crystal is re-ordered due to a background collision to ensure random initial conditions for the next attempt.
To rate the reordering experiments in terms of cooling times, figure 5.1 also gives the calculated maximal 1/e mode cooling time τ_α of the produced final configuration and its rank within all configurations of the composition with respect to this cooling time. Symmetrically identical configurations are only counted once for the total number of configurations within one composition. τ_α represents the cooling time of the worst cooled mode (radial or axial) of a configuration and is computed as explained in chapter 4 (see (4.5)) with trap parameters of $\omega_{\mathrm{rad}} = 2\pi\,1000\,\mathrm{kHz}$, the corresponding axial secular frequency calculated with equation (2.13) to have similar Coulomb coupling for all compositions and the saturation parameter $s = 1$. Generally, the confinement in the re-ordering experiments is not the same as for the cooling time calculations, but it is possible to adjust it afterwards without an effect on the configuration.
The maximal cooling times for successfully re-ordered compositions range from 13.0 ms for the (4,4)-composition re-ordered with *method A* to 111.2 ms for the (6,10)-composition also re-ordered with *method A* and have a mean cooling time of 69.3 ms. As expected, both re-ordering methods do not achieve the best possible configurations. Over all tested compositions the methods achieve a final configuration with an average rank of 0.6, which is calculated by normalizing all configuration ranks by their respective number of possible configurations so that rank 0 is equivalent to the most efficiently cooled configuration within the composition and rank 1 is the worst. This means that the average produced

ions N_{Yb^+}	ions N_{In^+}	method A	method B	empirical probability	rank within composition	final configuration	τ_α [ms]	comment
3	8	X		20/20	44/85		59.6	
4	4	X		19/20	14/38		13.0	
				1/20	32/38		23.9	
4	7	X		17/20	84/170		37.3	
				3/20	110/170		46.3	
4	10	X		20/20	332/511		86.4	
5	4	X		17/20	30/66		15.7	
				3/20	59/66		29.8	
5	5	X		20/20	105/126		38.4	
5	5		X		44/126		17.6	
					63/126		21.9	No clear favorite.
					11/126		9.4	all sorts of
					79/126		28.1	similar configurations
						...		
6	10	X			3341/4032		113.7	No clear favorite.
					2882/4032		96.1	all sorts of
						...		similar configurations
6	10		X	18/20	2761/4032		90.1	
				1/20	2763/4032		90.2	
				1/20	3274/4032		111.2	
8	10		X	21/21	12511/21942		88.2	
9	10		X	12/24	27922/46252		98.5	other configurations
				4/24	27919/46252		98.5	occured but
				2/24	14785/46252		68.0	were unstable
10	10		X	9/16	32606/92504		76.3	
				4/16	58694/92504		109.4	
				2/16	57726/92504		107.6	
				1/16	54964/92504		97.4	

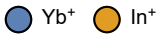

Table 5.1: Summary of the crystal re-ordering experiment: For each tested composition with N_{Yb^+} ytterbium and N_{In^+} indium ions the table gives information on the respective applied re-ordering *method*, the produced *final configurations*, their maximal 1/e mode cooling time τ_α, *empirical probability* and their *rank* of all sorted configurations within the tested composition with respect to the cooling time. The cooling times are calculated for trap parameters of $\omega_{\text{rad}} = 2\pi\,1000\,\text{kHz}$ and the corresponding axial secular frequency calculated with (2.13) to remain comparable to chapter 4.

configuration is worse than 60 % of all configurations and better than the other 40 %. The trade off between a sufficiently low cooling time and a maximally possible number of clock ions can be addressed and evaluated by normalizing the cooling times with the number of indium ions in the respective composition. This makes the final configuration of the (5,5)-composition re-ordered with *method B* with $\tau_\alpha = 9.4\,\text{ms}$ and a cooling time

per clock ion of $\tau_\alpha/N_{In^+} = 1.88\,\text{ms}$ the best option with respect to this criterion.

5.4.3 Re-ordering conclusions

Even though both presented re-ordering methods have relatively high reliabilities, the experiments should be classified as initial tests, to answer the question if re-ordering is applicable in the used experimental setup. A statistically significant analysis of the re-ordering methods is only possible with more data. One also has to test how fast the re-ordering can be carried out.
Nevertheless, a proposal for a re-ordering strategy in 1D can be made. As many configurations within the re-ordered compositions are cooled more efficiently than the final configurations of the re-ordering methods, it is not useful to generally re-order if a different configuration occurs and is detected. Rather it is more practicable to decide on a threshold 1/e cooling time, which is higher or equal to the one of the final configuration produced by a reliable re-ordering method, and re-order if the cooling time of the detected configuration rises above this threshold. The strategy also aligns with the structure of most compositions cooling times. As it can be seen in chapter 4 or in the examples of figure 4.8 and figure 4.9, a composition mainly consists of mostly efficiently cooled configurations and only few less efficiently cooled configurations. The proposed re-ordering strategy would cut off this latter part and lead to clock operation on the basis of many different but efficiently cooled configurations with optimal or medium cooling times. The strategy also reduces the amount of required re-ordering applications. Even though all re-ordering experiments were done manually and can be accelerated by automatization of the processes, each experiment will claim a certain time within the clock cycle, where the clock cannot be operated and therefore need to be kept as short as possible.

6 Mitigating micromotion-induced non-thermal heating of ions in a Coulomb crystal

The chapter covers cooling experiments on a single ytterbium ion, which is intentionally exposed to micromotion. As suggested in section 4.4, operating a multi-ion clock with two- or three-dimensional Coulomb crystals could be useful in terms of cooling times. However, an ideal linear Paul trap's electric field only vanishes along the axial trap axis but is generally non-zero elsewhere, which induces excess micromotion (EMM - see subsection 2.1.1). EMM can reduce or even reverse the effect of typical Doppler cooling and result in non-thermal heating. Depending on the size of the crystal, this poses a major problem as intensive heating can increase motional shifts or lead to a loss of ions. Reference [9] proposes a cooling technique which is able to maintain temperatures close to the Doppler limit while being exposed to EMM. The predictions are tested with a single $^{172}Yb^{+}$ ion. The following subsections firstly summarize the relevant parts of [9] in section 6.1. Section 6.2 and section 6.3 give a detailed description of the experiment and present measurements that build the basis and preconditions for the main experiment. This includes the spectroscopy sequence and a calibration of the electrode voltage that controls the EMM amplitude in the setup. Lastly, the results of the main cooling experiment with EMM are shown and compared to the theoretical predictions from [9] in section 6.4. The experimental data follows the theory qualitatively. The deviations are discussed in the conclusion in section 6.5.

6.1 Cooling EMM exposed ions - theory overview

Calculations for a single ion in a Paul trap that is exposed to EMM are presented in [9]. The motion of the ion is described with the classical action angle coordinates and laser cooling is introduced as a perturbation of the system. With additional stray fields that displace the ion from the trap centre, the ion's motion[1] $z(t)$ transforms to

$$z(t) = A_0 + \frac{1}{2}A_z \cos\Omega t + u(t), \tag{6.1}$$

where A_0 is a spatial displacement, Ω the Paul trap's radio frequency, $\frac{1}{2}A_z$ the EMM amplitude and $u(t)$ a time-dependent function that describes the motion of the ion that is not periodic in Ω. In the low saturation limit of the Doppler cooling laser, the model is evaluated in three different regimes of the ratio between the micromotion frequency Ω and the linewidth of the cooling transition Γ: $\Omega \ll \Gamma, \Omega \approx \Gamma$ and $\Omega \gg \Gamma$.
In the presence of EMM, Doppler cooling with a cooling laser detuning of $-\Gamma/2$ with

[1] The motion is considered to be one-dimensional (here z), with the micromotion direction parallel to the displacement.

respect to the cooling transition can lead to non-thermal heating, when $\Omega \approx \Gamma$ or $\Omega > \Gamma$. This happens due to excitation of the micromotion sidebands, which are blue detuned with respect to the cooling laser. To re-establish effective cooling, the laser needs to be detuned to the red side of the micromotion sidebands depending on the EMM amplitude.

6.2 Experimental description and methods

This subsection describes the experimental sequence and methods for measuring the non-thermal heating due to micromotion. First, a single Yb^+ ion is prepared as per the spectroscopy sequence described in figure 3.4. This involves a reference image, a Doppler cooling and optical pumping pulse with standard detuning discussed in subsection 3.2.1. Afterwards the ion is shifted out of the trap centre with the DC compensation (U_{ec}) voltages where an additional cooling and pumping pulse is applied. Then, the values for detuning and applied U_{ec} voltage are varied to measure the heating of the ion. Finally, the ion is shifted back to the trap centre and the experimental cycle continues with state detection and repumping as in the standard spectroscopy cycle. This is schematically presented in figure 6.1.

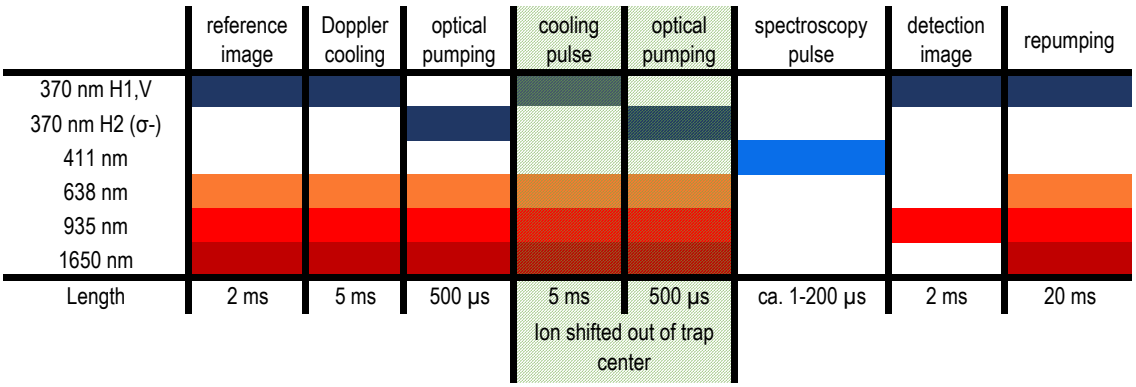

Figure 6.1: Experimental sequence of the Yb^+ ion temperature measurement under excess micromotion consisting of a reference image, Doppler cooling and optical pumping. Then, the ion is shifted out of the trap centre with DC voltages, Doppler cooled and optically pumped again. Afterwards the ion is shifted back, detected and repumped like in the usual spectroscopy cycle.

The U_{ec} electrodes shift the ion along the radial negative x axis out of the trap (see figure 6.2 (a)). The U_e voltages are set so that strong radial secular trap axis aligns with the y axis and the spectroscopy laser only addresses carrier transitions and sidebands of a single secular mode. Even with the applied trap voltages, the radial trap axis deviates by 2-3° from the spectroscopy laser axis in the y direction in the experiment. This deviation nonetheless can lead to additional heating by the non-vanishing projection of the H1 cooling laser on the trap axis. However, this effect has been excluded by measurements that are not described in this thesis.
The compensation electrode voltages U_{tc} and U_{ec} are set so that the ions residual micromotion is minimized at the initial ion position. The ion is cooled vertically with the cooling beam V and in the horizontal plane with the cooling beam $H1$.
With this modified spectroscopy cycle Rabi flops are measured to evaluate temperatures or mean motional state numbers $\bar{n}$ of the probed Yb^+ ion for the chosen parameter sets.

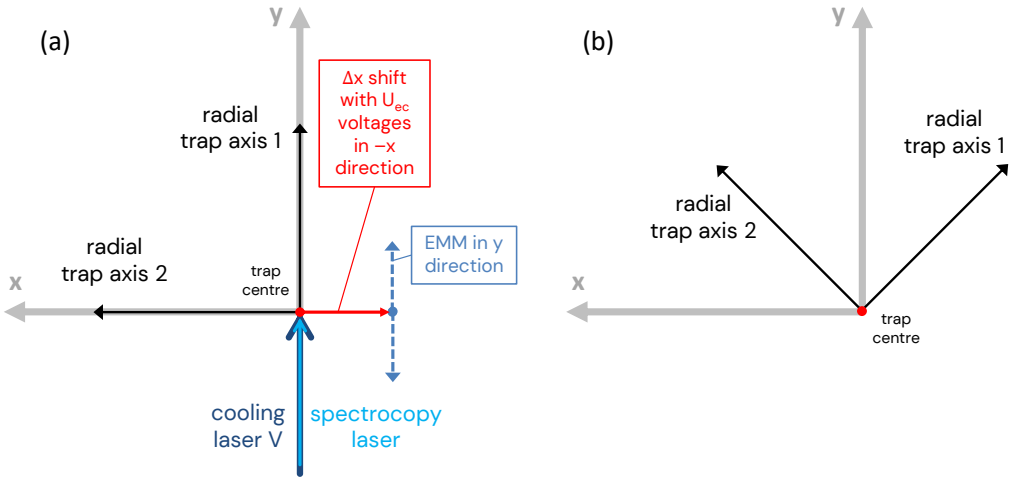

Figure 6.2: (a) A schematic of ion motion and laser orientation in the EMM experiment in the radial plane. U_{ec} electrode DC voltages are used to displace the Yb^+ ion along the negative x axis, which leads to EMM in the y direction. The spectroscopy laser probes the ion along the y axis. In the same axis, cooling is performed with the V laser. Additionally, the ion is cooled by the H1 laser in the xz plane. The trap axes are rotated so that the spectroscopy laser only addresses a single motional mode. (b) Visualization of trap axis rotation for minimization of micromotion measurement.

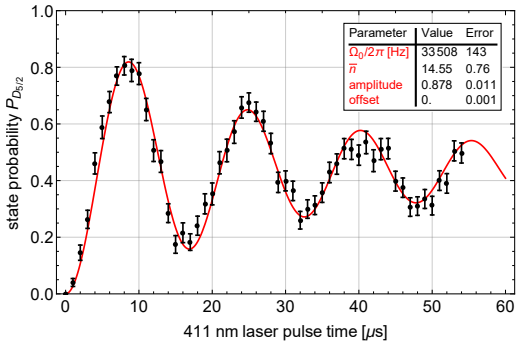

(*a*)
The ion is displaced from the rf nodal line but the second cooling step is replaced with a delay.

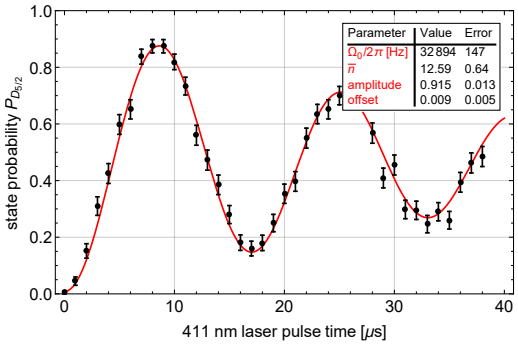

(*b*)
A second cooling step is applied but the ion is not displaced from the rf nodal line.

Figure 6.3: Measurements to validate the cooling experiment of an ion exposed to excess micromotion. The different modifications in (*a*) and (*b*) in the spectroscopy cycle from figure 6.1 should not change the results of the temperature evaluation so that eventual changes can be purely attributed to the cooling laser heating the ion if it is exposed to EMM. If the ion heats up, the evaluated mean phonon number $\bar{n}$ deviates from the value that corresponds to the Doppler temperature $\bar{n}_D$. For a radial secular frequency of $\nu_{\mathrm{rad}} = 568\,\mathrm{kHz}$ this value is $\bar{n}_D \approx 17$.

The theory behind this temperature measurement method is explained in section 2.3. The following measurements verify that no other heating processes are involved and that the modifications on the spectroscopy cycle do not influence the ion's motional state. Sub-

section 3.2.2 presents the basic heating rate of the trap without the presence of any lasers. As the calculated heating rate with less than 1 phonon/s is on a much slower timescale than the temperature measurements under EMM (spectroscopy cycle time is $< 40\,\mathrm{ms}$), this heating process can be neglected. Figure 6.3 (a) shows a measurement of the ion heating when the ion is displaced from the trap centre but the second cooling step is exchanged with an equal length delay of 5 ms in the spectroscopy cycle. At the resolution of this measurement, no heating is detected. Reference [33] measures this heating process quantitatively in a similar setup and agrees with this result.
The measurement shown in figure 6.3 (b) tests for a potential influence of the second cooling pulse in the spectroscopy cycle without shifting the ion out of the trap centre. Neither of the measurements heats the ion, which is why all potentially occurring heating can be attributed to the V cooling laser heating the ion in the presence of EMM.

6.3 Estimating the relation between the trap voltages and electric field amplitude

The relation between the U_{ec} trap voltage, that shifts the ion away from the trap centre in this experiment, and the resulting electric field amplitude E_{rf}, that acts on the ion and causes micromotion, is experimentally determined in this section. This relation is important to compare the experimental data presented in subsection 6.4.1 and subsection 6.4.2 to the theoretical predictions from [9] and to evaluate the experimental results in general. For small displacements Δx compared to the distance between the ion and the trap electrodes $d/2$, the relation $E_{\mathrm{rf}}(U_{\mathrm{ec}})$ can be assumed to be linear. In the following experiments this is valid, as the maximal displacement[2] is approximately 3 µm and the distance between the ion and the U_{ec} trap electrodes $> 1\,\mathrm{mm}$ [22]. If the displaced ion is exposed to micromotion, all lasers are phase modulated at the rf-drive frequency Ω_{rf} in its rest frame. This also affects the coupling strength of the spectroscopy transition and its sidebands. The relative coupling strength of the carrier spectroscopy transition Ω_0 and the first sideband Ω_1 is equal to ratio of the zeroth and the first order Bessel function $J_0(\beta)$ and $J_1(\beta)$ [34]

$$\frac{\Omega_1}{\Omega_0} = \frac{J_1(\beta)}{J_0(\beta)}. \tag{6.2}$$

A measurement of both Rabi frequencies allows to determine the modulation index β, which can be directly related to the electric field amplitude E_{rf} using

$$E_{\mathrm{rf}}(\beta) = \frac{m\Omega_{\mathrm{rf}}^2}{ke}\beta, \tag{6.3}$$

with the angular wavenumber k, the elementary charge e and the ions mass m. Such data was measured and evaluated in figure 6.4.
A fit estimates the relation to be

$$E_{\mathrm{rf}}(U_{\mathrm{ec}}) = (2559 \pm 18)\frac{\mathrm{V/m}}{\mathrm{V}} \cdot U_{\mathrm{ec}} - (259 \pm 19)\frac{\mathrm{V}}{\mathrm{m}}. \tag{6.4}$$

Besides the slope, this fit also reveals an offset in the E_{rf} minimizing U_{ec} voltage, that occurs if the trap axes are turned from the trap configuration presented in figure 6.2 (b)

[2] calculated with formulas from subsection 2.1.1

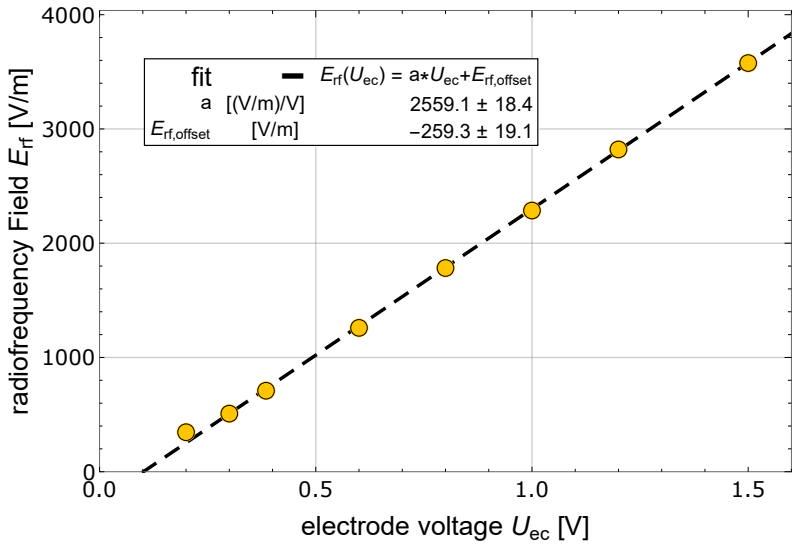

Figure 6.4: Relation between DC compensation voltage U_{ec}, which shifts the ion out of the trap centre, and the resulting radio frequency field amplitude E_{rf}. The measurement is performed by comparing amplitudes of the carrier and first micromoton sideband of the spectroscopy transition and deducing the modulation index β. The latter is proportional to E_{rf} (see eq. 6.3). The relation is approximated with a linear fit.

to the spectroscopy configuration in (a) in the same figure. The relation in (6.4) is taken into account in the rest of this chapter.

6.4 Experimental results and comparison to theory

This section presents the experimental results and compares them to theoretical data from [9]. The paper describes micromotion in terms of a double spatial EMM amplitude A_z (see (6.1)), where the z direction is chosen to be the micromotion driven coordinate. This quantity can be expressed in terms of the radio frequency electric field amplitude E_{rf} by deriving

$$E_{\mathrm{rf},i}\left(\vec{r}\right) = -\frac{\partial \phi_{\mathrm{rf}}}{\partial r_i}\left(\vec{r}\right) = \frac{\kappa_{\mathrm{rf}} U_{\mathrm{rf}}}{d_{\mathrm{rf}}^2} \cdot r_i \tag{6.5}$$

from (2.1) and substituting into

$$A_y = q_y\, r_y = \frac{2e\kappa_{\mathrm{rf}} U_{\mathrm{rf}}}{m d_{\mathrm{rf}}^2 \Omega_{\mathrm{rf}}^2} \cdot r_y = \frac{2e}{m\Omega_{\mathrm{rf}}^2} \cdot E_{\mathrm{rf},y} \tag{6.6}$$

using (2.4) and (2.9). As (6.6) only compares amplitudes, factors of -1 and time-dependent oscillations $\cos\left(\Omega_{\mathrm{rf}}\, t\right)$ are neglected. The theoretical data are provided in discrete steps, which is why the experimental datasets are compared to the respective closest theoretical values.
In the following two subsections the experimental data of two measurement series are shown. The related uncertainties are discussed in subsection 6.4.3 afterwards.

6.4.1 Temperature vs EMM amplitude

The following measurements determine the effect of the micromotion amplitude on temperature for a fixed laser detuning. The EMM amplitude is tuned by the U_{ec} voltage, which displaces the ion from the trap centre. The measurement is repeated for three values of the cooling laser detuning $\Delta/\Gamma_{\mathrm{Yb}} = -0.5, -1.1$ and -1.9. The respective results

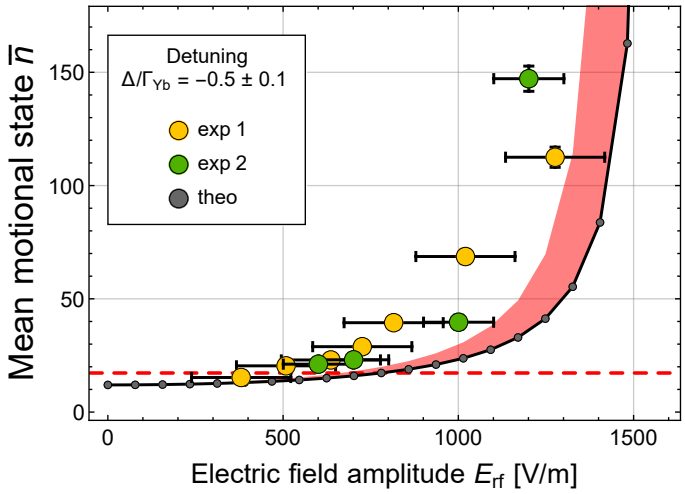

Figure 6.5: Experimental (big yellow and green circles) and theoretical (small grey circles) mean motional state $\bar{n}$ vs EMM amplitude E_{rf} for a cooling laser detuning of $\Delta/\Gamma_{\mathrm{Yb}} = -0.5 \pm 0.1$. The two experimental data sets were acquired as explained in section 2.3 on different days and have different uncertainties (see discussion in subsection 6.4.3). The theoretical data for $\Delta/\Gamma_{\mathrm{Yb}} = -0.5$ from [9] are shown in grey. The area enclosed between the theoretical data for $\Delta/\Gamma_{\mathrm{Yb}} = -0.6$ and -0.5 is shown as a red area to represent the experimental uncertainty of the laser detuning. A red horizontal line at the mean motional state number $\bar{n} \approx 17$, that corresponds to the Doppler temperature, is drawn for orientation.

are presented in figure 6.5, figure 6.6 and figure 6.7. While $\Delta/\Gamma_{\mathrm{Yb}} = -0.5$ is the typical detuning for Doppler cooling, $\Delta/\Gamma_{\mathrm{Yb}} = -1.1$ and -1.9 are settings so that the cooling laser is detuned by 0.2 to $0.3 \cdot \Gamma_{\mathrm{Yb}}$ to the red side of the first and second micromotion sideband of the cooling transition.
As expected for all three measurements, the ion temperature increases for high electric field amplitudes E_{rf}. Even higher micromotion amplitudes cause stronger heating and the measurement method fails as the ion's motional distribution becomes non-thermal (see section 2.3). Additionally the ion is cooled when the cooling laser is red-detuned with respect to the EMM sideband and is heated when its blue detuned. With an increasing E_{rf}, the amplitudes of the micromotion sidebands and the carrier transition change proportional to the respective Bessel functions. Starting from no coupling to the micromotion sidebands for $E_{\mathrm{rf}} = 0$, the ratio of red and blue transitions changes significantly towards the blue transitions for $E_{\mathrm{rf}} > 0$. The point where the motional distribution becomes non-thermal depends on the detuning. The detunings $\Delta/\Gamma_{\mathrm{Yb}} = -1.1$ and -1.9 ensure thermal distributions up to higher micromotion amplitudes. However, the higher detunings cannot cool the ion to its Doppler temperature for low micromotion amplitudes, especially for $E_{\mathrm{rf}} = 0$ as seen in figure 6.7. Although the experiment follows the theoretical data qualitatively for all three detunings, they do not agree quantitatively within their uncertainties, which are discussed in subsection 6.4.3.

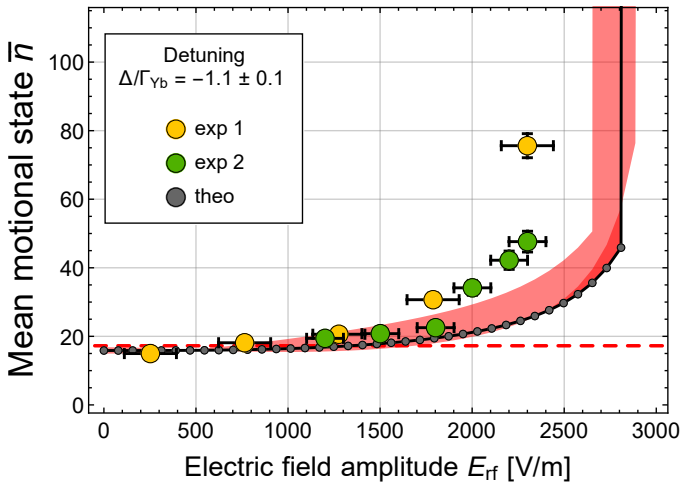

Figure 6.6: Experimental (big yellow and green circles) and theoretical (small grey circles) mean motional state $\bar{n}$ vs EMM amplitude E_{rf} for a cooling laser detuning of $\Delta/\Gamma_{\mathrm{Yb}} = -1.1 \pm 0.1$. The two experimental data sets were acquired as explained in section 2.3 on different days and have different uncertainties (see discussion in subsection 6.4.3). The theoretical data for $\Delta/\Gamma_{\mathrm{Yb}} = -1.1$ from [9] are shown in grey. The area enclosed between the theoretical data for $\Delta/\Gamma_{\mathrm{Yb}} = -1.2$ and -1.0 is shown as a red area to represent the experimental uncertainty of the laser detuning. A red horizontal line at the mean motional state number $\bar{n} \approx 17$, that corresponds to the Doppler temperature, is drawn for orientation.

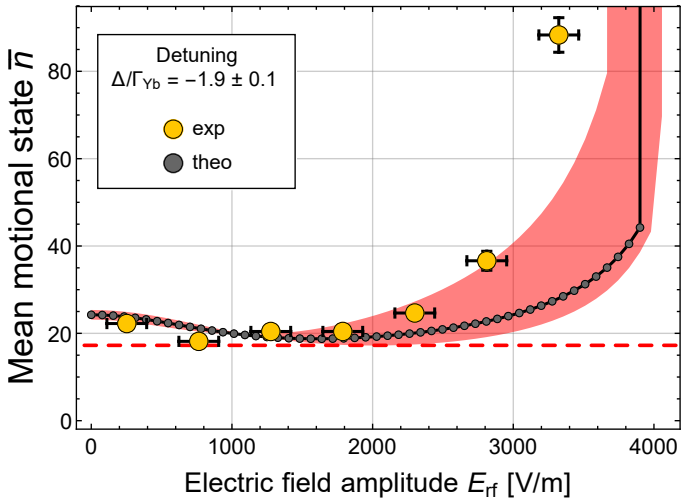

Figure 6.7: Experimental (big yellow circles) and theoretical (small grey circles) mean motional state $\bar{n}$ vs EMM amplitude E_{rf} for a cooling laser detuning of $\Delta/\Gamma_{\mathrm{Yb}} = -1.9 \pm 0.1$. The experimental data set was acquired as explained in section 2.3 with uncertainties as discussed in subsection 6.4.3. The theoretical data for $\Delta/\Gamma_{\mathrm{Yb}} = -1.9$ from [9] are shown in grey. The area enclosed between the theoretical data for $\Delta/\Gamma_{\mathrm{Yb}} = -2.0$ and -1.8 is shown as a red area to represent the experimental uncertainty of the laser detuning. A red horizontal line at the mean motional state number $\bar{n} \approx 17$, that corresponds to the Doppler temperature, is drawn for orientation.

6.4.2 Temperature vs detuning

This subsection determines the effect of the laser detuning on temperature for a fixed micromotion amplitude. The measurement is repeated for three values of EMM amplitude $E_{\mathrm{rf}} = 726, 1276$ and $2812\,\mathrm{V/m}$. The respective data is presented in figure 6.8, figure 6.9 and figure 6.10. The measurement presented in the previous subsection in figure

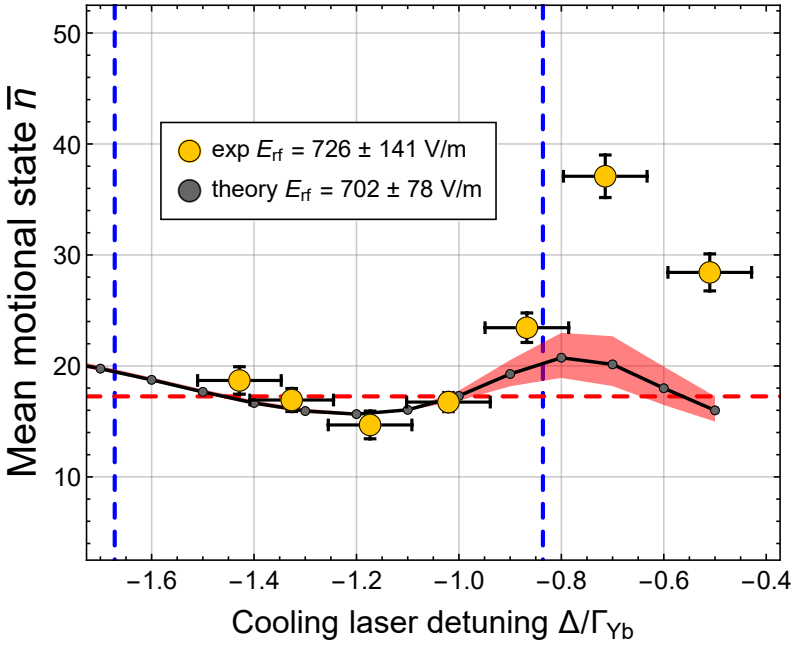

Figure 6.8: Mean motional state number $\bar{n}$ vs cooling laser detuning $\Delta/\Gamma_{\mathrm{Yb}}$ depicted in yellow for a constant micromotion amplitude $E_{\mathrm{rf}} = 726 \pm 141\,\mathrm{V/m}$. The experimental data is acquired as described in section 2.3 and its uncertainties are discussed in subsection 6.4.3. The discrete theoretical data set provided by [9] corresponding to $E_{\mathrm{rf}} = 702\,\mathrm{V/m}$, which is closest to the experimental micromotion amplitude, is shown in grey. The area enclosed by the discrete theoretical values above and below is shown in red to reflect the cooling laser detuning dependent sensitivity of $\bar{n}$ on E_{rf} and the experimental uncertainty. The discrete steps between the theoretical data are $78\,\mathrm{V/m}$. A red horizontal line at the mean motional state number $\bar{n} \approx 17$, that corresponds to the Doppler temperature, is drawn for orientation. Also blue vertical lines are shown where the detuning matches the micromotion sidebands at $n \cdot \Omega_{\mathrm{rf}}/\Gamma_{\mathrm{Yb}} = 0.836$ and 1.672.

6.5 showed, that the typical Doppler cooling detuning of $\Delta/\Gamma_{\mathrm{Yb}} = -0.5$ is not able to produce motional distributions close to the Doppler limit for higher EMM amplitudes. These findings are supported by the measurements in this subsection. For all three values of E_{rf}, no laser detuning between the carrier and first micromotion sideband transition is able to cool the ion and approach a mean motional state number, that corresponds to the Doppler limit (red dashed line in the plots).
For the amplitudes $E_{\mathrm{rf}} = 726$ and $1276\,\mathrm{V/m}$, laser detunings on the red side of the first micromotion sideband at $\Delta/\Gamma_{\mathrm{Yb}} = -0.836$ can produce thermal distributions with a mean motional state number $\bar{n}$ below 25, close to the Doppler limit at $\bar{n}_{\mathrm{D}} \approx 17$. For the highest EMM amplitude of $E_{\mathrm{rf}} = 2812\,\mathrm{V/m}$, no detuning of up to $\Delta/\Gamma_{\mathrm{Yb}} \approx -2.4$ achieves temperatures close to the Doppler limit. However, for a cooling laser detuning on the red side of the second micromotion sideband at $\Delta/\Gamma_{\mathrm{Yb}} = -1.672$, thermal motional distributions around $\bar{n}$ of ~ 40 with a minimum of $\bar{n} = 39$ can be produced.

All three measurement series only qualitatively agree with the plotted theoretical data. Quantitatively only a few data points agree within the uncertainties.

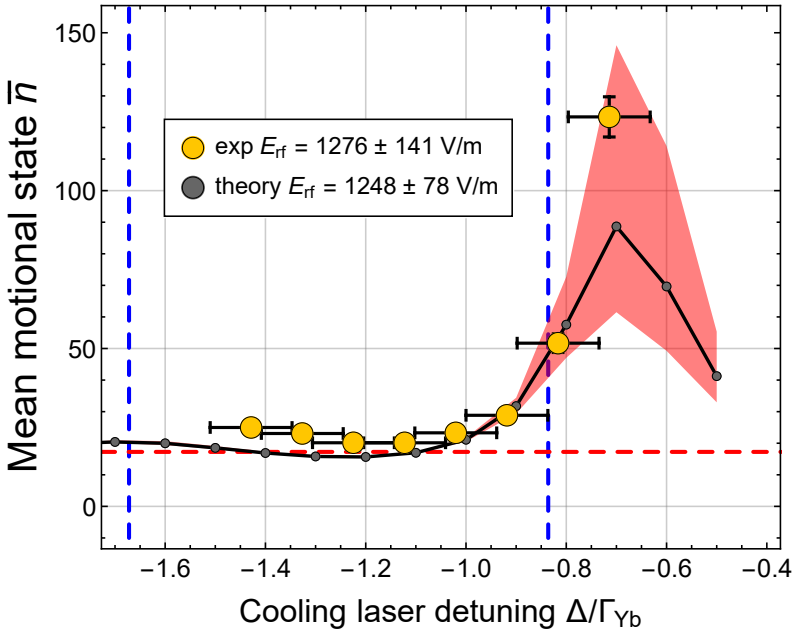

Figure 6.9: Mean motional state number $\bar{n}$ vs cooling laser detuning $\Delta/\Gamma_{\mathrm{Yb}}$ depicted in yellow for a constant micromotion amplitude $E_{\mathrm{rf}} = 1276 \pm 141\,\mathrm{V/m}$. The experimental data is acquired as described in section 2.3 and its uncertainties are discussed in subsection 6.4.3. The discrete theoretical data set provided by [9] corresponding to $E_{\mathrm{rf}} = 1248\,\mathrm{V/m}$, which is closest to the experimental micromotion amplitude, is shown in grey. The area enclosed by the discrete theoretical values above and below is shown in red to reflect the cooling laser detuning dependent sensitivity of $\bar{n}$ on E_{rf} and the experimental uncertainty. The discrete steps between the theoretical data are $78\,\mathrm{V/m}$. A red horizontal line at the mean motional state number $\bar{n} \approx 17$, that corresponds to the Doppler temperature, is drawn for orientation. Also blue vertical lines are shown where the detuning matches the micromotion sidebands at $n \cdot \Omega_{\mathrm{rf}}/\Gamma_{\mathrm{Yb}} = 0.836$ and 1.672.

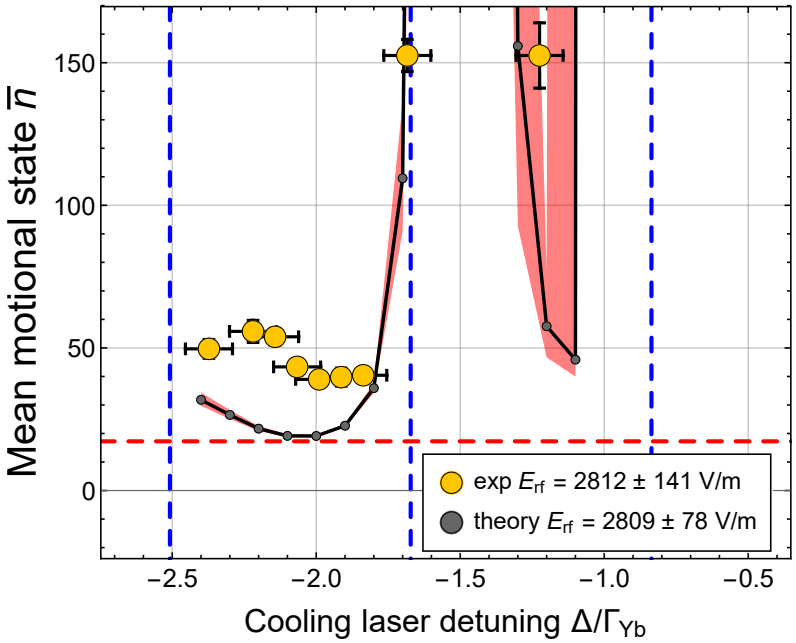

Figure 6.10: Mean motional state number $\bar{n}$ vs cooling laser detuning $\Delta/\Gamma_{\mathrm{Yb}}$ depicted in yellow for a constant micromotion amplitude $E_{\mathrm{rf}} = 2812 \pm 141\,\mathrm{V/m}$. The experimental data is acquired as described in section 2.3 and its uncertainties are discussed in subsection 6.4.3. The discrete theoretical data set provided by [9] corresponding to $E_{\mathrm{rf}} = 2809\,\mathrm{V/m}$, which is closest to the experimental micromotion amplitude, is shown in grey. The area enclosed by the discrete theoretical values above and below is shown in red to reflect the cooling laser detuning dependent sensitivity of $\bar{n}$ on E_{rf} and the experimental uncertainty. The discrete steps between the theoretical data are 78 V/m. A red horizontal line at the mean motional state number $\bar{n} \approx 17$, that corresponds to the Doppler temperature, is drawn for orientation. Also blue vertical lines are shown where the detuning matches the micromotion sidebands at $n \cdot \Omega_{\mathrm{rf}}/\Gamma_{\mathrm{Yb}} = 0.836, 1.672$ and 2.508.

6.4.3 Uncertainty discussion

The experimental data of this chapters measurement, that is presented in subsection 6.4.1 and subsection 6.4.2, does not agree with the theoretical data from [9]. This motivates the following discussion of the uncertainties of the experimental data.

Micromotion amplitude uncertainty

A conservative uncertainty of $\pm 100\,\mathrm{V/m}$ in the micromotion amplitude (E_{rf}) is applied to the experimental data of the first measurement series (experimental data presented in yellow in subsection 6.4.1 and subsection 6.4.2) because the ion trap's potential centre was not accurately determined for these data points. Additionally a measurement of the trap's potential centre after the second measurement series (data presented in green) revealed an occurrence of a trap centre shift during the measurement process. This shift of $\pm 100\,\mathrm{V/m}$ is applied to all experimental data in subsection 6.4.1 and subsection 6.4.2 as the occurrence of this shift cannot be excluded for the other experiments.

Cooling laser detuning uncertainty

The uncertainty in the cooling laser detuning mainly consists of the frequency uncertainty of the measurement of the carrier cooling transition. This uncertainty is 1.6 MHz in absolute frequency units and results in a rounded uncertainty of $u(\Delta/\Gamma_{\mathrm{Yb}}) \approx \pm 0.1$. This uncertainty is included in all experimental and theoretical data in subsections 6.4.1 and 6.4.2.

Mean motional state number uncertainty

The uncertainties in the mean motional state number $\bar{n}$ are extracted from the fit of the thermal distribution model onto measured the Rabi flop (see section 2.3). This uncertainty varies for all data points.

6.5 Conclusion

The measurements presented in subsection 6.4.1 and subsection 6.4.2 qualitatively agree with the calculations from [9]. However, quantitatively the data does not agree within the uncertainties, which are discussed in subsection 6.4.3, and deviate significantly from the theoretical data. More specifically, throughout all measurement series, it seems that the experiment measures higher micromotion amplitudes than the theory predicts. Unfortunately no clear source has yet been identified for these discrepancies. Regardless, the measurements show that cooling of single Yb^+ ions that are exposed to excess mircomotion can be significantly improved if the cooling laser is detuned far enough to the red side of micromotion sidebands of the cooling transition. The required detuning strongly depends on the micromotion amplitude.

7 Summary

This thesis presents theoretical calculations and experimental measurements to improve multi-ion clock operation with mixed-species Coulomb crystals. The chosen platform for these experiments is a Paul trap which stores ytterbium ions for sympathetic cooling and indium ions for clock interrogation.
Efficient laser cooling is an essential part of the clock cycle, as it reduces motional shifts and prevents ions gaining kinetic energy and escaping the trap. This thesis provides a model that calculates motional mode 1/e cooling times for linear Coulomb crystals which depend on the participation of the cooling ions in the respective mode. It is shown that the cooling times are strongly influenced by the crystal composition and configuration as well as by the confinement in the trap, and can differ by several orders of magnitude. Figure 7.1 presents cooling times for an example composition. Generally, shorter crystals, more

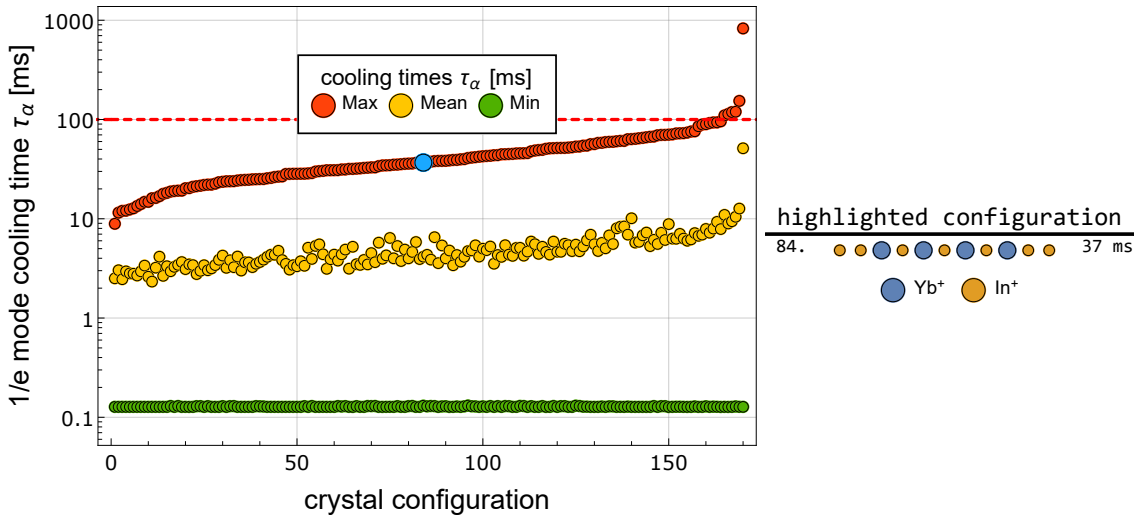

Figure 7.1: Sorted maximal, mean and minimal cooling times τ_α for radial and axial modes for the trap confinement ratio $\alpha \approx 5.7$ for all 170 unique possible configurations with 4 Yb^+ an 7 In^+ ions. A horizontal line at $\tau_\alpha = 100\,\text{ms}$ is shown for orientation. The cooling time axis is scaled logarithmically. The configuration that is generated with a re-ordering method with the highest empirical probability is highlighted in blue and presented with its rank within the composition and its maximal cooling time.

cooling ions in the crystal composition and a trap confinement in linear configuration close to the phase transition to a 2D crystal are favourable for cooling times. As the motional mode spectrum complexity quickly increases with the crystal size, no trivial recipe for the configuration of clock and cooling ions for optimally cooled, longer crystals can be devised. The results show that cooling times improve when configurations are not symmetrical and the cooling ions are evenly distributed across the crystal. The thesis also discusses finite cooling times and determines the dependence of motional shifts on the analysed parame-

ters. Further calculations should include the influence of the Debye-Waller effect [35] and could evaluate the prospects of direct cooling on indium.
Using another model [30], cooling times for 2D and 3D crystals are also calculated. These predict that sympathetic cooling might work better in higher dimensional crystals. More details on the calculations of cooling times can be found in chapter 4.

After this theoretical consideration, the question arises how and if certain crystal composition and configurations can be loaded and generated experimentally. For this purpose, a scheme to deterministically load compositions of In^+ and Yb^+ is developed and tested for up to 28 ions. This requires detection schemes for dark indium ions, using a camera detecting ytterbium fluorescence. The amount of loaded indium ions is determined by comparing theoretically calculated linear crystal positions with the detected positions of the bright ytterbium ions.
As background gas collisions can randomize the crystal configuration, re-ordering is investigated to produce efficiently cooled configurations. Possible tools available are the change of the axial and radial trap confinement and the application of DC fields. Two methods based on these tools have proven to be reliable, which separate both ion species from each other via the mass dependence of the radial confinement in an intermediate phase. In this way, after a reversal of the applied changes, configurations are produced which are independent of the starting configuration. Figure 7.2 presents a schematic of the intermediate phases of both re-ordering approaches.

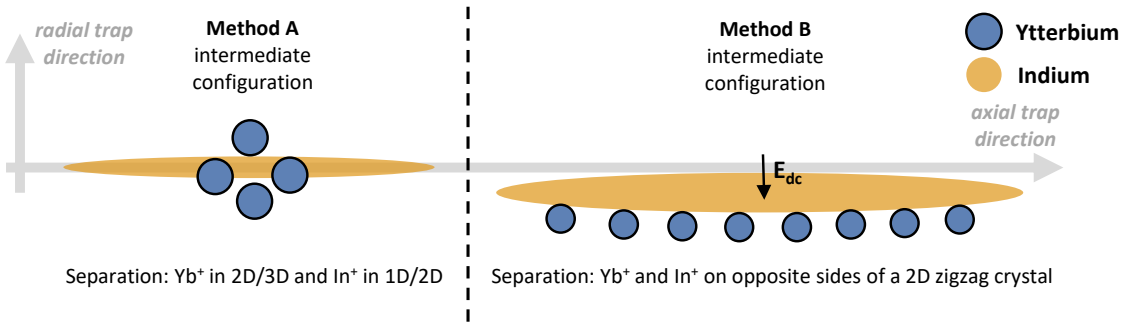

Figure 7.2: A schematic of the intermediate configurations of two reliable re-ordering methods, which separate both ion species from each other via changes in trap potentials and applications of DC fields. In this way, after a reversal of the applied changes, configurations are produced which are independent of the starting configuration. Indium ions are represented by a yellow cloud, since their positions cannot be detected in the intermediate configuration.

Since these methods can only produce certain configurations, the choice of the crystal composition needs to take into account their respective cooling times. Figure 7.1 shows how the configuration produced with a re-ordering method compares to the overall set of cooling times of their composition. A statistically significant analysis of the re-ordering methods will be carried out once a higher level of automatization has been implemented. The loading scheme and the reordering experiments are presented in chapter 5.

As a last topic, this thesis presents experiments that work towards cooling of higher dimensional Coulomb crystals. In a Paul trap, ions which do not reside on the nodal line of the confining rf electric field undergo excess micromotion (EMM). In this case, the

intended effect of Doppler cooling can be reduced or even lead to additional non-thermal heating. This is due to excitation of red micromotion sidebands of the cooling transition [9]. Reference [9] proposes a technique in which the cooling laser is further detuned to the red side of the sidebands to prevent heating. Chapter 6 implements this experiment for a single Yb^+ ion by measuring the effect of cooling pulses for different laser detunings and EMM amplitudes on the ion temperature.

One series of measurements records ion temperature versus EMM amplitude for three different constant laser detunings and shows that the temperature increases with the EMM amplitude before the ion's motional distribution becomes non-thermal and the measurement technique fails. Higher laser detunings achieve a given temperature at higher EMM amplitudes (see subsection 6.4.1) at the expense of cooling of the ion at $E_{\mathrm{rf}} = 0$. Another series of measurements records ion temperature versus laser detuning for three different constant EMM amplitudes. Measurements at an EMM amplitude of $E_{\mathrm{rf}} = 1276\,\mathrm{V/m}$ show that a detuning on the red side of the first micromotion sideband is sufficient to achieve thermal distributions close to the Doppler limit. At $E_{\mathrm{rf}} = 2812\,\mathrm{V/m}$, it is observed that a detuning on the red side of the second micromotion sideband reaches thermal distributions with a mean motional state number of $\bar{n} \approx 40$. However, this considerably exceeds the Doppler limit of $\bar{n} \approx 17$.

The experimental results are compared to theoretical predictions [9]. Both data agree qualitatively, but the experimentally measured scaling of temperature with EMM amplitude differs from the theory. Further tests are required to identify the source of this discrepancy.

Regardless of these discrepancies, this experiment shows that cooling of higher dimensional crystals which feature EMM exposed ions could be applicable. Together with the theoretical findings of chapter 4, that cooling of 2D or 3D crystals might be more efficient, this could lead to the development of new cooling strategies for operating multi-ion clocks.

8 Appendix

8.1 Cooling times of the $(n_{\mathbf{Yb}^+}, n_{\mathbf{In}^+}) = (5, 5)$ composition

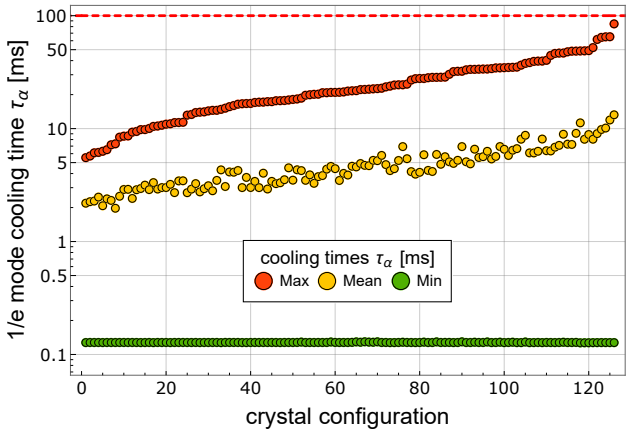

Figure 8.1: Sorted maximal, mean and minimal **radial** mode cooling times τ_α for $\omega_{\text{rad}} = 2\pi\,1000\,\text{kHz}$, $\omega_{\text{ax}} = 2\pi\,189\,\text{kHz}$ ($\alpha \approx 5.3$) for all 126 unique possible configurations with 5 Yb^+ an 5 In^+ ions. A horizontal line at $\tau_\alpha = 100\,\text{ms}$ is shown for orientation. The cooling time axis is scaled logarithmically.

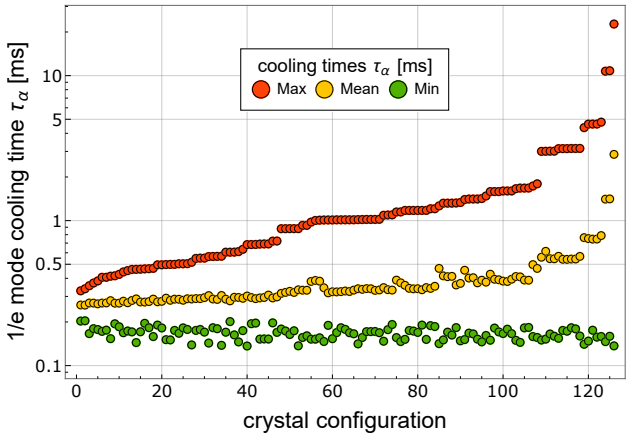

Figure 8.2: Sorted maximal, mean and minimal **axial** mode cooling times τ_α for $\omega_{\text{rad}} = 2\pi\,1000\,\text{kHz}$, $\omega_{\text{ax}} = 2\pi\,189\,\text{kHz}$ ($\alpha \approx 5.3$) for all 126 unique possible configurations with 5 Yb^+ an 5 In^+ ions. The cooling time axis is scaled logarithmically.

8.2 Mean cooling times for five indium ions and different numbers of ytterbium ions

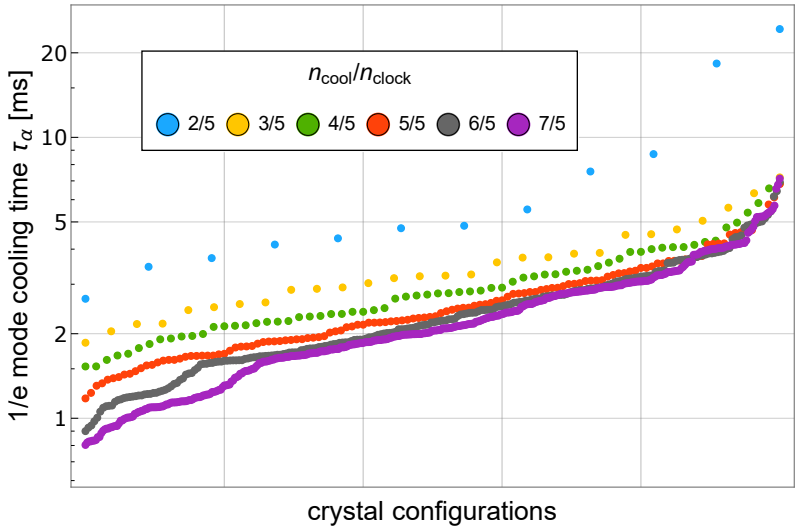

Figure 8.3: Mean 1/e cooling times of radial and axial modes of all configurations of composition with a constant number of 5 clock ions ($n_{clock} = const.$) and different numbers of cooling ions. The cooling time axis is scaled logarithmically.

8.3 Three dimensional cooling times for equal radial and axial confinement

Section 4.4 presents data on 1/e motional mode cooling time of multi-species Coulomb crystals for an example composition with 3 Yb^+ and 10 In^+ ions. The ratio between both radial secular frequencies and the axial secular frequencies $\alpha = \omega_{rad}/\omega_{ax}$ is consecutively decreased from 6 to 1 to investigate, how cooling times behave in two dimensions ($\alpha = 5, 4$) and three dimensions ($\alpha = 3, 2, 1$). The mean and maximal cooling times for $\alpha = 1$ non intuitively plateau on a single value for almost all configurations (as highlighted in figure 8.4). This is briefly discussed in the following.
The answer to the question, where these plateaus come from, is most likely in the equilibrium positions of the respective configurations. These are plotted in figure 8.5. With some deviations the positions form a few distinct circles. Combined with the radial symmetry this hints for lots of similar configurations. Figure 8.6 presents three different configurations in the radial plane with the amplitudes of their worst cooled mode. The configurations seem to be identical or at least similar to each other under rotation and mirroring and therefore feature similar worst mode cooling times. Further analyses could rule out some of the following explanations: The algorithm, that minimizes the potential energy of the crystal to calculate the equilibrium positions in Matlab, could fail for these conditions. The algorithm could also stop in an existing local minimum of the potential energy, meaning that other stable positions for this conditions exist but the algorithm does not reach them. Another explanation could be that only a few unique stable positions for the applied confinement exist. Regardless of the correct answer, it makes sense to come

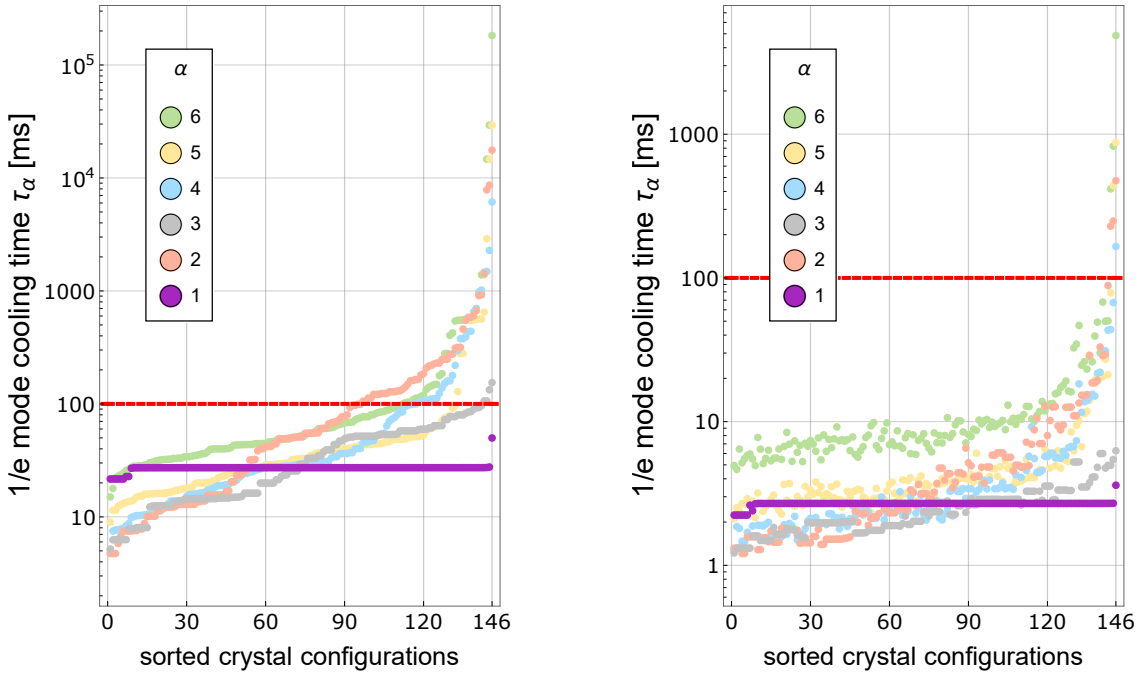

(*a*) maximal cooling times (*b*) mean cooling times

Figure 8.4: Sorted maximal (a) and mean (b) 1/e cooling times of motional modes for all configurations with 3 Yb^+ and 10 In^+ ions for different radial secular frequencies ratios $\alpha = 6, 5, ..., 1$. The data points for $\alpha = 1$ are highlighted. A horizontal line at $\tau_\alpha = 100\,\text{ms}$ is shown for orientation. The cooling time axis is scaled logarithmically.

up with a new method to count and describe the two and three dimensional multi-species Coulomb crystals. It is not useful to address different configurations with respect to the order of ions in the linear chain starting conditions, if these starting conditions do not influence the final configuration.

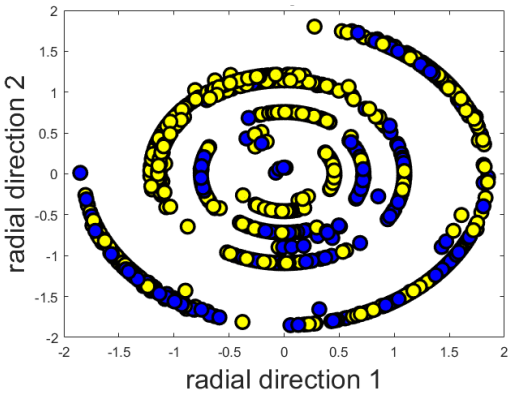

Figure 8.5: Equilibrium positions in the radial plane of all configurations in the $(n_{Yb^+}, n_{In^+}) = (3, 10)$-composition for $\alpha = 1$ calculated by *Matlab*. Yb^+ is presented in blue and In^+ in yellow.

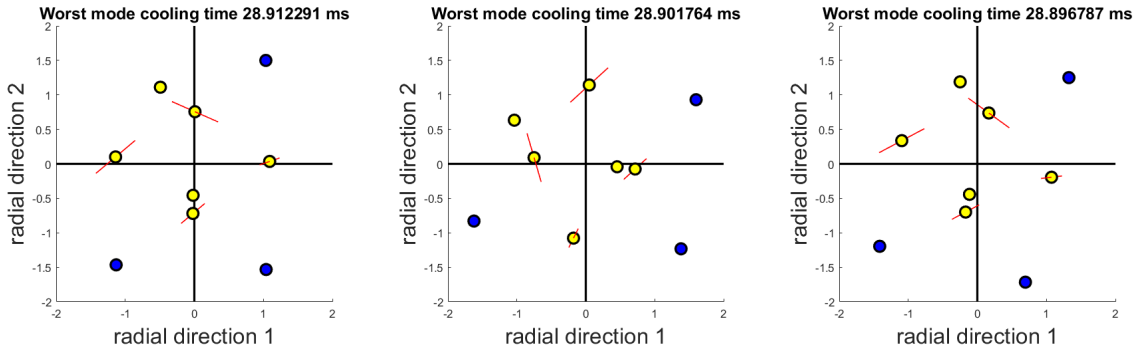

Figure 8.6: Worst cooled modes of three different configurations of the $(n_{\mathrm{Yb}^+}, n_{\mathrm{In}^+}) = (3, 10)$-composition in the radial plane for $\alpha = 1$ calculated by *Matlab*. Yb^+ is presented in blue and In^+ in yellow. The red lines represent the ions' amplitudes in the respective mode. Four of the indium ions align in the axial direction and are therefore drawn on top of each other in the schemes.

References

[1] S. M. Brewer et al. "$^{27}Al^{+}$ Quantum-Logic Clock with a Systematic Uncertainty below 10^{-18}". In: *Phys. Rev. Lett.* 123 (3 July 2019), p. 033201. DOI: 10.1103/PhysRevLett.123.033201. URL: https://link.aps.org/doi/10.1103/PhysRevLett.123.033201.

[2] T. E. Mehlstäubler et al. "Atomic clocks for geodesy". In: *Reports on Progress in Physics* 81.6 (Apr. 2018), p. 064401. DOI: 10.1088/1361-6633/aab409. URL: https://doi.org/10.1088/1361-6633/aab409.

[3] M. S. Safronova et al. "Search for new physics with atoms and molecules". In: *Rev. Mod. Phys.* 90 (2 June 2018), p. 025008. DOI: 10.1103/RevModPhys.90.025008. URL: https://link.aps.org/doi/10.1103/RevModPhys.90.025008.

[4] J. Keller et al. "Controlling systematic frequency uncertainties at the 10^{-19} level in linear Coulomb crystals". In: *Phys. Rev. A* 99 (1 Jan. 2019), p. 013405. DOI: 10.1103/PhysRevA.99.013405. URL: https://link.aps.org/doi/10.1103/PhysRevA.99.013405.

[5] D. J. Larson et al. "Sympathetic cooling of trapped ions: A laser-cooled two-species nonneutral ion plasma". In: *Phys. Rev. Lett.* 57 (1 July 1986), pp. 70–73. DOI: 10.1103/PhysRevLett.57.70. URL: https://link.aps.org/doi/10.1103/PhysRevLett.57.70.

[6] W. Paul. "Electromagnetic traps for charged and neutral particles". In: *Rev. Mod. Phys.* 62 (3 July 1990), pp. 531–540. DOI: 10.1103/RevModPhys.62.531. URL: https://link.aps.org/doi/10.1103/RevModPhys.62.531.

[7] K. Arnold et al. "Prospects for atomic clocks based on large ion crystals". In: *Phys. Rev. A* 92 (3 Sept. 2015), p. 032108. DOI: 10.1103/PhysRevA.92.032108. URL: https://link.aps.org/doi/10.1103/PhysRevA.92.032108.

[8] N. Aharon et al. "Robust optical clock transitions in trapped ions using dynamical decoupling". In: *New Journal of Physics* 21.8 (Aug. 2019), p. 083040. DOI: 10.1088/1367-2630/ab3871. URL: https://doi.org/10.1088/1367-2630/ab3871.

[9] H. Landa. "Tuning nonthermal distributions to thermal ones in time-dependent Paul traps". In: *Phys. Rev. A* 100 (1 July 2019), p. 013413. DOI: 10.1103/PhysRevA.100.013413. URL: https://link.aps.org/doi/10.1103/PhysRevA.100.013413.

[10] F. G. Major, V. N. Gheorghe, and G. Werth. *Charged Particle Traps*. Springer Berlin Heidelberg, 2005. DOI: 10.1007/b137836. URL: https://doi.org/10.1007/b137836.

[11] D. J. Berkeland et al. "Minimization of ion micromotion in a Paul trap". In: *Journal of Applied Physics* 83.10 (1998), pp. 5025–5033. DOI: 10.1063/1.367318. eprint: https://doi.org/10.1063/1.367318. URL: https://doi.org/10.1063/1.367318.

[12] G. Morigi and H. Walther. “Two-species Coulomb chains for quantum information”. In: *The European Physical Journal D* 13 (Jan. 2001), pp. 261–269. DOI: 10.1007/s100530170275.

[13] A. Steane. “The ion trap quantum information processor”. In: *Applied Physics B* 64.6 (June 1997), pp. 623–643. ISSN: 1432-0649. DOI: 10.1007/s003400050225. URL: https://doi.org/10.1007/s003400050225.

[14] Peter Horak, Aurélien Dantan, and Michael Drewsen. “Optically induced structural phase transitions in ion Coulomb crystals”. In: *Phys. Rev. A* 86 (4 Oct. 2012), p. 043435. DOI: 10.1103/PhysRevA.86.043435. URL: https://link.aps.org/doi/10.1103/PhysRevA.86.043435.

[15] W. Demtröder. *Laserspektroskopie*. Springer Berlin Heidelberg, 2011. DOI: 10.1007/978-3-642-21306-9. URL: https://doi.org/10.1007%2F978-3-642-21306-9.

[16] T. W. Hänsch and A. L. Schawlow. “Cooling of gases by laser radiation”. In: *Optics Communications* 13.1 (1975), pp. 68–69. ISSN: 0030-4018. DOI: https://doi.org/10.1016/0030-4018(75)90159-5. URL: http://www.sciencedirect.com/science/article/pii/0030401875901595.

[17] S. Chu et al. “Three-dimensional viscous confinement and cooling of atoms by resonance radiation pressure”. In: *Phys. Rev. Lett.* 55 (1 July 1985), pp. 48–51. DOI: 10.1103/PhysRevLett.55.48. URL: https://link.aps.org/doi/10.1103/PhysRevLett.55.48.

[18] F. Diedrich et al. “Laser Cooling to the Zero-Point Energy of Motion”. In: *Phys. Rev. Lett.* 62 (4 Jan. 1989), pp. 403–406. DOI: 10.1103/PhysRevLett.62.403. URL: https://link.aps.org/doi/10.1103/PhysRevLett.62.403.

[19] C. J. Foot. *Atomic Physics*. Oxford Master Series in Physics. OUP Oxford, 2005. ISBN: 9780198506966. URL: https://books.google.de/books?id=kXYpAQAAMAAJ.

[20] R. H. Dicke. “The Effect of Collisions upon the Doppler Width of Spectral Lines”. In: *Phys. Rev.* 89 (2 Jan. 1953), pp. 472–473. DOI: 10.1103/PhysRev.89.472. URL: https://link.aps.org/doi/10.1103/PhysRev.89.472.

[21] R. Loudon. *The Quantum Theory of Light*. Oxford Science Publications, 2000. ISBN: 9780198501763.

[22] T. Burgermeister. “Development and characterization of a linear ion trap for an improved optical clock performance”. PhD thesis. Leibniz Universität Hannover, 2019.

[23] J. Keller. “Spectroscopic characterization of ion motion for an optical clock based on Coulomb crystals”. PhD thesis. Leibniz Universität Hannover, 2015.

[24] C. Pyka. “High-precision ion trap for spectroscopy of Coulomb crystals”. PhD thesis. Leibniz Universität Hannover, 2013.

[25] S. Bourdeauducq et al. *ARTIQ 1.0*. Version 1.0. May 2016. DOI: 10.5281/zenodo.51303. URL: https://doi.org/10.5281/zenodo.51303.

[26] W. Nagourney, J. Sandberg, and H. Dehmelt. “Shelved optical electron amplifier: Observation of quantum jumps”. In: *Phys. Rev. Lett.* 56 (26 June 1986), pp. 2797–2799. DOI: 10.1103/PhysRevLett.56.2797. URL: https://link.aps.org/doi/10.1103/PhysRevLett.56.2797.

[27] Q. A. Turchette et al. “Heating of trapped ions from the quantum ground state”. In: *Phys. Rev. A* 61 (6 May 2000), p. 063418. DOI: 10.1103/PhysRevA.61.063418. URL: https://link.aps.org/doi/10.1103/PhysRevA.61.063418.

[28] D. Leibfried et al. “Quantum dynamics of single trapped ions”. In: *Rev. Mod. Phys.* 75 (1 Mar. 2003), pp. 281–324. DOI: 10.1103/RevModPhys.75.281. URL: https://link.aps.org/doi/10.1103/RevModPhys.75.281.

[29] R. Loudon. *The quantum theory of light*. Oxford Science Publications, 1973.

[30] H. Landa. Private Communication. 2019.

[31] D. James. “Quantum dynamics of cold trapped ions with application to quantum computation”. In: *Appl Phys B* 66 (1997), pp. 181–190. DOI: 10.1007/s003400050373. URL: https://doi.org/10.1007/s003400050373.

[32] V. Kaushal et al. “Shuttling-based trapped-ion quantum information processing”. In: *AVS Quantum Science* 2.1 (2020), p. 014101. DOI: 10.1116/1.5126186. eprint: https://doi.org/10.1116/1.5126186. URL: https://doi.org/10.1116/1.5126186.

[33] D. Kalincev et al. “Motional heating of spatially extended ion crystals”. In: *Quantum Science and Technology* 6.3 (May 2021), p. 034003. DOI: 10.1088/2058-9565/abee99. URL: https://doi.org/10.1088/2058-9565/abee99.

[34] J. Keller et al. “Precise determination of micromotion for trapped-ion optical clocks”. In: *Journal of Applied Physics* 118.10 (2015), p. 104501. DOI: 10.1063/1.4930037. eprint: https://doi.org/10.1063/1.4930037. URL: https://doi.org/10.1063/1.4930037.

[35] D. J. Wineland et al. “Experimental issues in coherent quantum-state manipulation of trapped atomic ions”. In: *J. Res. Natl. Inst. Stand. Technol* 103 (3 1998), p. 259. DOI: 10.6028/jres.103.019.

Danksagung

Abschließend möchte ich mich noch bei Menschen bedanken, die mich in meiner Zeit an der PTB unterstützt haben.
Zuerst danke ich Prof. Dr. Tanja Mehlstäubler, dass sie mir ermöglicht hat an diesem spannenden Experiment mitzuarbeiten. Auch Prof. Dr. Piet O. Schmidt möchte ich für die Übernahme der Rolle des Zweitprüfers danken.
Vielen Dank an Tabea Nordmann für die tolle Zeit im Labor und für das Korrekturlesen dieser Arbeit. Letzter Dank geht auch an Dr. Jonas Keller und Dr. Nishant Bhatt. Außerdem möchte ich Dr. André Kulosa für die melodischen Autofahrten zwischen Braunschweig und Hannover danken. Vielen Dank auch den Rest der QuaCCS-Gruppe.
Zuletzt möchte ich meiner Studienlerngruppe und meiner Familie danken, ohne deren Unterstützung ich es nicht bis hierhin geschafft hätte.

Erklärung der Selbstständigkeit

Hiermit versichere ich, dass ich die vorliegende Arbeit selbständig verfasst und keine anderen als die angegebenen Quellen und Hilfsmittel verwendet habe. Alle Ausführungen, die sinngemäß oder wörtlich aus anderen Quellen übernommen wurden, sind als solche kenntlich gemacht. Diese Arbeit wurde in gleicher oder ähnlicher Form noch keiner Prüfungsbehörde vorgelegt.

Hannover, den 08. Oktober 2021 Leon Schomburg